



UNIVERSITA' DEGLI STUDI DI PAVIA

DIPARTIMENTO DI CHIMICA

Dottorato di Ricerca in Scienze Chimiche e Farmaceutiche

Direttore: Prof. Antonella Profumo

Chemical Tuning of Hybrid Perovskites for solar-driven clean energy technologies

Relatore:

Prof. Lorenzo Malavasi

Tesi di dottorato di Ricerca

di Ambra Pisanu

TRIENNIO ACCADEMICO 2016-2019 (XXXII CICLO)

Coordinatore: Prof. Mauro Freccero

“[«Che valore hanno per te l'utopia, il sogno?»]

Io penso che un uomo senza utopia, senza sogno, senza ideali, vale a dire senza passioni e senza slanci sarebbe un mostruoso animale fatto semplicemente di istinto e di raziocinio,
una specie di cinghiale laureato in matematica pura.”

(Fabrizio De Andrè)

CONTENTS

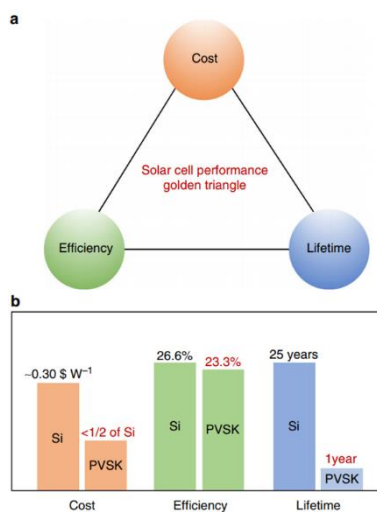
Contents	5
Abstract	8
Riassunto	11
Summary.....	15
Chapter 1. Introduction	18
1.1 Concepts behind solar energy.....	22
1.2 Absorber materials and different types of photovoltaic cells.....	25
1.3 Perovskites.....	29
1.3.1 Crystal structure and tolerance factor	29
1.3.2 Hybrid halide perovskites: history	31
1.3.3 Structure of perovskite solar cells.....	32
1.3.4 Properties of semiconducting perovskites.....	33
1.3.5 Band gap tuning and structural stability control of perovskites.....	37
Chapter 2. A-site Cation Substitution.....	39
2.1 $FA_{(1-x)}MA_xPbI_3$	40
The $FA_{(1-x)}MA_xPbI_3$ System: Correlations among Stoichiometry Control, Crystal Structure, Optical Properties, and Phase Stability	40
Chapter 3. B-site Cation Substitution	54
3.1 $FAPb_{(1-x)}Sn_xBr_3$	56
Exploring the Limits of Three-Dimensional Perovskites: The Case of $FAPb_{1-x}Sn_xBr_3$	56
Chapter 4: Mixed A-Cation Tin-Based Perovskites	69
4.1 $FA_{(1-x)}MA_xSnBr_3$	70
Wide bandgap tuning in Sn-based hybrid perovskites through cation replacement: the $FA_{1-x}MA_xSnBr_3$ mixed system	70
4.2 $MA_{(1-x)}DMA_xSnBr_3$	80

Enhanced air-stability of Sn-based hybrid perovskites induced by dimethylammonium (DMA): synthesis, characterization, aging and hydrogen photogeneration of the MA _{1-x} DMA _x SnBr ₃ system	80
Chapter 5. Anion Substitution in Nanocrystals	94
5.1 Exploitation of lability in post-synthetic reactions.....	97
5.2 FA _{0.8} Cs _{0.2} Pb(Br/X) ₃	98
Facile anion-exchange reaction in mixed-cation lead bromide perovskite nanocrystals	98
Chapter 6. Anion Substitution in 2D Perovskites	110
6.1 Stability issue and advantages of 2D perovskites	110
6.2 BZA ₂ SnX ₄	114
Exploring the Role of Halide Mixing in Lead-Free BZA ₂ SnX ₄ Two-Dimensional Hybrid Perovskites.....	114
Chapter 7. Conclusions and Outlooks.....	135
7.1 Quantitative determination of mixed-ion composition.....	135
7.2 The relevance of electronic dimensionality.....	136
7.3 Simpler conditions of reactions: 3D, 2D and NCs perovskites.....	137
7.4 Outlooks.....	138
7.4.1 Addressing the stability issue.....	138
7.4.2 Reducing the toxicity	139
Publications	143
Reproduced.....	143
Other Publications	144
Ringraziamenti.....	146
Bibliography.....	149

ABSTRACT

In the last years, the massive evolution of modern technologies together with the continuous increase in population, has gradually created an alarming gap between the production and the consumption of energy. The 29th of July 2019 was the Earth overshoot day, day in which we ended the available resources of the year and started consuming more than the planet can produce. From that day on, we are using the resources allocated to future generations. Globally, man is living as if he had 1.75 lands available and Italy is among the less virtuous countries: if everyone followed the Italian lifestyle, we would need 2.72 earths. Italians seem at least aware of this terrible situation, as only 4 out of 10 people believe their life is marked by eco-sustainability. The sense of responsibility seems strong, as does the belief that things can change.

The use of fossil fuels, exercised by man since the First Industrial Revolution, still plays a key role in satisfying the growing energy demand. However, the limited availability of exhaustible primary energy sources and the long-term negative effects on the environment due to the greenhouse effect, make the development of new strategies urgent, so that other primary energy sources can be used effectively: renewable ones. Among all the renewable energy sources available, solar energy is the easiest candidate to provide all the energy required by our growing population.



Golden triangle of solar cells where cost, efficiency and lifetime are considered (102)

Scientific research on this subject has produced very interesting results and hybrid perovskite solar cells are the proof of this. Hybrid perovskites are one of the most promising photovoltaic material: their use in photovoltaic cells increased up to 25% in a decade, making them the fastest growing photovoltaic technology in history.

According to the Golden Triangle rule, in addition to efficiency, stability and cost are the two parameters that must be considered to evaluate the possible commercialization. Efficiency and costs are now competitive with those of traditional silicon cells, the interest has therefore turned to the stability and toxicity of lead. To meet these two major challenges, the best solution is to concentrate research efforts on both the development of new materials and their characterization.

In sight of this, in this thesis the attention focused on the development and characterization of new materials with the main goal of deeply investigate how the perovskites' physical-chemical properties can be modulated by "ad hoc" substitutions in order gain stability. To do this, different materials chemistry strategies have been tackled: substitutions on the organic cation, substitution of the metallic and anionic cation, often faced simultaneously and on perovskites with different dimensionality. The work can ideally be divided into three parts.

The first part of the work deals with a new system in which the most common methyl ammonium (MA) cation has been partially replaced with formamidinium (FA), which leads to more symmetrical perovskites with lower bandgap and better stability. The primary objective was to stabilize the black perovskitic phase of FAPbI_3 by doping it with MA cation. What we obtained is the formation of cubic samples even for very small quantities of MA, without the need for heat treatments. The study of stability over time has led us to demonstrate that, although there is an effective gain in structural stability, time course may lead to phase separation with the formation of the non-perovskitic yellow phase.

Aware of the high toxicity of lead, in the second part of the work, attention has turned to its replacement with less harmful elements. Among these, tin is the one that currently demonstrated the best performances, but it has been scarcely used in the development of new compositions. We first took care of the metallic substitution: the $\text{FAPb}_{1-x}\text{Sn}_x\text{Br}_3$ system showed an unusual evolution of the band gap values, which proved to be the result of a dynamic average of a strongly distorted structure. The end member of the system, FASnBr_3 , solves the problem of structural instability of FAPbI_3 by adopting a highly distorted structure with a fair variance on the length of Sn-Br

distances, that make its structure intermediate between those of 0D and 3D perovskites. The study then continued on two organic cation substitutions in tin-based systems: $\text{FA}_{1-x}\text{MA}_x\text{SnBr}_3$ e $\text{MA}_{1-x}\text{DMA}_x\text{PbBr}_3$. In the first case a remarkable modulation of the band gap has been demonstrated only modifying the ratio of the two amines, which turn out therefore to have a deep impact on the electronic properties. In the other, the presence of the DMA cation led to a very high increase in stability, both in air and in water.

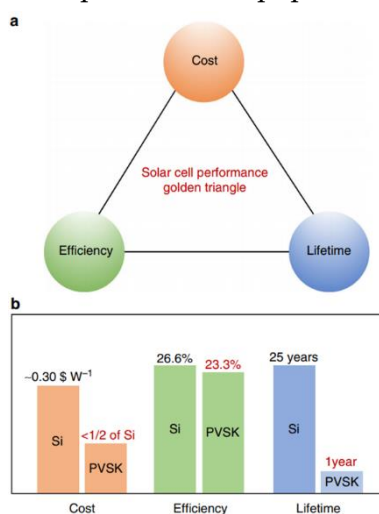
In addition to the research on bulk perovskites, in the third and last part, the study of chemical properties tuning by chemical substitution, in particular anionic substitution, was extended to nano crystalline and two-dimensional perovskites. In both cases, the most evident result is certainly the remarkable modulation of the optical properties: changing the relative quantities of the halide it has been possible to cover almost all the visible spectrum. The synthesis methods used are also noteworthy: in the case of nano-crystals, the anionic-exchange reaction employs a completely new approach, fast and easy, which does not require precursors difficult to synthesize or post-synthetic treatments; some of the 2D samples have been synthesized by mechanochemical synthesis in ballmiller, a sustainable and scalable method that allowed to avoid any contact between air and samples.

The results of this work show that the greater stability of tin-based perovskites, combined with an extremely low toxicity, makes them the most interesting topic for the scientific community to devote the greatest efforts in the near future. The search of new and tuneable phases based on tin, as it has been done for lead, was pioneered for many instances in this work. Alongside, it has already proved urgent to establish standardized parameters for the stability tests of these materials, which will make possible a comparison that is unanimously accepted.

RIASSUNTO

Negli ultimi anni, soprattutto a causa della frenetica evoluzione delle moderne tecnologie e del continuo aumento della popolazione, sta crescendo in modo allarmante la differenza tra produzione e consumo di energia. Il 29 luglio 2019 è stata la giornata del sovrasfruttamento della terra (Earth Overshoot Day), giorno nel quale abbiamo terminato le risorse disponibili dell'intero anno e abbiamo iniziato a consumare più di quanto il pianeta riesca a produrre. Da quel giorno in poi, le risorse che stiamo utilizzando sono quelle destinate alle future generazioni. A livello globale, l'uomo sta vivendo come se avesse 1.75 terre a disposizione e l'Italia risulta fra i paesi meno virtuosi: se il nostro stile di vita fosse seguito da tutti, avremmo bisogno di 2.72 terre. Gli italiani sembrano almeno consapevoli di questa terribile situazione, in quanto solo 4 persone su 10 pensano di condurre una vita ecosostenibile. Il senso di responsabilità sembra forte, così come la convinzione di poter cambiare le cose (fonte: sondaggio YouGov.it).

L'utilizzo dei combustibili fossili, esercitato dall'uomo sin dalla prima rivoluzione industriale, ha tuttora un ruolo chiave nel soddisfare la domanda energetica in costante crescita. Tuttavia, la limitata disponibilità di fonti energetiche primarie esauribili e gli effetti negativi a lungo termine sull'ambiente dovuti all'effetto serra, rendono urgente lo sviluppo di nuove strategie, in modo da utilizzare efficacemente altre fonti di energia primaria: quelle rinnovabili. Tra tutte le fonti di energia rinnovabile disponibili, l'energia solare è il candidato più facilmente praticabile per fornire tutta l'energia richiesta dalla nostra sempre crescente popolazione.



La ricerca scientifica impegnata su questo argomento ha ottenuto risultati molto interessanti e le celle solari a perovskiti ibride ne sono la dimostrazione. Le perovskiti ibride sono uno dei materiali fotovoltaici più promettenti: la loro efficienza è aumentata fino al 24% in un decennio, facendola diventare la tecnologia fotovoltaica in più rapida crescita nella storia.

Secondo la regola del triangolo d'oro, oltre all'efficienza, la stabilità e il costo sono i due parametri che vanno considerati per valutare la possibile commercializzazione. Efficienza e costi sono ormai competitivi con quelli delle celle al silicio tradizionali, l'interesse si è quindi rivolto alla stabilità e alla tossicità del piombo.

Per far fronte a queste due grandi sfide, la soluzione migliore è quella di concentrare gli sforzi della ricerca sia sullo sviluppo di nuovi materiali, sia sulla loro caratterizzazione. In vista di ciò, in questo lavoro di tesi l'attenzione si è concentrata sullo sviluppo e la caratterizzazione di nuovi materiali con l'obiettivo principale di investigare a fondo su come le proprietà fisico-chimiche delle perovskiti possano essere modulate da sostituzioni "ad hoc" al fine di migliorarne la stabilità. Per farlo sono state affrontate diverse strategie: sostituzioni sul catione organico, sostituzione del catione metallico e anioniche, spesso affrontate contemporaneamente e su perovskiti con diversa dimensionalità. Il lavoro può essere idealmente suddiviso in tre parti.

La prima parte del lavoro tratta un nuovo sistema in cui il più comune catione metilammonio è stato parzialmente sostituito con quello formamidinio, il quale porta a perovskiti più simmetriche con band-gap inferiori e una migliore stabilità. L'obiettivo primario era quello di stabilizzare la fase perovskitica nera di FAPbI_3 drogando con il catione MA. Quello che abbiamo ottenuto è la formazione di campioni cubici anche per piccolissime quantità di MA senza il bisogno di trattamenti termici. Lo studio della stabilità nel tempo ci ha portato a dimostrare che, pur essendoci un effettivo guadagno in stabilità strutturale, nel tempo si osserva una separazione di fase che porta alla formazione della fase gialla non perovskitica.

Consapevoli dell'alta tossicità del piombo, nella seconda parte del lavoro l'attenzione si è rivolta alla sua sostituzione con elementi meno nocivi. Tra questi, lo stagno è quello che attualmente ha dimostrato le migliori prestazioni. Ci siamo dapprima occupati della sola sostituzione metallica: il sistema $\text{FAPb}_{1-x}\text{Sn}_x\text{Br}_3$ ha evidenziato un'evoluzione anomala dei valori del band gap, che si è dimostrata essere il risultato di una media dinamica di una struttura fortemente distorta. Il membro finale del sistema, FASnBr_3 , risolve il problema dell'instabilità strutturale di FAPbI_3 adottando

una struttura altamente distorta con una discreta varianza sulla lunghezza dei legami Sn-Br che rendono la sua struttura intermedia fra quelle delle perovskiti 0D e 3D. Lo studio è poi proseguito su due sostituzioni del catione organico in sistemi contenenti solo stagno: $FA_{1-x}MA_xSnBr_3$ e $MA_{1-x}DMA_xPbBr_3$. Nel primo caso si è dimostrata una notevole modulazione del band gap solo modificando il rapporto tra le due ammine, che risultano quindi avere un profondo impatto anche sulle proprietà elettroniche. Nell'altro, la presenza del catione DMA ha portato ad un aumento molto elevato della stabilità, sia all'aria che in acqua.

Accanto alla ricerca sulle perovskiti bulk, nella terza ed ultima parte, lo studio delle sostituzioni, in particolare delle sostituzioni anioniche, è stato esteso a perovskiti nano cristalline e bidimensionali. In entrambi i casi, il risultato più evidente è sicuramente la notevole modulazione delle proprietà ottiche: cambiando le quantità relative dell'alogeno è stato possibile coprire quasi tutto lo spettro visibile. Anche i metodi di sintesi utilizzati sono da evidenziare: nel caso dei nano-cristalli la reazione di scambio anionico utilizza un approccio completamente nuovo, facile e veloce, che non necessita di precursori difficili da sintetizzare o di trattamenti post-sintetici; alcuni dei campioni 2D sono stati sintetizzati tramite sintesi meccanochimica in ballmiller, un metodo sostenibile e scalabile che ha permesso di evitare qualsiasi contatto tra aria e campioni.

I risultati di questo lavoro di tesi evidenziano come la maggiore stabilità delle perovskiti a base di stagno, unita ad una tossicità estremamente ridotta, le renda l'argomento più interessante cui la comunità scientifica dovrà dedicare i maggiori sforzi nel prossimo futuro. Parallelamente, si è già rivelato urgente stabilire dei parametri standardizzati per i tests di stabilità di questi materiali, che rendano possibile un confronto che sia unanimemente accettato.

SUMMARY

This thesis deals with the synthesis and the characterization of new hybrid organic-inorganic perovskites for solar driven clean energy technologies. The interest on hybrid perovskites come from their outstanding qualities: they combine efficiency, scalability, ease of preparation and relatively cost effective and abundant constituent elements, with fascinating unique and tunable physical properties.

Perovskites hold a great promise for the next generation of high performance and low-cost solar cells, but for this technology to be deployed on a large scale, there are some problems which need to be solved. I started working in the field of hybrid perovskite for photovoltaics at the beginning of 2015, when the perovskite fever had just begun, with only a few articles published on this topic, in particular related to the basic materials chemistry issues. The questions and problematics that were raised in 2015 are completely different than the ones of 2019. Over a four years period, thousands of articles were published by over a hundred research groups around the world. The development of perovskite solar cells has focused on two important issues with respect to practical applications: one is photoelectric conversion efficiency (PCE) and the other is stability. (1) The PCEs have been increased to over 25% in just a few years and are now competitive with those of traditional crystalline solar cells, thus general concern has recently turned to the long-term operational stability of perovskite solar cells with exposure to prolonged humidity, heat, light, and oxygen.

In sight of this, the present Ph.D. dissertation has a main goal: to deeply investigate how the physical-chemical properties can be modified by “ad hoc” substitution of the main components in order to gain stability. The perovskite structure naturally lends itself to combinatorial chemistry. One of the key aspects that make perovskites so successful is, in fact, the adaptability of this structure type towards A, B or X site substitution.

This thesis is divided in 7 chapters. After a description of the contextual background provided in the **Chapter 1**, the **Chapter 2** shows the modulation of lead halide perovskites by means of protonated amines, which is a very appealing way of performing such tuning with the aim of extending or changing the absorption edge and improving the material stability. Another investigated substitution route is the Sn for Pb replacement reported in the **Chapter 3**. Sn represent an excellent choice for Pb

replacement despite the problems related to its oxidation. Most of the Sn-based organic-inorganic perovskite investigations focus on the methylammonium cation and iodide anion, *i.e.* the MASnI_3 material. Less extensive investigations are available regarding other protonated amines and/or halogens in Sn-based systems. To start filling this gap, in **Chapter 4** is provided the description of two mixed A-cation Sn-based perovskites. **Chapter 5** and **Chapter 6** face the anion replacement, respectively in colloidal nanocrystalline perovskites and in 2D perovskites. The last chapter summarizes the main findings of the work that is presented herein and provides an overview of some future directions that the field of hybrid perovskites for photovoltaic might take.

CHAPTER 1.

INTRODUCTION

Over the last decade an increasing global concern of climate change has emerged. Polluters and conservationists argue whether increased concentration of CO₂ in the earth's atmospheres, which rose above the scary threshold of 415 ppm in May 2019 (Mauna Loa Observatory), is caused by human emissions or simply a consequence of the earth's eternal temperature cycle. Despite the existence of some few skeptics and evidence deniers, we must recognize that the peaks in CO₂ concentration, as well as the consequent global warming that we are experiencing today, have unquestionably anthropic origins. Because of this, overpopulation is one of the main environmental issue, the main cause of unsustainable depletion of our planet.

The correlation between overpopulation and environmental concerns can be completely understood through the definition by Ehrlich et al. (2)

When is an area overpopulated?... In short, if the long-term carrying capacity of an area is clearly being degraded by its current human occupants, that area is overpopulated.

Recently, many studies confirmed that Human Population Planning alone cannot stop the enormous environmental crisis that we are facing. Indeed, a prompt and effective solution should be found in technology and through the improvement of resources and waste management. The ultimate causes of air pollution are the energy sources that currently drive our transport, electricity generation, industry and food production systems. The connection between the sources of local air pollution and the emissions that drive climate change is very clear. Estimations show that approximately 25% of urban ambient air pollution from fine particulate matter (PM_{2.5}) is contributed by traffic, 15% by industrial activities including electricity generation, 20% by domestic fuel burning, with a remaining 22% from unspecified sources of human origin and 18% from natural sources. (3) The sources of climate change and air pollution are broadly the same: polluting energy systems. For this reason, environmental concerns are strengthening the interest in the alternative energy research field that started already during the 1970s energy crisis. The exploitation of fossil fuels as coal, oil and gas (joint

with the nuclear energy) exercised by man since the first Industrial Revolution, is still playing a lead role to meet the ever-growing energy demand. However, the limited availability of primary exhaustible energy sources and the long-term adverse effects on the environment due to the well-known greenhouse effect, reflects the urgency to develop new strategies (infrastructures, policies, etc.) to effectively utilize other primary energy sources: the renewable ones.

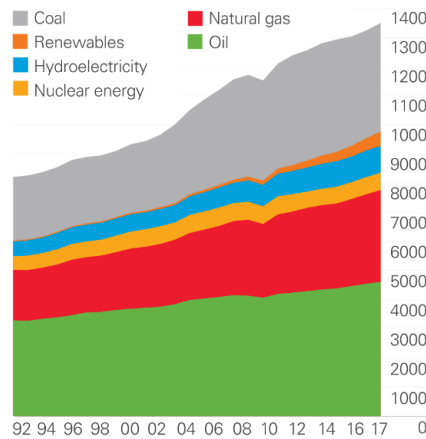


Figure 1.1: World primary energy consumption by fuel type in Mtoe from 1992 to 2017 (4)

Figure 1.1 shows the world primary energy consumption by fuel type in million tons of oil equivalents (Mtoe), from which it is obvious that the energy consumption is continuously increasing and is dominated by the use of fossil fuels. With the uncertainty in the reserves and the concern of its irreparable effect on the climate, the need for renewable energy conversion applications are of primary interest for future global development and sustainability.

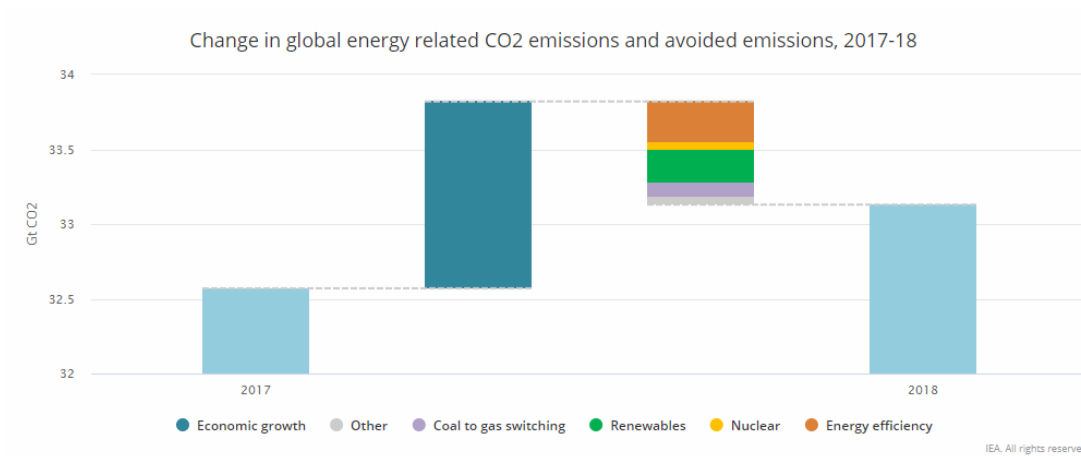


Figure 1.2: Change in global energy related CO₂ emissions and avoided emissions, 2017-18

In the last 20 years a lot of work was done to increase the amount of energy coming from clean sources, not just in terms of research and development, but also in terms of legislation and politics. In Figure 1.2 is reported the change in global energy related to CO₂ emissions and avoided emissions. Increased use of renewables in 2018 had an even greater impact on CO₂ avoided emissions, avoiding 215 Mtoe.

Climate models and strategies that aim at the decarbonization of society often combine the commitments on renewable energies with those on the CO₂ capture; 2018 saw an increase in plans to develop large-scale carbon capture, utilization and storage (CCUS) facilities: the number of projects, operating and under construction, increased a lot. For CCUS to contribute to climate change, the industry would need investment and confidence, but is it really worth spending money on carbon capture? According to MEPs, who have spoken on this issue in their report on the EU 2050 strategy (5), the answer is no, and they are not the only ones to think so. An international research team has for the first time compared the energy performance of investments in renewable energies with those in CCUS technology. In the climate emergency situation in which we find ourselves, the study (6) shows that it is much more affordable and effective to switch to energy production with clean and renewable technologies rather than to reduce emissions from conventional plants. Among all available renewable energy sources (wind, hydropower, geothermal, biomass and solar but excluding nuclear fusion), solar energy is the only viable candidate for supplying all the energy required by our growing population.

I'd put my money on the sun and solar energy. What a source of power! I hope we don't have to wait until oil and coal run out before we tackle that.

This statement sounds contemporary but was pronounced in 1931 by Thomas Edison, the godfather of electricity-intensive living, a green pioneer whose ideas about renewable power still resonate today.

The sun bathes the earth with 92000 TW of electromagnetic radiation, in free form, abundant, non-polluting and, on scale of our times, inexhaustible. Moreover, based on a rough calculation, considering the amount of sunlight that reaches the land area of the Earth, supposing to cover just 2% of the earth surface with solar panels and considering modules with power conversion efficiency of 12%, the power produced would be 67 TW. If it is considered that the global energy demand estimated for 2050 is 30 TW, the amount produced from the Photovoltaic (PV) would be enough to meet the

global demand. Additionally, direct conversion of solar energy into electricity leads to a more efficient energy transportation and storage step. However, the development of PV is still on going and some intrinsic problem has to be overcome before reaching this ambitious target (7).

Currently, almost all photovoltaic panels for commercial use are made of crystalline silicon (c-Si). It is a wafer-based technology, which benefit from high power conversion efficiencies, abundant materials, and proven manufacturability. However, in order to obtain high purity and crystalline materials, the fabrication process is complex and expensive. As a consequence, the production costs increase, and worst, the CO₂ emissions increase, reducing the attraction to this technology. There are other technologies that allow energy production at a lower cost, thin-film semiconductor solar cells and those based on organic, inorganic or hybrid semiconductor solutions are great examples of them. These technologies are often defined, respectively, as second and third generation photovoltaics. Over the last 10 years, the increased research in the third generation has led to huge advances in efficiency, reproducibility and stability. Among the most interesting materials for the development of photovoltaic cells of third generation emerge perovskites, as they use economic precursors and the methods of synthesis are many and versatile. At the time of writing, the perovskite power conversion efficiency record, reported by the Japanese photovoltaic company Solar Frontier Kabushiki Kaisha in April 2019 and certified by the National Renewable Energy Laboratory, is 24.2% (8).

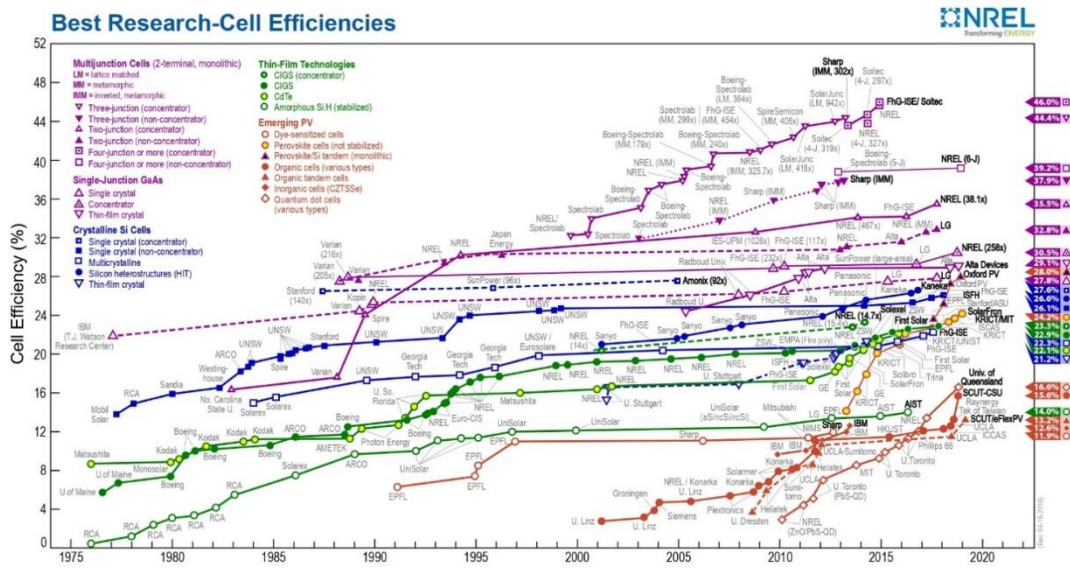


Figure 1.3: Best research-cell efficiency chart plotted from 1976 to the present by NREL (8)

1.1 Concepts behind solar energy

The solar cells convert by photoelectric effect the radiation coming from the sun directly into electricity; solar radiation is not concentrated on a single frequency but is distributed over a spectrum of uneven width: the absorption limit is determined by the spectrum reported below.

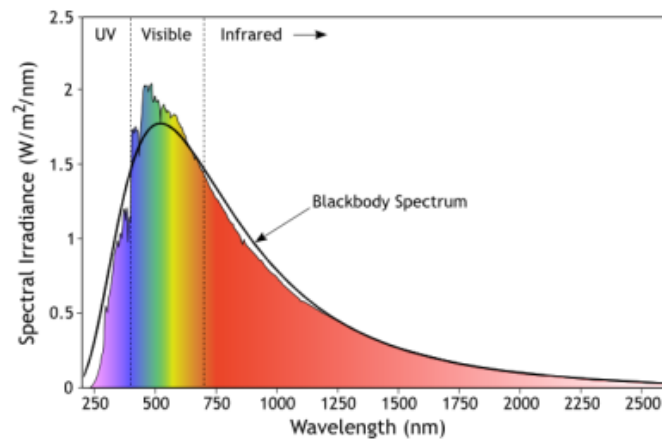


Figure 1.4: Comparison of solar radiation spectrum and black body spectrum at T 5760K

The incident solar radiation on the top of the Earth's atmosphere is described by the solar spectrum AM0, the total incident energy flow is 1353 W/m^2 . However, this radiation is attenuated by the reflection of the radiation in space and by the absorption of gaseous molecules. For this reason, it is preferred to use the direct AM1,5 solar spectrum, whose maximum radiance is 900 W/m^2 and is conventionally normalized to 1000 W/m^2 . It is very important also the angle at which the radiation affects the earth's surface, in fact, the smaller the angle of incidence, the greater will be the thickness of the atmosphere that the radiation must cover and, consequently, the absorption of energy.

The energy of solar radiation is used directly in two ways: for direct conversion to electricity with solar cells and for accumulation of heat by collectors. The first point is described as the conversion of photovoltaic energy, because it is based on the photovoltaic effect (Figure 1.6).

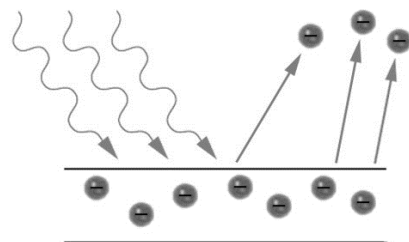


Figure 1.5: Photovoltaic Effect

It is a physical phenomenon that occurs when an electron present in the valence band of a material (usually semiconductor) passes to the conduction one, following the absorption of a sufficiently energetic photon. This effect is closely linked to the photoelectric effect for which a metallic surface emits electrons when struck by an electromagnetic radiation with a given wavelength. The absorption and the emission occur, therefore, by exchange of photons, or light quanta, whose energy is regulated by Planck's law ($E=h\nu$). From the formula it is evident how only photons whose wavelength will be greater than that given by the work function, will be able to produce photoelectrons.

Semiconductors are materials whose properties and electric conductivity lie somewhere between those of a conductor and those of an insulator. Their allowable energy level is interrupted by a little energy gap that divides the valence band from that of conduction. For the electron to be excited the photon must have an energy $h\nu$ at least equal to the E_G ; those with less energy, being unable to be absorbed, will be transmitted or reflected by the semiconductor. When the electron is in the conduction band it starts to lose its energy quickly through phonon generation, once reached the extreme of the band, however, there are no more contiguous electronic states with less energy and to return to the valence band the electron must lose all its excitation energy in one step. The lifetime of the electron within the conduction band is about 10^{-9} seconds, which allows it to convert this energy into electricity. When an electron is promoted to the conduction band, in the valence band remains a hole that can in turn be filled by another electron: the excitation process can then be seen as the generation of an electrically neutral hole-electron pair. To complete the photovoltaic conversion process, the excited electrons must be separated from the holes. The value of the energy gap, the type of semiconductor and the density of the band states are the values to consider in the realization of the photovoltaic cells because they are properties that strongly depend on the absorption coefficient α of the material ($I=I_0 e^{-\alpha x}$).

Absorbing solar radiation is a necessary feature for the operation of a photovoltaic cell, but it is not sufficient; after the absorption of the radiation and the generation of the hole-electron pair, the charges must reach the electrodes. These, however, are subject to recombination phenomena, which depend on three mechanisms: a) band to band recombination, b) trap-assisted recombination and c) Auger recombination

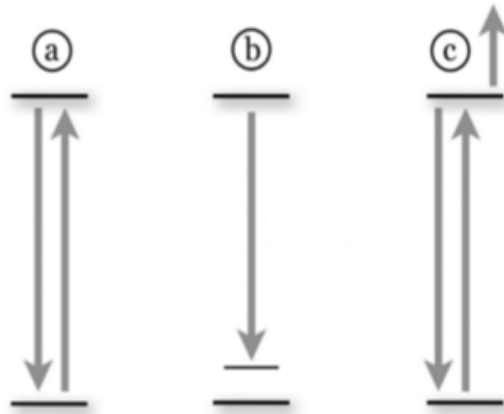


Figure 1.6: Representation of the recombination mechanisms

Band-to-band recombination is a bimolecular process where hole and electron recombine by emitting a photon of energy equal to the material's energy gap. Opposite charges must interact, that's why the process is highly mobility dependent. Trap-assisted recombination exploits a localized energy trap and it is a monomolecular process because it involves one charge at a time. The Auger recombination is instead a trimolecular process, the energy of recombination between hole and electron is transferred to a third particle, hole or electron, which is excited; such a process, to happen, requires a high density of charge, for this reason, when talking about solar cells, is often overlooked. These recombination processes are considered by evaluating two parameters: the lifetime (τ) and the carrier's diffusion length (D). The diffusion length L is the average distance covered by the charge before it gives recombination and is given by

$$L = \sqrt{\tau D}$$

1.2 Absorber materials and different types of photovoltaic cells

The ideal absorber for a photovoltaic cell must combine good optical absorption characteristics with a high charge transport efficiency. In particular it should:

- absorb light in a wide spectral range (approximately 350 nm to 950 nm) and have an energy gap between 1 and 1,5 eV;
- allow the hole-electron pairs to reach the cell electrodes without recombination phenomena;
- have a low cost and abundance in nature;
- be stable and not perishable;
- have a small environmental impact.

As mentioned in the previous sub-chapter, the absorption limit is determined by the solar radiation spectrum (Figure 1.5) and since a material is not able to absorb all the radiation, it is attempted to produce materials that have greater efficiency in proximity of the maximum of this spectrum. The band gap value is limited by this factor, but also by the fact that the cell must optimize the released power. If E_G is small a lot of light will be absorbed, but at the same time, the energy of the charges produced will be small. This means that there is a large current at the head of the cell, but a small voltage and consequently a small output power. If, on the contrary, E_G is high, little light is absorbed, but very energetic charges are produced. In this case the current will be small, but the voltage large and consequently also the power. A compromise must be found between these two extreme cases. It is interesting to see how the efficiency of a photovoltaic cell varies according to the value of the energy gap.

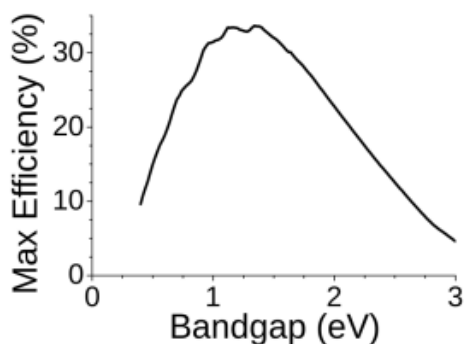


Figure 1.7 Cell efficiency as a function of bandgap

From the Figure 1.7 it can be deduced that the perfect solar absorber can have a maximum theoretical efficiency of approximately 33% when the E_G value is about 1.3/1.4 eV (9). In the realization of photovoltaic cells is also of primary importance the research of low-cost (and therefore easily available) and low environmental impact materials, both in production and disposal.

The history of solar cells can be divided in three parts. (10) The first generation of solar cells is dominated by crystalline silicon wafers (c-Si). The main problem of this technology is the requirement of a large amount of starting material and of a complex and expansive fabrication process. For this reason, a second generation photovoltaic has developed from the early 1980s based on thin-film cells that allow to reduce material usage, manufacturing costs and environmental impact.

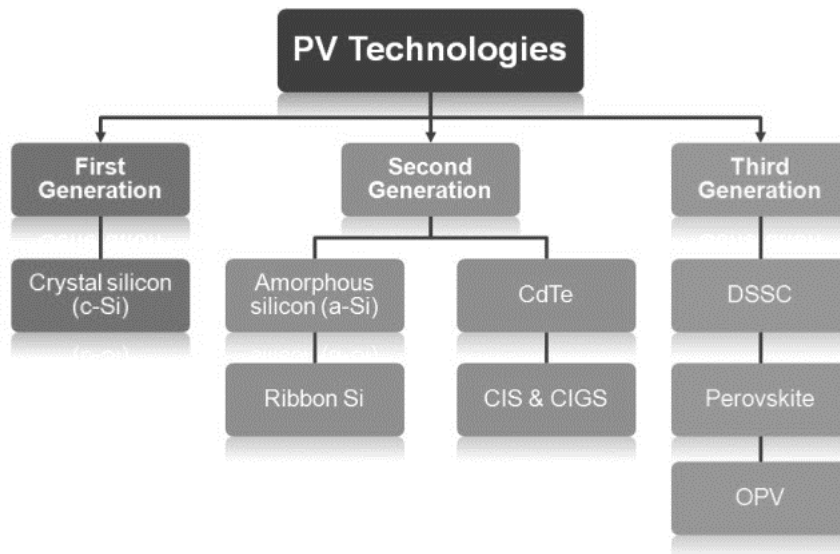


Figure 1.8: Overview of main PV technologies

The second-generation alternatives are:

ribbon-Si, *i.e.* ribbons of polycrystalline silicon, which highly reduce cost for developing PV solar cells. However, due to their high defect density and generally higher impurity concentration, its efficiency is low compared to mono-crystalline cells and other developing materials. (11)

a-Si, namely amorphous silicon technologies, which have a higher bandgap (1.7 eV) than crystalline silicon (1.1 eV) compatible with lightweight and flexible solar cells (12). Those cells are well suited for small-scale and low-power applications, however their susceptibility to light-induced degradation (the Staebler-Wronski effect (13)) and their low efficiency compared to other mature thin-film technologies, limit market adoption.

CdTe, Cadmium telluride technology, that is an attractive thin film technology thanks to the deposition processes that offers low module costs. Good performance was found with sputtered CdTe layers of only 0.5 mm thick, allowing low consumption materials

and reducing the time of processing. (14) However, the main problems of this technology are the toxicity of elemental cadmium and the scarcity of tellurium.

CIGS stand for Copper Indium Gallium diselenide, devices that are based on films which can be deposited by a variety of solution- and vapor-phase techniques on flexible metal or polyimide substrates. They show record efficiencies of 21.7% for cells and 17.5% for modules (15). Despite they seem a good alternative the main disadvantage is the scarcity of indium that could hinder large-scale deployment of these technologies.

Summarizing, the key advantage of the thin-film technologies is the low amount of material used. Furthermore, life cycle analyses suggest that thin films produce lower greenhouse gas emissions during production and use than c-Si (16). However, the use of toxic elements (*e.g.*, Cd) and reliance on rare elements (*e.g.* Te, In) may limit the potential for large-scale deployment along with the high temperature and vacuum processing conditions. In recent years, several new thin-film PV technologies have emerged as a result of intense R&D efforts in materials discovery and device engineering.

Even if the resulting efficiencies are not the same as multijunction or crystalline silicon (for now), the third generation of thin-film PV technologies, which share the goal of low-temperature solution processing, aim to decrease costs to well below the 1\$/W level of second-generation photovoltaics potentially to 0.20 \$/W or better, by significantly increasing efficiencies but maintaining the economic and environmental cost advantages of thin-film deposition techniques. It includes the following:

DSSCs, acronym of Dye-Sensitized Solar Cells, which are photoelectrochemical cells consisting of a transparent inorganic scaffold anode (typically nanoporous TiO₂) sensitized with light-absorbing dye molecules (usually ruthenium complexes). (17) Key challenges involve limited long-term stability under illumination and high temperatures, low absorption in the near-infrared and the presence of rare elements that can limit the use of this technology on large scale production.

OPV stands for Organic PV and it is based on organic small molecules, fullerene derivatives or polymers. These materials consist mostly of Earth-abundant elements, that can be processed by solution, reducing the fabrications costs. They are compatible with roll to roll fabrication that allow to implement the large-scale production. (18) They are compatible with light weight, transparent, plastic substrates. They show the smallest ecological footprint and the shortest energy payback time possible (7). Key challenges are to get high efficiency at the modules scale and to increase the lifetime.

Perovskite cells evolved from DSSCs. The origin of the surprisingly high efficiencies exhibited by solar cells fabricated with perovskites remains a subject of widespread interest. To understand the origin of their outstanding performance, it is essential to first understand their crystal structures, characterized by structural phase transitions, considerable static or dynamic disorder and unknown concentrations of various defects such as halide anion or organic cation vacancies. The hybrid perovskites are far more complicated than conventional photovoltaic materials and the perovskite structure is the basic framework adopted by a wide variety of functional materials such as ionic conductors, ferroelectrics and superconductors. They will be widely treated in the next paragraph.

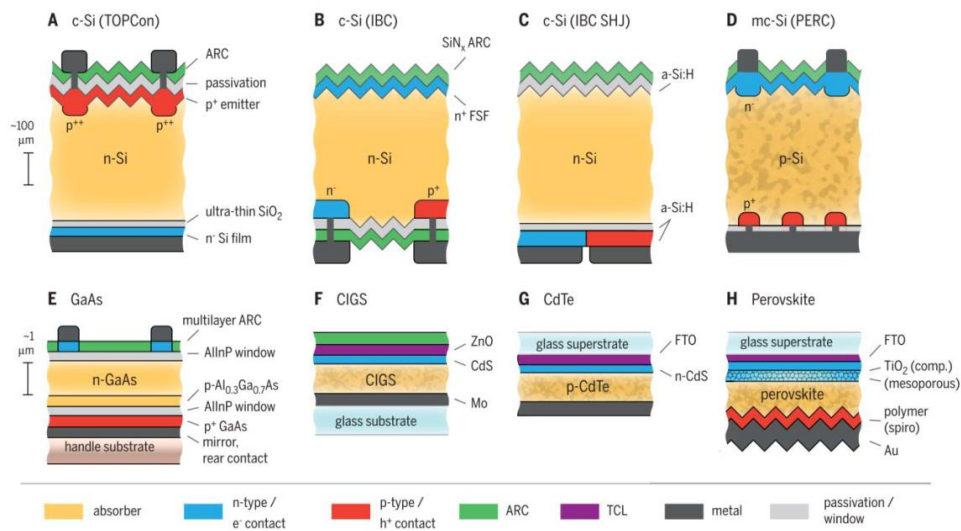


Figure 1.9: Solar cells with record efficiencies above 20% (19)

1.3 Perovskites

The perovskite is a particular type of mineral with cubic crystals composed of calcium titanite (CaTiO_3), discovered in 1893 by Gustav Rose and named after Lev Perovskiy. Over time this nomenclature has been adopted to indicate the whole class of compounds having a structure similar to that of the natural oxide, that is ABX_3 . There are hundreds of compounds belonging to the perovskite family, natural and synthetic, which have the most varied physical properties: antiferromagnetic, ferroelectric, piezoelectric, optoelectronic, insulating, semiconductor or conductor and super conduction.

1.3.1 Crystal structure and tolerance factor

The ideal perovskite cubic structure is described by the generalized formula ABX_3 , where B is the metal cation with a small ionic radius, X is the anion, usually oxygen or a halogen and A is always a cation, metallic or not, with a big ionic radius. B and X atoms form octahedrons BX_6 in which B and X are arranged at the corners and at the edges respectively, while A cation is placed among the octahedrons, occupying the 12-fold coordination site formed in the middle of the cube of eight such octahedra, balancing the charge.

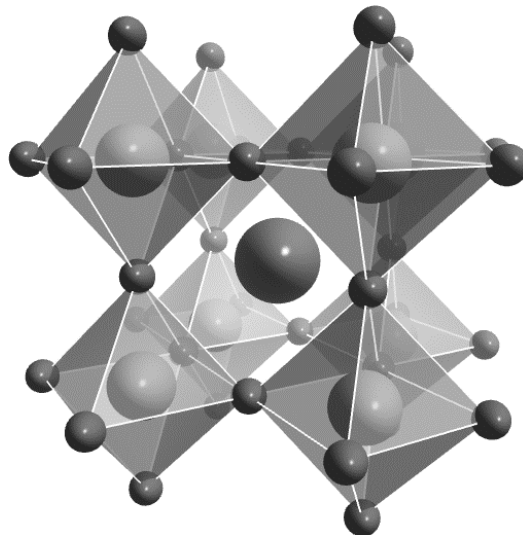


Figure 1.10: Three-dimensional representation of the perovskite structure

Despite the simplicity of the original perovskite crystal structure, this family of compounds shows an enormous variety of structural modifications and variants. Owing to steric constraints, caused by different combinations of ionic radii, the unit cell of most perovskites is slightly distorted. The ideal cubic perovskite structure is not very common (also the mineral perovskite itself is slightly distorted) and it is only present within SrTiO₃. There are 5 different mechanisms that cause these changes: distortion of the octahedral structure BX₆ due to the Jahn-Teller effect; displacement of B from the central position of the octahedral structure; the overturning of the octahedral structure that occurs when B is too small; ordering of one or both cations; ordering of the anion.

Such distortions are fundamental because the interest in compounds belonging to this family of crystal structures arise in the large and ever surprising variety of properties exhibited and the flexibility to accommodate almost all of the elements in the periodic system. Pioneering structural work on perovskites were conducted by Goldschmidt in the 1920s (20) in which he introduced an experimental factor used to quantify the magnitude of distortions and to predict the stability of the perovskite structure based only on the chemical formula, ABX₃, and the ionic radii (r_i). This factor is called Goldschmidt tolerance factor and is described by the following equation:

$$t = \frac{r_A + r_X}{\sqrt{2}(r_B + r_X)}$$

where r_A , r_B and r_X are the radii of the different ions. The value of t varies between 0.7 and 1.1. For $t = 1$ it's found the perfect perovskite cubic structure. The further t moves away from this value, the more the structure deforms. In general, materials with a tolerance factor of 0.9–1.0 have an ideal cubic structure. A tolerance factor of 0.71–0.9 results in a distorted perovskite structure with tilted octahedra (orthorhombic and rhombohedral variants). Non-perovskite structures are formed when the tolerance factor is higher (hexagonal structures) or lower (corundum or ilmenite).

1.3.2 Hybrid halide perovskites: history

The first report of lead-based halide perovskite structures dates back from 1893 with the syntheses of CsPbBr_3 and CsPbI_3 (21). However, it is only in 1958 that their structures were identified as perovskites by Møller (22), who also identified the photoconductive nature of their single crystalline forms, suggesting semiconducting behavior. The first report of an organic-inorganic lead halide perovskite structure dates from Weber, who was the first to introduce the methylammonium cation (CH_3NH_3^+) as an alternative for Cs^+ . Methylammonium lead iodide ($\text{CH}_3\text{NH}_3\text{PbI}_3$), in particular, is exhibiting fascinating optoelectronic properties, among which its narrow band gap (1.55 eV, onset at 800 nm (23)) and high charge diffusion length (100 nm to 1 μm (24) (25)) makes it an ideal candidate as a photo-active layer in solar cells. Such appealing properties are the result of low exciton binding energies (30 meV) (26) and high mobilities (27). This intriguing material was further incorporated into field-effect transistors (FETs) by Mitzi in the middle of 1990s demonstrating the promising property of perovskites in electronic devices.

The potential of $\text{CH}_3\text{NH}_3\text{PbI}_3$ as a photoactive material was first recognized by Kojima (28) in 2009, however, as the device delivered just 3.8% power conversion efficiency, had an active area of 0.24 cm^2 and was stable for only a few minutes as a result of the hydrolysis and partial dissolution in the electrolyte, these initial results presented uncertainties about the likely deployment of these materials in photovoltaics and were largely overlooked by the community until 2012, where the first solid-state perovskite solar cells appeared (29). In 2012, the group of Michael Grätzel in Switzerland and Nam-Gyu Park in South Korea (30), demonstrated solid-state perovskite photovoltaic devices that overcame the poor stability of the material in liquid-based dye-sensitized solar cells. Later in the same year, Henry Snaith and colleagues (31) in the United Kingdom demonstrated that these materials are not only able to sensitize a semiconductor, but also, and more interestingly, can themselves transport electronic charges to the solar cell electrodes, enabling higher device efficiencies. Organic-inorganic lead halide perovskites thus became the front runners among emerging photovoltaic materials and the field has advanced dramatically ever since.

1.3.3 Structure of perovskite solar cells

Almost all perovskite solar cells are constructed using bottom-up processes on transparent conductive oxide coated glass. However, there are structural differences that allow to classify them into three different categories: mesoscopic, flat and fully mesoporous hole transporter free solar cells.

Mesoscopic hybrid perovskite solar cells

The leading class of hybrid perovskite solar cells in terms of power conversion efficiency and stability. They are based on a mesoscopic n-type TiO_2 film deposited on the conductive glass coating with a thin, compact TiO_2 layer. The titanium dioxide acts as an electron transport layer and selectively blocks the holes. The mesoporous film generally consists of anatase nanoparticles (18-30 nm) forming a porous 100-200 nm thick film. The TiO_2 film is infiltrated by $\text{CH}_3\text{NH}_3\text{PbI}_3$ (or a related hybrid perovskite) deposited from solution. In most cases, a thick and compact 200-250 nm layer of $\text{CH}_3\text{NH}_3\text{PbI}_3$ caps the electron transporting layer. A thin hole transport layer is then deposited on top of the perovskite layer to provide selectivity for the holes and block the electrons. Most hole transport materials consist of doped Spiro-MeOTAD with additives (LiTFSI and 4-tertbutylpyridine) (32), but variations have been reported, notably copper thiocyanate (CuSCN) (33) (34) or poly-triarylamine derivatives (PTAA) (35) (36). The device assembly is terminated by thermally evaporating a 40-200 nm top layer of gold or silver. Research is greatly active towards the optimization of each layer, such that certified power conversion efficiencies have quickly raised from 14.1% to 24.2% in less than five years (8).

Flat hybrid perovskite solar cells

In the fabrication of flat hybrid-perovskite heterojunction solar cells reported (37) (38) (39), various electron transporting layers can be used, such as the traditional TiO_2 blocking layer, zinc oxide or PCBM, in which case the perovskite must be deposited by thermal evaporation. In particular, the use of SnO_2 as the ETL has attracted significant attention in view of their increased stability and efficiency (40). The rest of the device remains the same as in mesoscopic solar cells.

Fully mesoporous hole transporter free solar cells

At the opposite of flat hybrid perovskite solar cells are fully mesoporous solar cells. They are fabricated through the sequential printing of a TiO₂ mesoporous layer, a mesoporous inorganic spacer (ZrO₂ or Al₂O₃) and a mesoporous back-contact (usually graphite-based). The three layers are sintered together and infiltrated by the hybrid perovskite material from solution, which fills the pores of all three layers. There is no selectivity for the hole extraction, which must be transported through the perovskite layer towards the carbon back-contact. Therefore, the functioning of the device relies on the quick charge transfer of the electrons into the titanium dioxide. Failure to transfer the electrons is synonym of electron-hole annihilation and is to be avoided.

1.3.4 Properties of semiconducting perovskites

In this paragraph are reported the advances in understanding the fundamental properties of hybrid halide perovskites that explain why they work so well for solar cells.

Light absorption and charge generation

As said in the paragraph about absorber, a good photovoltaic material should have a large absorption coefficient. Besides efficient light harvesting, it also contributes to a large open-circuit voltage because the material would require only a thin active layer which can reduce the charge recombination. Hybrid perovskites are among the most efficient photovoltaic absorbers; for example, the absorption coefficient of methylammonium lead iodide (MAPbI₃) ($>3.0 \cdot 10^4 \text{ cm}^{-1}$ in the visible light region) is more than one order of magnitude larger than that of silicon. As a result, the thickness of most reported high-efficiency OIHP solar cells is in the range of 0.3–0.6 μm (31) (41), whereas crystalline silicon solar cells are about 300 μm thick. A thin photoactive layer also requires less material and is thus lower in cost. This strong absorption of MAPbI₃ has been attributed to its direct band gap and Pb 6p – I 5p transitions (42). A major form of V_{oc} loss is the loss of energy to separate light generated Frenkel excitons, which have large binding energies. As a consequence, a donor/acceptor heterojunction interface with a large energy offset is necessary to provide the driving force for the dissociation. For photovoltaic applications, a small E_B , like the one of inorganic semiconductors, is favorable to minimize the energy loss. The hybrid nature of these perovskites makes one wonder whether its behavior, with respect to free charge generation, is similar to that of

inorganic or organics materials. To answer this question, the E_B in MAPbI₃ has been intensely studied with reported values varying from 2 to 75 meV. Nevertheless, according to numerical simulations, the free charge dominates the photogenerated species under solar cell operating conditions, even with high E_B . These results suggest that MAPbI₃ can be classified as a non-excitonic material in photovoltaic applications: the direct generation of free charges dominates the conversion process. The E_B in perovskites is also found to be sensitive to their microstructure (43): in perovskite thin films with small grains, disorders and variations of electrostatic potential decrease the E_B and suppress exciton formation, thus, tuning the crystal size can narrow down the effective bandgap without changing the composition of the perovskite. In addition to composition and microstructure, the dimensionality of the crystal structure also influences exciton binding energies. Recently, 2D hybrid perovskites, consisting of lead iodide octahedral layers intercalated with large organic cations as spacers, have gained considerable research interest because of the prospect of enhancing moisture and light stability (44) (45). Two-dimensional perovskites are essentially quantum wells: the charge carriers are mainly confined in the lead iodide octahedral planes because the organic layers have a larger bandgap and smaller dielectric constant. However, 2D perovskites suffer from having much larger exciton binding energies (270-380 meV) owing to spatial quantum confinement (46).

Charge recombination rate

A longer carrier recombination lifetime is needed for larger V_{oc} because it enables a higher carrier concentration for solar cells under illumination. The Auger charge recombination is generally weak compared with other recombination channels. Different techniques have been used to determine the mono and bimolecular rate constants. The very weak bimolecular charge recombination makes monomolecular (10^{-6} - 10^{-7} s⁻¹) charge recombination the dominant process (47). Most of the polycrystalline films in solar cells with efficiencies >20% still have a film photoluminescence lifetime much shorter than 10 μ s. This indicates that the efficiency or V_{oc} of these state-of-the-art solar cells is still limited by the trap-related charge recombination in the perovskite films, in addition to the charge recombination at the perovskite/electrode interfaces.

Defect tolerance

Conventional wisdom, developed over decades of research on Si, CdTe and GaAs, holds that PV-grade electronic quality requires ultralow concentrations of impurities and crystalline defects, typically at ppb-levels, because all act as dopants or electronic traps. There are different types of defects in crystalline semiconductors which can be present in the form of point defects and higher dimensional defects producing recombination or emission centers that are at the heart of the optoelectronic properties. Due to these defects, semiconductors create unintentional n- or p-type doping, leading to the formation of p-n junctions. In his work about defect tolerance in new compounds, professor Aron Walsh (48) explains that halide perovskites are different from the majority of materials: HP PV devices contain an ultra-high density of defects but the presence of these defects does not destroy the performance of solar cells. In optoelectronic devices, it is essential to avoid non-radiative processes that convert electronic to thermal energy via defects. These events lower efficiency and can trigger device breakdown. It turns out that many of the low energy point defects in halide perovskite are “inert”, which is one of the reasons for these materials’ success. There are other properties that are in relation with the presence of defects. The mobile ions issue is said to be due to the defect properties within perovskite structures. The presence of halogen interstitial or vacancy within the structure plays a major role: it has been observed that under light exposure, iodide and bromide species migrate along the cell, creating iodide- and bromide-rich domains, that act as recombination centers.

Doping in perovskite semiconductors

In typical crystalline semiconductors, defects are very important for the reason they allow the doping of the structure. Low and moderate doping is important for many electronic properties of semiconductors, such as conductivity and mobility. In solar cells, doping can directly change the charge carrier recombination rate, diffusion length and contact resistance, as well as the V_{oc} . However, intentional extrinsic doping of hybrid perovskite materials is difficult to achieve because of the defect-tolerant nature and low activation energy for ion migration. The self-doping properties can be explained by the similar formation energies of the dominant donor and dominant acceptor (49). Apparently, the self-doping level in perovskite materials is sensitive to the precursor composition and fabrication process parameters.

Photon recycling

The photon recycling effect was proposed to contribute to the high V_{oc} in GaAs solar cells and thus be responsible for increasing the PCE from 25 to 29%. The perovskite community is now asking the question of whether the photon recycling effect also contributes to the large V_{oc} in perovskite solar cells. In fact, there are many similarities between perovskites and GaAs. For example, both exhibit high absorption coefficients near the band edge ($\sim 10^3 \text{ cm}^{-1}$), which gives rise to high self-absorption ratios. Recently, the first experimental evidence for the photon recycling effect in MAPbI₃ polycrystalline thin films was reported, showing that charge generation was observed more than 50 μm from the light-absorbing region (50). In these systems, the efficiencies of photon recycling were less than 0.5%, showing negligible photon recycling effects under the solar cell working conditions. The low photon recycling efficiency may be attributed to the low internal photoluminescence quantum yield (PLQY) of the perovskite thin films and single crystals.

High electronic dimensionality

The concept of electronic dimensionality was introduced to partially explain why MAPbI₃ exhibits excellent photovoltaic properties whereas other metal halide perovskite absorbers do not (51). The electronic dimensionality is defined by the connectivity of the electronic orbitals that comprise the lower conduction band and the upper valence band. It is better than the conventional structural dimensionality for explaining photovoltaic properties because although some perovskites are both structurally and electronically 3D, some are structurally 3D but exhibit lower-dimensional electronic structures. Low electronic dimensionality implies that, at a minimum, the absorber films must be grown with special crystallographic orientation to facilitate effective carrier transport.

Ion migration

Ion migration is a unique property of hybrid perovskites and is not present in other photovoltaic materials. Although ion migration has been reported to affect device operation and stability in various ways, here the focus will be on the beneficial role on device efficiency. The accumulation of ions under working conditions was shown to actually enhance the device efficiency by providing an additional electric field to facilitate charge extraction. This may contribute to enhanced device efficiency over time. (52) Nevertheless, the ion back-diffusion that occurs when the devices are kept in the dark would negate the light-induced diffusion. There is little doubt that ion migration

can impair the long-term device stability of perovskite solar cells under continuous operation by damaging the perovskite layer or other layers. Nevertheless, some interesting studies have shown that the short-term stability actually benefits from ion migration in the perovskite layer of devices operating under cycled illumination.

1.3.5 Band gap tuning and structural stability control of perovskites

Metal halide perovskites benefit from the combination of wide absorption, high carrier mobility, moderate exciton binding energies and versatility of solution processes. As said before, the development of perovskite solar cells has focused on two important issues with respect to practical applications: one is photoelectric conversion efficiency (PCE) and the other is stability. The PCE has been increased from less than 4% to over 24% in just a few years (8) through device engineering and materials design based on the desired optoelectronic properties and they are now competitive with those of traditional crystalline solar cells.

For this reason, concern has recently turned to the toxicity and long-term operational stability of perovskite solar cells with exposure to prolonged humidity, heat, light, and oxygen which are still the Achille's heel limiting their further practical applications. Perovskite materials most often suffer from a rapid degradation upon exposure to humidity, process which also appears to be accelerated by heat. The possible mechanisms of decomposition in moisture may be as follows (53):

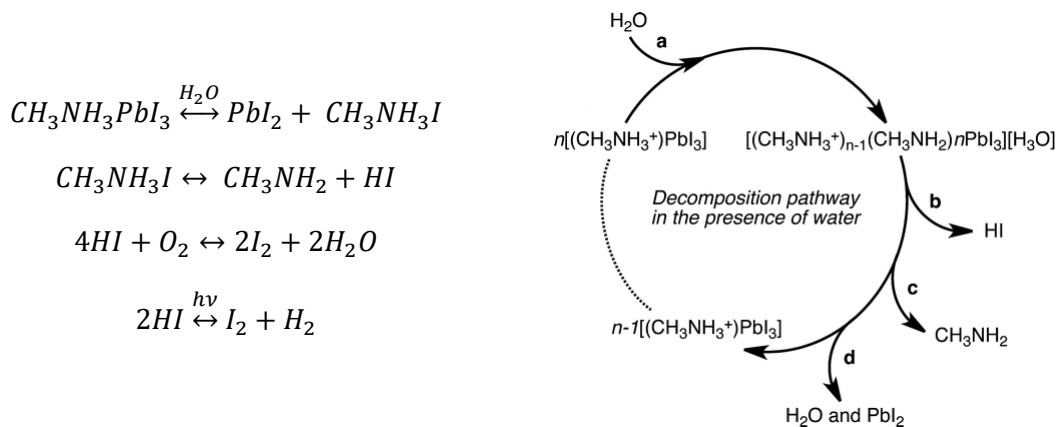


Figure 1.11: Possible reactions and mechanisms of decomposition of hybrid perovskites in moisture (53)

Walsh et al. demonstrated that water react as a Lewis base, the proton of the amine coordinates with H_2O to the intermediate $[(CH_3NH_3^+)_{n-1}(CH_3NH_2)_n][H_3O]$

which continue to decompose. It is clear that moisture is a critical cause of instability and that led to make top charge-transporting layer of the device as a first line of defense.

Another big problem is the ion migration. It is an intrinsic factor and cannot be eliminated by encapsulation. So far, various effective methods have been developed such as passivation on trap states (54), introducing supramolecular cation- π interaction (55), doping with larger amine cations (56) and increasing the grain size (57). The ion migration phenomenon is often correlated with light exposure. The ion migration is, in fact, light enhanced: as light increase, it can be observed a significant reduction in the activation energy of the ionic transport. (58)

Fortunately, hybrid lead halide perovskites have a very high tolerance toward changes in physical properties arising from doping or addition of different cations and anions, in many cases showing improved properties. There are a lot of engineering approaches to face this problem, but they require a careful and precise design. Recently a lot of research has focused on the modification of perovskite material since a small lattice expansion or distortion cause a symmetry change that give a different structural stability to the material. Chemical doping of an impurity was reported to be an effective approach to solve these issues, while providing additional tunable properties. As said before, unlike from the dopants in conventional inorganic semiconductors which create deep energy levels and act as electron traps, dopants in metal halide perovskites generally do not give rise to mid-gap trap states, they are inert.

In view of the significant effect of dopants on the physical and chemical performance, in the next chapters will be discussed different kinds of doping behavior: A-site cation, B-site metal and X-site halogen doping with a brief focus on nanocrystalline and 2D perovskites. These contents provide an in-depth insight into the structure-property relationship, which is crucial for further improvements.

CHAPTER 2.

A-SITE CATION SUBSTITUTION

The A cation occupies the center of the 3D perovskite which is a key part of the perovskite that determines its type of structure and dimensionality. It was found to have no direct influence on electronic properties of the perovskite. Nevertheless, it has been revealed via simulations that the size of the A cation can vary the amount of distortion which ultimately affects electronic characteristics of the material (59). Despite a number of experimental reports and intriguing proposals, an in-depth atomistic understanding of these improvements is currently unclear.

Among compositional engineering approaches, the mixing of different sized A-cations has shown promise in producing longer-lived solar cells. In particular, engaging the A site vacancy by a tiny monovalent cation with a radii similar to that of the original cation, like cesium (Cs), rubidium (Rb), methylammonium (MA), formamidinium (FA), results in a three-dimensional symmetrical structure (60). In this case the aim is to obtain a more-stable cubic phase and the appropriate dynamic position of the conduction band. But, when a small cation is replaced by a larger organic primary ammonium cation, the 3D perovskite would move to a 2D layered structure as a result of steric effects.

2.1 FA_(1-x)MA_xPbI₃

The FA_(1-x)MA_xPbI₃ System: Correlations among Stoichiometry Control, Crystal Structure, Optical Properties, and Phase Stability

Purpose and scope

The FA_(1-x)MA_xPbI₃ solid solution has been the first mixed system that I investigated during my master thesis. We were the very first group to use the solid-state ¹H NMR to determine the effective ratio of the mixed-cation composition in this kind of materials. This allowed for a quantitative analysis demonstrating that the actual compositions of the samples were slightly different from the nominal compositions used for the synthesis. I would like to thank Chiara Ferrara for the acquisition of these data and their analysis. The precise control over the real stoichiometries allowed for the determination of a reliable correlation between the amount of protonated amine and the physiochemical properties.

Another important aspect investigated was the deleterious effect of aging on these mixed compositions, observed by X-ray diffraction and optical measurements. While the behaviour of the pure FAPbI₃ as a function of time is well-known, the stability issue of these mixed system has never been studied before. We demonstrated that only for small x values, the perovskite phase is not stable with time, showing a progressive phase separation, which is, anyway, much slower than that of the two end members.

Introduction

Mixed methylammonium/formamidinium (MA/FA) lead halide hybrid perovskites have recently attracted significant interest because of the very high efficiencies of perovskite solar cells (PSCs) employing such semiconductor layers, which exhibit strong band-gap photoabsorption.¹⁻⁴ One of the reasons for using these mixed systems is the need to stabilize the black phase (α) of formamidinium lead iodide (FAPbI₃) at room temperature. In fact, at room temperature, FAPbI₃ crystallizes in a hexagonal yellow phase (δ -phase) in the space group P6₃mc, whereas the perovskite α -phase, with an optimal band gap of about 1.47–1.49 eV, is achieved by crossing the phase transition above 165 °C.⁵ The black α -phase crystallizes in a cubic symmetry with space group Pm $\bar{3}$ m. Interest in the use of FAPbI₃-based perovskites is also related to the facts that (i) the larger FA cation leads to more symmetric perovskites than for the MAPbI₃ (MAPI)

phase (which is tetragonal at room temperature), (ii) the smaller band gap of FAPI allows for near-IR absorption, and (iii) perovskites containing FA cations have improved stability.⁶ Most of the solid solutions investigated so far are based on FAPI systems with partial substitution of Br for the I halogen and mixed MA/ FA lead iodides.¹⁻⁶ The present work focuses on the latter system.

$\text{FA}_{(1-x)}\text{MA}_x\text{PbI}_3$ system has been the subject of a number of studies in the past few years reporting very high efficiencies for PSCs employing such phases.^{2,3,6-8} For example, Pellet et al.² explored several compositions of the $\text{FA}_{(1-x)}\text{MA}_x\text{PbI}_3$ system using samples prepared in the form of films by infiltrating TiO_2 with PbI_2 , dripping these films in mixed FAI and MAI solutions, and then performing a thermal treatment. According to the observed XRD patterns, each of the samples still contained a significant amount of PbI_2 , no lattice parameters were provided, and only relative shifts from the peaks of FAPI were reported. In addition, the starting FAPI sample consisted of a mixture of α and δ phases with a band-gap value, E_g , for pure FAPI reported to be 1.53 eV, which is higher than most of the values reported in the current literature (about 1.48 eV). Moreover, the E_g values reported for phases with very different nominal stoichiometries, such as FAPbI_3 and $\text{FA}_{0.4}\text{MA}_{0.6}\text{PbI}_3$, were the same.² Such anomalous trends might be due to the peculiar growth kinetics of the films prepared by the reported method, leading to a difference between the nominal and real compositions. In the work of Binek et al., XRD investigation on powdered samples revealed the stabilization of the cubic phase of FAPI when the amount of FA was greater than 20%, whereas for lower stoichiometries, the solid solution maintained the tetragonal symmetry of MAPI.⁶ The authors also reported no lattice shrinkage upon the replacement of about 13% of the FA with MA and confirmed the stabilization of the α -phase induced by MA doping already at relatively low amounts. Moreover, in ref 6, for all of the levels of MA doping in α -FAPI (5%, 10%, and 15% MA), the band gap remained the same, at about 1.52 eV.⁶ A very recent work by Jacobsson et al. presented a comprehensive investigation of the $\text{FA}_{(1-x)}\text{MA}_x\text{PbI}_3$ system.³ In that case, the band-gap value of FAPI was reported to be 1.52 eV, the trend of the cell volume as a function of MA content did not follow a linear trend (as predicted by Vegard's law for solid solutions), and no information was provided on the real stoichiometries of the prepared films. It is surprising to see how large the spread is in the reported results for the $\text{FA}_{(1-x)}\text{MA}_x\text{PbI}_3$ system in terms of the crystal structure and optical properties. Some of the discrepancy might arise from the presence of powdered and thin-film samples and, for the latter, from the fact that their preparation by means of different routes can lead to compositions that differ from the nominal ones. Another relevant point might be the actual phase stability of FA-rich phases. Concerning this last

point, the literature does not provide any information about the time stability of the α -phase within the $\text{FA}_{(1-x)}\text{MA}_x\text{PbI}_3$ system. It is well-known that the pseudo-cubic black phase of pure FAPI can be stabilized at room temperature after a thermal treatment of the hexagonal phase above 165 °C, but that this phase, being a metastable phase, progressively converts to the yellow phase with time.⁵ A very recent work addressed the structural behavior of this solid solution and found that the cubic perovskite phase is stable up to $x = 0.8$, whereas the mixed phase is tetragonal for higher stoichiometries. No information has been provided about the phase stability of mixed phases, even though express mention is made of the fact that pure FAPI is not stable in the perovskite phase.⁹

Considering the significant interest in the $\text{FA}_{(1-x)}\text{MA}_x\text{PbI}_3$ mixed system related to the high efficiencies of the PSCs employing such materials as absorbers, we report a detailed investigation of the crystal structure, optical properties, and phase stability of this solid solution as a function of x carried out on samples with well-defined cation stoichiometries (*i.e.*, x values), as determined by NMR spectroscopy.

Experimental Methods

Material Preparation

Samples of general formula $\text{FA}_{(1-x)}\text{MA}_x\text{PbI}_3$ were synthesized according to a general procedure that our group developed previously.^{10,11} In a typical synthesis, a proper stoichiometric amount of lead acetate is dissolved in excess HI under continuous mechanical stirring under a nitrogen atmosphere. Then, the solution was heated to 100 °C, and the corresponding amines (methylammonium and/or formamidinium in water, 40 wt %) were added in the correct stoichiometric amounts. The solution was then cooled to 46 °C at 1 °C/min, until the formation of a precipitate, which was immediately filtered and dried under a vacuum at 60 °C overnight. All reagents were purchased from Sigma-Aldrich in pure form and were used without any further purification.

X-ray Diffraction

The crystal structures of the samples were characterized by room-temperature Cu-radiation Powder X-ray diffraction (XRD) on a Bruker D8 diffractometer. Scans were performed in the 10–90° range, with a step size 0.02° and a counting time of 8 s/step. Data were fitted by the Rietveld method using the FullProf suite of programs.¹²

Diffuse Reflectance Measurements

The optical diffuse reflectance spectra of the different perovskites were measured from 0.8 to 4.5 eV (250–1500 nm, in steps of 1 nm) on a Varian Cary 6000i spectrophotometer equipped with an integrating sphere. For this type of measurement, polycrystalline

powders were compacted into pellets of about 10 mm in diameter, and reflectance spectra were calibrated using a standard reference disk.

NMR Spectroscopy

^1H solid-state NMR room-temperature spectra were acquired on a 9.4 T (1 H = 400.16 MHz) Bruker Avance III spectrometer with the use of TopSpin 3.1 software; spectra were collected with a 4-mm magic-angle spinning (MAS) probe under 8 kHz spinning conditions. ^1H quantitative one-pulse experiments were performed with a pulse length of 4.65 μs , a recycle delay of 120, and 16 scans. The pulse length and recycle delay were carefully calibrated before the acquisition of the final spectra to ensure the full relaxation of the magnetization and to fulfill the conditions for quantitative data acquisition. Chemical shifts are referred to tetramethylsilane (TMS) using adamantane as a secondary standard. The analysis of the obtained data was performed using the DMFit program.¹³

Differential Scanning Calorimetry (DSC)

DSC measurements were performed in a Q2000 apparatus from TA Instruments by heating about 25 mg of powder from -90 to 200 $^{\circ}\text{C}$ in Al open crucibles under a flux of nitrogen.

Results and Discussion

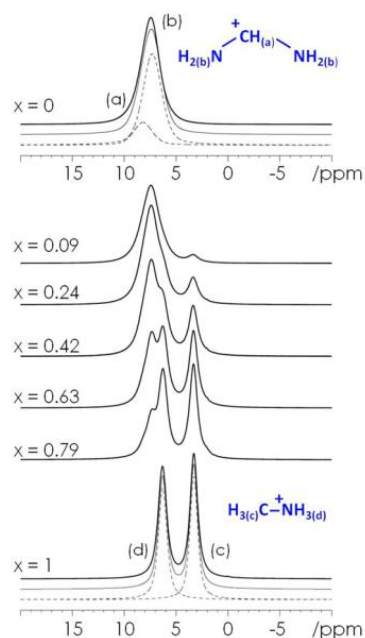


Figure 2.1: Solid state NMR spectra of the $\text{FA}_{1-x}\text{MA}_x\text{PbI}_3$ solid solution. Dashed lines represent contributions and the light solid line represents the overall best fit to the experimental spectra

Samples synthesized according to the experimental procedure were first investigated by solid-state ^1H NMR spectroscopy to determine their actual FA/MA ratios. ^1H MAS spectra for the whole $\text{FA}_{(1-x)}\text{MA}_x\text{PbI}_3$ series are reported in Figure 1, together with the corresponding attributions and the best fits for the two end members.

The spectrum of the FAPI composition presents two peaks at 7.53 and 8.87 ppm with a relative ratio of 4:1, and these signals can be attributed to the

-NH₂ and -CH protons, respectively. Similar chemical shifts were observed for the NMR signal (liquid) of the HC(NH₂)₂I and FAI precursors used for the synthesis of FAPI.^{7,14} Similarly, the attribution of the MAPI composition was made considering the presence of the two resonances at 6.22 and 3.28 ppm with a ratio of 1:1. These two signals have been previously correlated with the -NH₃⁺ and -CH₃⁺ protons, respectively, of the series MAPbX₃ (X = I, Br, Cl).¹⁵ The signals of the two MA and FA species were only partially overlapping at the experimental MAS speed (8 kHz), the observed lines were sufficiently sharp and the acquisition parameters (pulse length and recovery delay) were optimized to obtain fully relaxed signals. Under these conditions, the quantitative analysis of the mixed samples was possible, and the results are reported in Table 2.1.

FA/MA ratio	
nominal	NMR-determined
1.0:0.0 (<i>x</i> = 0, pure FAPI)	1.0:0.0
0.8:0.2	0.91:0.09
0.7:0.3	0.76:0.24
0.5:0.5	0.58:0.42
0.3:0.7	0.37:0.63
0.1:0.9	0.21:0.79
0.0:1.0 (<i>x</i> = 1, pure MAPI)	0.0:1.0

^aBest-fit error < 5%.

Table 2.1: Nominal composition and composition determined from analysis of ¹H NMR spectra for the FA_{1-x}MA_xPbI₃ series

Analysis of the NMR data revealed that the actual compositions of the samples were slightly different from the nominal compositions used for the synthesis, as the MA amount was always slightly overestimated. This result suggests that proper control of the actual MA/FA ratio for this and related systems is a key aspect to be checked after material synthesis, also considering that most of the synthetic procedure is carried out in solution by dripping methods where a proper control of precursor stoichiometry might be hard to achieve. A possible origin of the difference between the nominal and measured stoichiometries might be the different solubilities/reactivities of the MA and FA precursors in solution.

¹H and ¹³C solid-state NMR techniques have been exploited for the study of the phase transitions between different polymorphs for MA lead halide perovskites series,¹⁵ whereas ¹H liquid NMR data for mixed MA/FA iodide precursors have been presented to confirm the alloying of MA and FA in MA-stabilized FAPI.¹⁴ Nevertheless, to our knowledge, this is the first time that ¹H solid-state NMR spectroscopy has been used to address the problem of the quantitative determination of mixed FA/MA compositions.

Based on the NMR results, the x values in the $\text{FA}_{1-x}\text{MA}_x\text{PbI}_3$ solid solution (within the estimated standard deviations) were 0, 0.09, 0.24, 0.42, 0.63, 0.79, and 1.0.

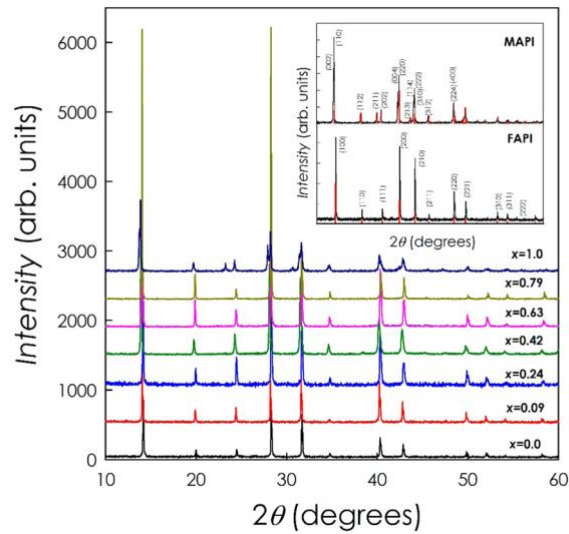


Figure 2.2: XRD patterns for samples of the $\text{FA}_{1-x}\text{MA}_x\text{PbI}_3$ solid solution. Patterns are vertically shifted to clarify viewing. Inset: XRD patterns of the two end members of the solid solution, namely FAPI and MAPI, together with the reflection positions from the literature patterns and Miller indices (red vertical bars)

The X-ray diffraction (XRD) patterns of all of the samples investigated in the present work are reported in Figure 2. All of the samples were single-phase, and for those from $x = 0$ to $x = 0.79$, the unit cell agreed with the crystal structure of the α -phase (black perovskite) of the FAPI end member.

In the inset of Figure 2, the XRD pattern of FAPI is compared with the literature reference pattern using the $\text{Pm}\bar{3}m$ space group, and this black sample was obtained by annealing the yellow, as-synthesized, FAPI sample at 185°C for 1 h. On the other hand, MAPI has a diffraction pattern consistent with the reported tetragonal structure in the $I4mc$ space group.¹⁰ The reported patterns show similar peak shapes and small full width at half-maximum (FWHM) as well, indicating good crystallinity of the phases. Small intensity variations are due to possible preferential orientation effects during sample preparation.

It is interesting to observe that even a small amount of the larger FA cation (ionic radii have been estimated to be 253 and 217 pm for FA and MA, respectively¹⁶) in the solid solution, as in the $x = 0.79$ sample, gave rise, at the end of the synthesis, to a sample with the cubic crystal structure. Moreover, for the low MA-containing samples, black perovskite samples were obtained at the end of the synthesis without the need for any thermal treatment, as in the case of the pure FAPI sample. This means that very low MA contents, such as in the $x = 0.09$ sample, are already able to destabilize the hexagonal

phase. However, as shown later in the text, for small x values, the perovskite phase is not stable with time. By using the effective radii of the organic cations, $r_{\text{eff}} = 217$ pm for MA and $r_{\text{eff}} = 253$ pm for FA, to calculate the tolerance factor, it was found that $\alpha = 0.91$ for MAPbI₃ versus 0.98 for FAPbI₃.⁹ Both values should give a perovskite structure that can be observed for $0.81 < \alpha < 1.01$, which is not the case for δ -FAPbI₃. It is clear that the spherical approximation used to estimate the effective radii of the organic cations is too simplistic in the present case and that the shape and hydrogen-bonding capabilities of each organic species play crucial roles in the definition of the structural properties of these hybrid perovskites.⁹

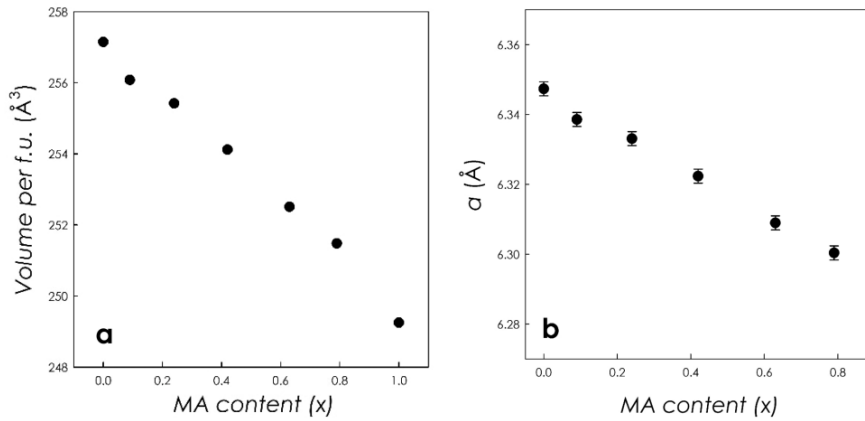


Figure 2.3: (a) Cell volume and (b) cubic lattice parameter of the FA_{1-x}MA_xPbI₃ solid solution as function of x

Panels a and b of Figure 2.3 show the trends in the cell volume (V) and cubic lattice parameter, respectively, of the FA_(1-x)MA_xPbI₃ solid solution, as obtained from Rietveld refinement of the diffraction data, as a function of the x value. The data are reported as cell volumes per formula unit, considering that the Pm $\bar{3}$ m and the I4mc space groups have different Z values. In the Table 2.2 below are reported the values of a and V as obtained from the Rietveld refinement of the patterns, together with an illustrative refined pattern of the pure FAPbI₃.

MA-content (x)	a (Å)	c (Å)	V (Å ³)
0.0000	8.9956(5)		257.14(5)
0.0900	8.9832(4)		256.05(5)
0.2400	8.9812(3)		255.41(4)
0.4200	8.9659(4)		254.11(5)
0.6300	8.9422(4)		252.50(5)
0.7900	8.9299(3)		251.47(4)
1	8.8743(4)	12.6708(8)	249.46(5)

Table 2.2: Results of the Rietveld refinement of the patterns reported in figure 2.2

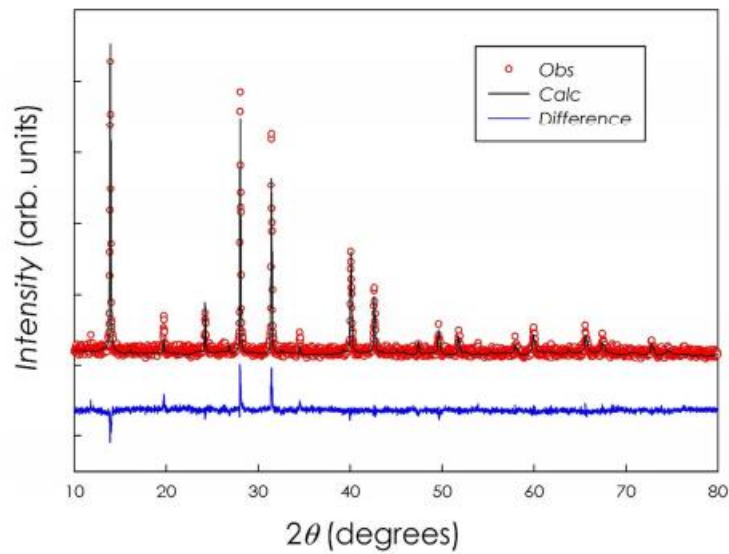


Figure 2.4: Rietveld refined pattern of the pure FAPbI₃

Figure 2.5 shows the differential scanning calorimetry (DSC) measurements for all of the samples except MAPI between -90 and 200 °C (from -90 ° to 100 °C for MAPI), showing the well-known tetragonal-to-cubic phase transition for MAPI at about 57 °C and the hexagonal-to-cubic phase transition for the as-prepared yellow FAPI at about 165 °C. As expected, and in agreement with the XRD results, none of the intermediate compositions present any peaks in the investigated temperature range because the perovskite phase was stabilized by the doping. The results for the thermal stability of the FA_(1-x)MA_xPbI₃ solid solution, determined by means of DSC and not yet reported in the current literature, indicate that the absence of phase transitions is a beneficial aspect of the use of these mixed phases.

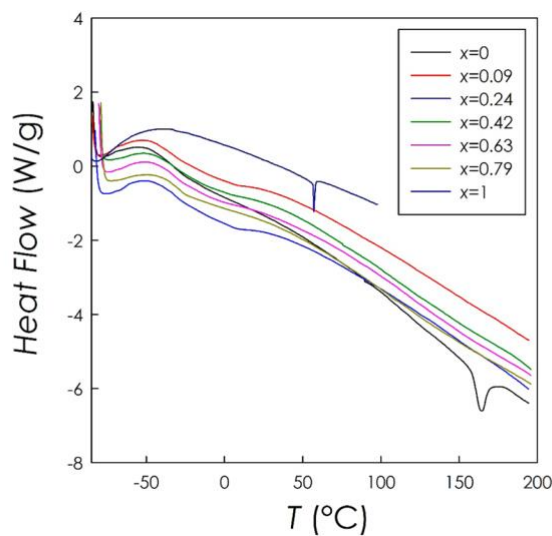


Figure 2.5: DSC measurements of samples of the FA_{1-x}MA_xPbI₃ solid solution. Data for MAPI have been shifted by +1 to clarify the view of the peak corresponding to the tetragonal-to-cubic

Returning to the data of Figure 2.3, one can see that linear decreases of both the cell volume (Figure 2.3a) and the cubic a lattice parameter (Figure 2.3b) occurred with

increasing amount of the smaller MA cation in the solid solution (about 3% volume shrinkage). This behavior is consistent with Vegard's law of solid solution formation, which could be anticipated for this system, but which is confirmed by the present structural data, DSC data, and optical absorbance results.

Other recent literature results based on thin films have indicated slightly different trends. A nonlinear trend, for example, was found in ref 3, where, for example, the $x = 0$ and 0.2 samples had the same cell volume and a significant decrease of V was found for the $x = 0.8$ sample. Binek and coworkers considered the doping of the FAPI phase with 5%, 10%, and 15% MA cation, and their mixed samples, after synthesis, were rich in the hexagonal FAPI phase for all doping levels, a with reduction in the amount of this phase with increasing methylammonium doping.⁶ In their article, they indicated no shrinkage of the unit cell upon the replacement of FA with MA, even for stoichiometries up to about $x = 0.13$. It is important to emphasize that, in both of the works cited here, the thin-film samples were prepared by immersion of the substrate in mixed FAI/MAI solutions and cannot be directly compared to the powdered samples prepared and characterized by the synthetic method used in the present work. In particular, whereas the synthetic approach used herein provides strict control over the stoichiometry, the earlier methods can lead to phases with different stoichiometries. However, the results reported in this work can be used as a reference to rationalize the results obtained for thin films. The stability as a function of time of FAPI (black) perovskites is well-known and was investigated previously.⁶ In general, once the α -phase has been stabilized by thermal annealing at about 180–185 °C, this phase remains stable in the black form for several days with the progressive formation of the yellow hexagonal phase, which is usually observed after 10 days regardless of storage in a vacuum or inert gas.⁶ However, no data are actually available on the time stability of mixed MA/FA systems, which are considered to be very efficient absorbers for use in PSCs.

Figure 2.6 reports the XRD patterns of the $x = 0$ (FAPbI₃), $x = 0.09$, and $x = 0.24$ samples immediately after synthesis and after 10 days of storage in a glovebox and in dark glass containers (aged samples). The blue vertical bars in the plot correspond to the reference pattern for the black α -FAPbI₃, whereas the orange vertical bars correspond to the hexagonal δ -FAPbI₃ reference pattern.

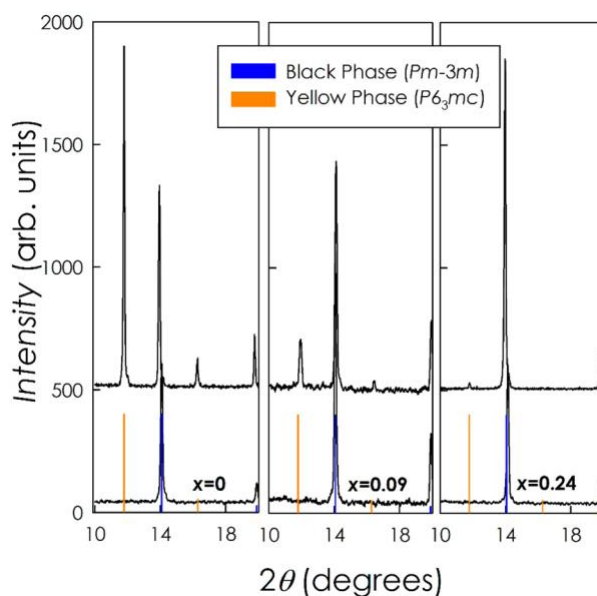


Figure 2.6: XRD pattern of the $x = 0, 0.09$ and 0.24 samples of the $\text{FA}_{1-x}\text{MA}_x\text{PbI}_3$ solid solution immediately after synthesis (bottom) and after 10 days of storage (top). Orange and blue vertical bars correspond to the reference patterns of the hexagonal and cubic structures of FAPbI₃

FAPbI₃ developed a remarkable amount of hexagonal phase after the considered time frame, in agreement with previous data. $\text{FA}_{0.91}\text{MA}_{0.09}\text{PbI}_3$ also developed a significant fraction of the δ -phase, whereas for $\text{FA}_{0.76}\text{MA}_{0.24}\text{PbI}_3$, the amount of the δ -phase was very small. For stoichiometries with $x > 0.24$, no traces of the hexagonal phase were detected. It should be noted that these preliminary results are related to optimal storage conditions and relatively short-time evaluations after synthesis. However, this evidence strongly suggests that, whereas the complete substitution of FA by MA (or other cations) directly stabilizes the (cubic) perovskite phase at room temperature after the synthesis, care must be taken when considering the stability of MA/FA mixed phases. In fact, in this work, we have shown that the time stability of cubic FAPbI₃-based lattices stabilized by low cation replacement might be poor. This suggests that other mixed systems such as Cs-doped and I-/Br-doped FAPbI₃ perovskites should be re-evaluated concerning their phase stability with time.^{17,18} For the samples investigated in this work, optical measurements were carried out to define the band-gap values as a function of (real) stoichiometries. The vis-NIR diffuse reflectance spectra and the trends in the band

gaps as functions of x are reported in panels a and b, respectively, of Figure 2.7. [The $x = 0$ (FAPI) values refer to the cubic “black” phase.] The E_g values were obtained from the extrapolation of the linear part of $[F(R)hv]^2$, where $F(R)$ is the Kubelka–Munk function $F(R) = (1 - R)^2/2R$.^{19,20}

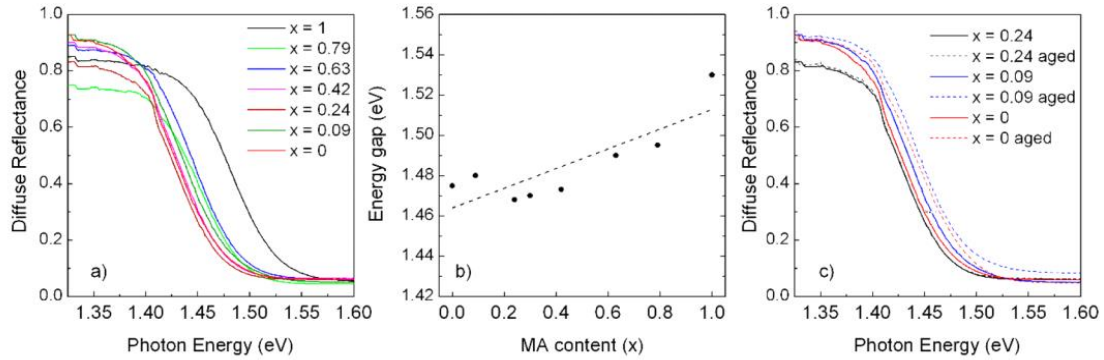


Figure 2.7: (a) Diffuse reflectance spectra for the $FA_{1-x}MA_xPbI_3$ solid solution; (b) trend in the energy gap as a function of x for the $FA_{1-x}MA_xPbI_3$ solid solution and (c) diffuse reflectance spectra of the as-prepared and aged samples for $x=0, 0.09$ and 0.24

FAPI perovskite was found to have a band-gap value of about 1.48 eV, in agreement with the literature, and with increasing amount of MA, the E_g value increased to about 1.53 eV (again in agreement with previously reported values), thus indicating a relatively small shift with MA substitution for FA in the $FA_{(1-x)}MA_xPbI_3$ solid solution.^{1,4,7} Figure 2.7c reports the evolution of the diffuse reflectance spectra of aged samples, analogous to those presented in Figure 2.6 for the XRD characterization. It can be observed that, for $x = 0$ and 0.09 , the spectra showed a shift of the band gap to higher values when the samples were left under optimal storage conditions for several days. On the other hand, for the sample with $x = 0.24$ and greater, there was no shift of the band gap (the dotted curve is exactly superimposed on the solid curve for the as-prepared sample), suggesting a greater stability of the material, at least in this time frame. The results for the optical measurements of aged samples are in very good agreement with the phase separation observed for the aged samples by means of XRD: The samples exhibiting a shift to higher values of E_g are the same as those showing the separation of the hexagonal δ phase with time (see Figure 2.6). This agreement clearly indicates that the time variation of the optical properties of the samples within the $FA_{(1-x)}MA_xPbI_3$ solid solution can be directly correlated with the phase stability of the same samples and that this change in the absorption properties might have a crucial effect on the performance of PSCs employing such materials as absorbing layers. It should be noted that, for low x values, the degradation was found to be very fast (within a few days under optimal storage conditions) and that, for samples with higher x values, the

same behavior might also occur at longer times. Further investigation in this regard is strongly needed for most of the mixed doped systems of hybrid perovskites. Finally, based on the observation of an increase in band-gap values due to phase separation within the samples, it can be suggested that literature data where the band-gap values for FAPI samples are reported to be very high and on the order of 1.53–1.55 eV might be due to significant phase separation occurring within the samples.

Conclusions

The $\text{FA}_{(1-x)}\text{MA}_x\text{PbI}_3$ system has been deeply investigated, defining its crystal structure, phase stability, and optical properties as functions of the actual x values determined by means of solid-state NMR spectroscopy. The collected results confirm the formation of a solid solution within this mixed system. By properly controlling the relative MA and FA amounts, we obtained reliable evidence of structural changes occurring upon doping. In addition, we characterized the time stability of mixed systems, highlighting a phase separation phenomenon in aged samples leading to the formation of the δ -phase. The optical properties were also found to scale with the real x values, and the time degradation of the samples resulted in an increase of the band-gap values due to the phase separation observed by diffraction. These results, providing a reliable definition of structure–property correlations in the $\text{FA}_{(1-x)}\text{MA}_x\text{PbI}_3$ system for well-defined doping levels, demonstrate the significant stability issue of such mixed systems that could also be a key issue for other mixed systems based on FAPI perovskite. These effects might, in turn, have detrimental effects on the performance of PSCs based on these materials as active layers.

References

1. Jeon, N. J.; Noh, J. H.; Yang, W. S.; Kim, Y. C.; Ryu, S.; Seo, J.; Seok, S., II Compositional engineering of perovskite materials for high-performance solar cells. *Nature* 2015, 517, 476.
2. Pellet, N.; Gao, P.; Gregori, G.; Yang, T.-Y.; Nazeeruddin, M. K.; Maier, J.; Graetzel, M. Mixed-organic-cation perovskite photovoltaics for enhanced solar-light harvesting. *Angew. Chem., Int. Ed.* 2014, 53, 3151.
3. Jacobsson, T. J.; Correa-Baena, J.-P.; Pazoki, M.; Saliba, M.; Schenk, K.; Graetzel, M.; Hagfeldt, A. Exploration of the compositional space for mixed lead halogen perovskites for high efficiency solar cells. *Energy Environ. Sci.* 2016, 9, 1706.

4. Yang, W. S.; Noh, J. H.; Jeon, N. J.; Kim, Y. C.; Ryu, S.; Seo, J.; Seok, S. II High-performance photovoltaic perovskite layers fabricated through intramolecular exchange. *Science* 2015, 348, 1234.
5. Han, Q.; Bae, S.-H.; Sun, P.; Hsieh, Y.-T.; Yang, Y.; Rim, Y. S.; Zhao, H.; Chen, Q.; Shi, W.; Li, G.; et al. Single crystal formamidinium lead iodide (FAPbI₃): insight into the structural, optical, and electrical properties. *Adv. Mater.* 2016, 28, 2253–2258.
6. Binek, A.; Hanusch, F. C.; Docampo, P.; Bein, T. Stabilization of the trigonal high-temperature phase of formamidinium lead iodide. *J. Phys. Chem. Lett.* 2015, 6, 1249.
7. Lee, J.-W.; Seol, D.-J.; Cho, A.-N.; Park, N.-G. High-efficiency perovskite solar cells based on the black polymorph of HC-(NH₂)₂PbI₃. *Adv. Mater.* 2014, 26, 4991.
8. Yang, Z.; Chueh, C.-C.; Liang, P.-W.; Crump, M.; Lin, F.; Zhu, Z.; Jen, A. K.-Y. Effects of formamidinium and bromide ion substitution in methylammonium lead triiodide toward high-performance perovskite solar cells. *Nano Energy* 2016, 22, 328–337.
9. Weber, O. J.; Charles, B.; Weller, M. T. Phase behaviour and composition in the formamidinium–methylammonium hybrid lead iodide perovskite solid solution. *J. Mater. Chem. A* 2016, 4, 15375.
10. Mancini, A.; Quadrelli, P.; Amoroso, G.; Milanese, C.; Boiocchi, M.; Sironi, A.; Patrini, M.; Guizzetti, G.; Malavasi, L. Synthesis, structural and optical characterization of APbX₃ (A = methylammonium, dimethylammonium, trimethylammonium; X = I, Br, Cl) hybrid organic-inorganic materials. *J. Solid State Chem.* 2016, 240, 55.
11. Mancini, A.; Quadrelli, P.; Milanese, C.; Patrini, M.; Guizzetti, G.; Malavasi, L. CH₃NH₃Sn_xPb_{1-x}Br₃ hybrid perovskite solid solution: synthesis, structure, and optical properties. *Inorg. Chem.* 2015, 54, 8893.
12. Rodriguez-Carvajal, J. Recent advances in magnetic structure determination by neutron powder diffraction. *Phys. B* 1993, 192, 55.
13. Massiot, D.; Fayon, F.; Capron, M.; King, I.; Le Calve, S.; Alonso, B.; Durand, J. O.; Bujoli, B.; Gan, Z.; Hoatson, G. Modelling one- and two-dimensional solid-state NMR spectra. *Magn. Reson. Chem.* 2002, 40, 70.
14. Fu, Y.; Zhu, H.; Schrader, A. W.; Liang, D.; Ding, Q.; Joshi, P.; Hwang, L.; Zhu, X.-Y.; Jin, S. Nanowire lasers of formamidinium lead halide perovskites and their stabilized alloys with improved stability. *Nano Lett.* 2016, 16, 1000.

15. Baikie, T.; Barrow, N. S.; Fang, Y.; Keenan, P. J.; Slater, P. R.; Piltz, R. O.; Gutmann, M.; Mhaisalkar, S. G.; White, T. J. A combined single crystal neutron/X-ray diffraction and solid-state nuclear magnetic resonance study of the hybrid perovskites $\text{CH}_3\text{NH}_3\text{PbX}_3$ ($X = \text{I, Br and Cl}$). *J. Mater. Chem. A* 2015, 3, 9298–9307.
16. Kieslich, G.; Sun, S.; Cheetham, A. K. An extended tolerance factor approach for organic–inorganic perovskites. *Chem. Sci.* 2015, 6, 3430.
17. Rehman, W.; Milot, R. L.; Eperon, G. E.; Wehrenfennig, C.; Boland, J. L.; Snaith, H. J.; Johnston, M. B.; Herz, L. M. Charge-carrier dynamics and mobilities in formamidinium lead mixed-halide perovskites. *Adv. Mater.* 2015, 27, 7938–7944.
18. Yi, C.; Luo, J.; Meloni, S.; Boziki, A.; Ashari-Astani, N.; Graetzel, C.; Zakeeruddin, S. M.; Roethlisberger, U.; Graetzel, M. Entropic stabilization of mixed A-cation ABX_3 metal halide perovskites for high performance perovskite solar cells. *Energy Environ. Sci.* 2016, 9, 656– 662.
19. Kubelka, P.; Munk, F. Ein beitrag zur optik der farbanstriche. *Z. Techn. Phys.* 1931, 12, 593–601. (20) Kim, H.-S.; Lee, C.-R.; Im, J.-H.; Lee, K.-B.; Moehl, T.; Marchioro, A.; Moon, S.-J.; Humphry-Baker, R.; Yum, J.-H.; Moser, J. E.; et al. Lead iodide perovskite sensitized all-solid-state submicron thin film mesoscopic solar cell with efficiency exceeding 9%. *Sci. Rep.* 2012, 2, 591.

CHAPTER 3.

B-SITE CATION SUBSTITUTION

Doping of the B-site is more difficult compared to that of the A and X-sites owing to its large formation energy. In general, there are two categories for Pb replacement: using either homovalent elements such as Sn and Ge or heterovalent elements such as Bi and Sb. While the homovalent replacement by Sn or Ge leads to instability, the heterovalent Pb replacement leads to degraded electronic properties mainly due to the reduction on electronic dimensionality. As a result, all the reported Pb-free perovskite and perovskite derivative solar cells in the literature show inferior photovoltaic performances as compared to Pb halide perovskite solar cells. However, in few years, thanks to the increased interest towards Sn-based PSC, the efficiency of them is now close to 10%, suggesting that there is space for further improvement also for lead-free materials-based cells.

So why should be interesting to perform this kind of substitution? Lead toxicity and environmental hazards of lead-containing products, which requires the development of special recycling protocols (61), together with the poor device stability due to water soluble Pb^{2+} are still two major challenges. Herein, two approaches may be effective to address the above-mentioned challenges: suitable encapsulation and new lead-free materials.

Leaving the encapsulation problem to the engineers, we chose to focus our attention on the synthesis of new Sn-Pb mixed doped perovskites because Sn perovskite solar cells have shown the best performance among all Pb-free halide perovskite solar cells. Tin and lead are in the same group in the periodic table and have similar electronic arrangements and similar ionic radius ($\sim 1.35 \text{ \AA}$ vs $\sim 1.49 \text{ \AA}$ respectively), encouraging the replacement with no significant perturbation in lattice structure. Despite this similarity, Sn-based perovskites exhibit a subtle difference in chemical bonding and semiconducting properties compared to Pb-based perovskites due to a larger degree of orbital overlap in the Sn-X bond than the Pb-X one. Specifically, the outer ns^2 electron

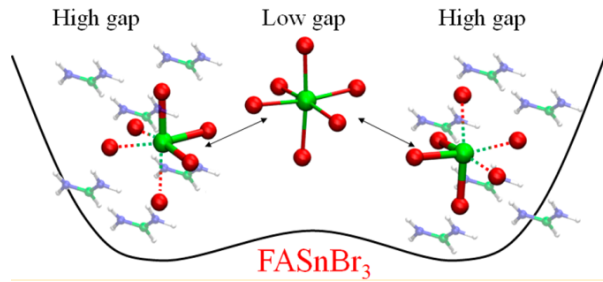
configuration, with low ionization energy, is helpful for Sn-based perovskites to obtain large optical absorption, a low exciton binding energy (~ 18 meV), a high charge mobility ($\sim 10^2$ – 10^3 $\text{cm}^2 \cdot \text{V}^{-1} \cdot \text{s}^{-1}$) and a narrow band gap (~ 1.3 – 1.4 eV). (62) It is nevertheless relevant that, to date, Sn-based PSCs have not yet benefited from the same intensive research effort that has propelled Pb-based perovskites, but the progress in this area is evident with the highest PCEs achieved to date, already comparable and competitive with the efficiency of “conventional” lead-based perovskites. The lead-free HP-based solar cells could soon become competitive to their Pb-based analogs in the near future because even with an inferior PCE, lead-free HPs are not acutely toxic and do not pose the severe concerns of possible environmental damage and the post-utilization recycling problems that Pb-based HPs do. (63)

3.1 FAPb_(1-x)Sn_xBr₃

Exploring the Limits of Three-Dimensional Perovskites: The Case of FAPb_{1-x}Sn_xBr₃

Purpose and Scope

As shown in the previous chapter, metal halide perovskites based on formamidinium (FA) show interesting properties compared to methylammonium (MA) compounds like the stabilization of the cubic



perovskite phase at room temperature, the extension of the absorption edge, the improvement of thermal and moisture stability and the enhancement of carrier lifetime. The larger molecular size of FA compared to that of MA leads, however, to a structural instability in FAPbI₃, placing FA at the border of tolerance factor for three-dimensional (3D) lead iodide perovskites. Because of the huge interest in mixed Sn/Pb perovskites, here we decided to investigate FAPb_{1-x}Sn_xBr₃ perovskites in a full compositional range ($0 \leq x \leq 1$).

In 2015, some weeks after my arrival in the group, Alessandro Mancini (64) investigated the role of tin alloying in MAPbBr₃, showing a progressive reduction of the band gap from 2.20 to 1.33 eV (red points), which is the band gap reduction expected upon increasing the Sn fraction

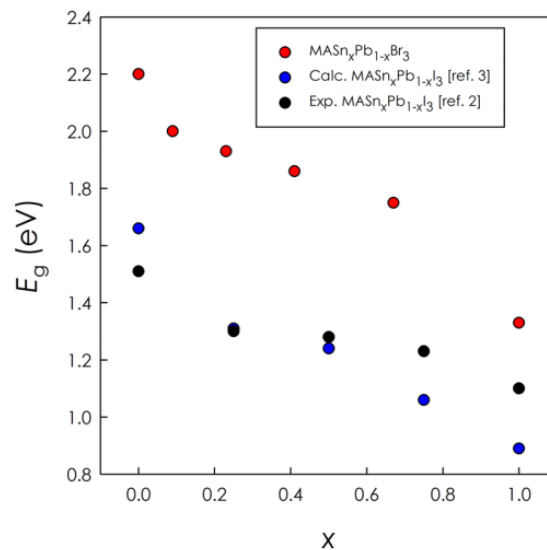


Figure 3.1: Trend in the energy gap as a function of x for the $MA\text{Sn}_x\text{Pb}_{1-x}\text{Br}_3$ solid solution (64)

On the other hand, a more recent study on the $\text{FA}_{1-x}\text{MA}_x\text{SnBr}_3$ mixed-cation system (reported in the paragraph 4.1) revealed an unusual and unexpected trend in the evolution of the band gap as a function of the organic cation.¹⁹ In particular, it was observed that starting from FASnBr_3 , the band gap value progressively decreased from about 2.4 eV ($x = 0$) to ~ 1.92 eV ($x = 0.82$) followed by an up-turn to ~ 2.0 eV for MASnBr_3 , which is, overall, a huge energy variation for a simple A-cation replacement. Such variations are usually observed for B-cation or X-anion substitutions.^{14,18,20} The results reported on the $\text{FA}_{1-x}\text{MA}_x\text{SnBr}_3$ solid solution seem to confirm the key role of structural distortions induced by A-site cations on the perovskite optical properties.¹¹

Motivated by these results, indicating a possible new scenario in the electronic structure evolution of FA-based tin halides; by the appeal of FAPbBr_3 for both photovoltaics and optoelectronic devices; and by the interest toward the replacement of Pb with Sn, thanks to the great help of professor De Angelis, we undertook a joint experimental and computational investigation of the $\text{FAPb}_{1-x}\text{Sn}_x\text{Br}_3$ system (*i.e.*, $0 \leq x \leq 1$). We have found a non-monotonic band gap evolution with the Sn content. The pure FASnBr_3 perovskite shows a higher band gap than the corresponding FAPbBr_3 compound, with intermediate compositions showing a lower band gap than FAPbBr_3 . Surprisingly, the high band gap of FASnBr_3 turns out to be the result of dynamical averaging of a strongly distorted structure, made by almost isolated SnBr_3 units characterized by very short interunit Sn–Br distances, similar to the reported structure of FAGeI_3 .²¹ This is the result of the FA cation being too large to fit into the SnBr_3 cavity and of the high-lying Sn 5s orbitals strongly contributing to the top of the valence band in tin halide perovskites. Notably, this distortion is lifted in the FAPbBr_3 perovskite because of the lower energy of Pb 6s orbitals, with FASnBr_3 probably representing the limit compound of 3D tin halide perovskites.

Experimental Section

Samples of general formula $\text{FAPb}_{1-x}\text{Sn}_x\text{Br}_3$ (with nominal $x=0, 0.05, 0.15, 0.3, 0.4, 0.6, 0.9, 1$) were synthesized according to a general and original procedure we developed.²²⁻²³ In a typical synthesis, a proper stoichiometric amount of Pb acetate and Sn acetate are dissolved in an HBr excess under continuous mechanical stirring under nitrogen atmosphere. Hypophosphoric acid is added to the solution and inert atmosphere is maintained in the reaction environment in order to prevent Sn oxidation. Then, the solution is heated to 100°C and the corresponding FA acetate solution (40%wt in water) is added in the stoichiometric amount. The solution is then cooled down to 46°C at 1°C/min, until the formation of a precipitate, which is immediately filtered and

dried under vacuum overnight. Finally, the samples are treated at 100°C for 2 h before the characterization. The final products are handled and stored in a glove box with oxygen and water contents lower than 1 ppm. All the reagents were purchased from Sigma Aldrich in pure form and were used without any further purification. The crystal structure of the samples has been characterized by room temperature Cu-radiation X-ray Powder Diffraction (XRD) in a Bruker D8 diffractometer by using a Bruker dome sealed in the glove box avoiding air exposure. The optical diffuse reflectance spectra of the different perovskites were measured from 0.8 to 4.5 eV (250-1500 nm, with step of 1 nm) by a Varian Cary 6000i equipped with an integrating sphere. For this kind of measurements polycrystalline powders were compacted into pellets of about 5 mm in diameter and reflectance spectra were calibrated using a standard reference disk. The real elemental composition of the samples was determined by Energy-dispersive X-ray spectroscopy using an INCA Energy 350 X Max detector from Oxford Instruments linked to the SEM. Cobalt standard was used for the calibration of the quantitative elementary analysis. All the samples manipulations were carried out under inert atmosphere thanks to a homemade sample holder allowing the transport of the powders from the glove box to the SEM chamber. Those analyses are essential to correlate the physical properties with the real stoichiometry instead of nominal cations ratio.

Results and Discussion

FAPbBr₃ crystallizes in a cubic space group at room temperature ($Pm\bar{3}m$) and undergoes two phase transitions by lowering the temperature (cubic to tetragonal between 275 and 250 K and tetragonal to orthorhombic between 150 and 125 K).²⁴ FASnBr₃ also presents a cubic $Pm\bar{3}m$ symmetry at room temperature, thus anticipating the possible existence of mixed Sn/Pb systems.¹⁹ The room-temperature laboratory X-ray diffraction patterns of the samples of the FAPb_{1-x}Sn_xBr₃ system investigated in the present work are shown in Figure 3.2, where x values refer to the effective Sn/Pb composition determined by energy-dispersive X-ray spectroscopy (see the Supporting Information).

All the patterns reported in Figure 3.2 display the typical reflections of the cubic structure of metal halide perovskites ($Pm\bar{3}m$, vertical red bars) and are free from detectable impurities.

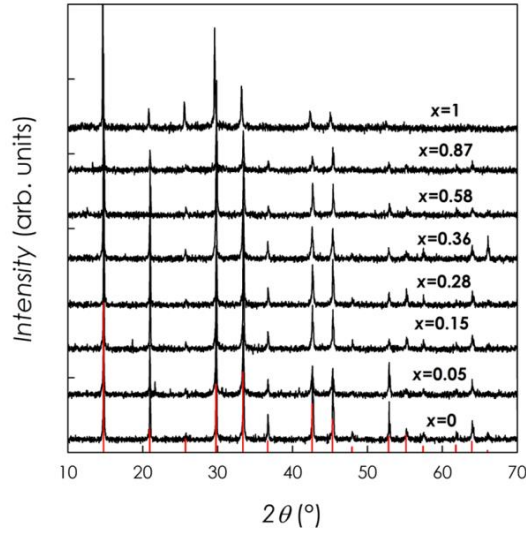


Figure 3.2: XRD patterns for the samples of the $FAPb_{1-x}Sn_xBr_3$ system. Patterns are vertically shifted to clarify viewing. Red vertical bars refer to the reflection positions for cubic structure

A slight peak broadening can be observed by increasing the Sn content, as also found in previous Pb/Sn systems, but all the samples retain a high level of crystallinity.^{18,19} By analogy with $FAGeI_3$, we cannot rule out a slight trigonal distortion,²¹ which however cannot be distinguished at the current level of X-ray diffraction (XRD) resolution. The cubic lattice parameter and cell volume determined from the refinement of the patterns are reported in Table 3.1.

x	a	V
0.00	5.9953(2)	215.50(1)
0.05	5.9946(2)	215.42(1)
0.15	5.9979(2)	215.78(1)
0.28	5.9976(2)	215.74(1)
0.36	5.9966(2)	215.64(1)
0.58	5.9970(2)	215.68(1)
0.87	6.0076(2)	216.82(1)
1.00	6.0344(2)	219.74(1)

Table 3.1: Lattice parameters (a , Å) and cell volumes (V , Å³) for the investigated $FAPb_{1-x}Sn_xBr_3$ samples as a function of the Sn content

The cell parameter and volume of the $FAPb_{1-x}Sn_xBr_3$ system remain substantially constant up to about $x = 0.58$, where it starts increasing with a further relevant expansion for $x = 1$, *i.e.*, for the pure $FASnBr_3$ compound. This is an anomalous behavior with respect to other Pb/Sn mixed halide perovskites where a slight decrease of the cell volume by increasing the Sn content has been reported,^{18,25} also according to the small ionic radius difference between Sn(II) and Pb(II).²⁶ Because the samples are single phase and the actual Sn/Pb content has been determined experimentally, assuming there are no significant deviations from the nominal stoichiometry, the structural results suggest

that some level of distortion could be present also for the averagely cubic structure and that this distortion should manifest itself with a peculiar trend by increasing the Sn content above $x = 0.50$.

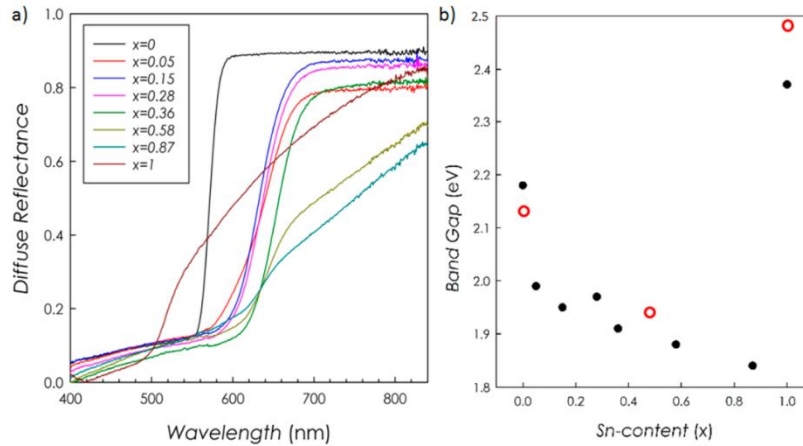


Figure 3.3: (a) Diffuse reflectance spectra for the $\text{FAPb}_{1-x}\text{Sn}_x\text{Br}_3$ system. (b) Experimental band gap trend as a function of Sn content (x) in black solid circles, red open circles represent calculated band gaps by HSE06_SOC

Related to the structural evolution, the $\text{FAPb}_{1-x}\text{Sn}_x\text{Br}_3$ system shows a correspondingly anomalous band gap trend upon varying the Pb/Sn ratio. Figure 3.3a reports diffuse reflectance spectra, and Figure 3.3b reports the extrapolated band gap values as a function of the Sn content. The band gaps have been obtained from the extrapolation of the linear part of $[F(R) h\nu]^2$, where $F(R)$ is the Kubelka–Munk function $F(R) = (1 - R)^2/2R$.^{27,28} From Figure 3.3a, one observes a progressive shift of the fundamental absorption edge toward lower energies by replacing Sn on the Pb site up to $x = 0.87$, together with a reduction of the overall reflectance of the samples and a broadening of the absorption line shape, consistent with the increased Urbach tail energy found for tin halides.²⁹ An abrupt shift of the absorption edge toward higher energy is instead found for FASnBr_3 . The band gap value shows a progressive reduction by increasing x from about 2.18 eV (FAPbBr_3) to 1.88–1.84 eV ($x = 0.58$ – 0.87), followed by a sudden upturn for FASnBr_3 (2.37 eV), Figure 3.3b. Again, such behavior is anomalous and intriguing because in mixed Pb/Sn systems one would expect a monotonic band gap variation with increasing the Sn content,¹⁴ as experimentally found by Ogomi et al.¹² Hao et al.,¹³ however, observed an anomalous band gap behavior by varying the Pb/Sn ratio in $\text{MASn}_{(1-x)}\text{Pb}_x\text{I}_3$ with intermediate compositions ($x = 0.25$ and 0.50) showing the lowest band gap.

To gain insight into the reasons underlying the anomalous band gap evolution with Pb/Sn alloying, we have carried out hybrid density functional theory calculations including spin– orbit coupling (SOC). We relaxed atomic positions by PBE,³⁰ followed

by single-point hybrid calculations including SOC using the modified version of the HSE06 functional³¹ including 43% Hartree–Fock exchange as proposed in ref 32. This approach is found to correctly reproduce the results of GW calculations for both lead and tin iodide perovskites.³³ We start our analysis by looking at results obtained for a cubic $2 \times 2 \times 2$ supercell. Atomic positions are allowed to relax, keeping the experimental cell parameters fixed. No significant differences are noted when relaxing the cell parameters, thus, we refer to experimental cell parameters for simplicity. For the mixed $\text{FAPb}_{0.5}\text{Sn}_{0.5}\text{Br}_3$ compound, we explored several possible arrangements of the four Sn and Pb ions, but for simplicity we refer to the most stable structure, we notice that the presence of such low-energy structures may induce significant disorder in the mixed Sn/Pb phases. As one may notice, the calculated band gaps are in good agreement with experimental values (Figure 3.3b). In line with experiments, we predict a decrease of the band gap from 2.12 eV in FAPbBr_3 to 1.94 eV when moving to $x = 0.5$, to then increase to 2.48 eV for the pure FASnBr_3 perovskite. The calculated band gap trend can be explained by looking at the density of states (DOS) reported in Figure 3.4.

Introduction of Sn in $\text{FAPb}_{0.5}\text{Sn}_{0.5}\text{Br}_3$ stabilizes the conduction band minimum (CBM), with mixed Pb 6p/Sn 5p character, while the valence band maximum (VBM) remains essentially unaltered. The stable VBM level in mixed Sn/Pb compositions is advantageous in terms of stability of the alloy with respect to the pure Sn perovskites. Upon further increases of the Sn content, the CBM is totally constituted by Sn 5p orbitals and shifts at higher energy. Concomitantly, the VBM shifts at higher energy, as a result of the mixing between Sn 5s and Br 4p states, but the VBM shift is smaller than the CBM shift; therefore, overall, the band gap increases. This is at variance with the $\text{FAPb}_{1-x}\text{Sn}_x\text{I}_3$ perovskites, where the VBM upshift was significantly larger than the CBM upshift, leading to a consistent band gap reduction in MASnI_3 compared to MAPbI_3 .³³

To further investigate the origin of the band gap evolution, we inspected the optimized structures of the investigated perovskites in Figure 3.4. FASnBr_3 was found to exhibit a strong long–short alternation of Sn–Br distances (2.76 and 3.30 Å, Figure 3c) which gradually equalizes when moving to $\text{FAPb}_{0.5}\text{Sn}_{0.5}\text{Br}_3$ (2.98 and 3.04 Å, Figure 3b) and FAPbBr_3 (3.02 and 3.03 Å, Figure 3a). While long–short alternation of apical metal halide distances is typical of tetragonal Sn and Pb halide perovskites,^{14,31} the calculated difference found in FASnBr_3 (~ 0.5 Å) is outstanding. Notably, such structural distortion is not related to a specific crystallographic direction, but it is symmetrically distributed along the three crystal axes (see Figure 3.4), at variance with the long–short bond alternation along the [001] direction found in tetragonal metal halide perovskites.³³ The structural distortion, leading to a polar structure similar to that reported for FAGeI_3 ,²¹

actually drives the system toward a structure which is intermediate between that of 0D and 3D perovskites, because SnBr_3 units with short Sn–Br distances (2.76 Å) are separated by long Sn–Br distances (3.30 Å) from other units (see Figure 3b,c).

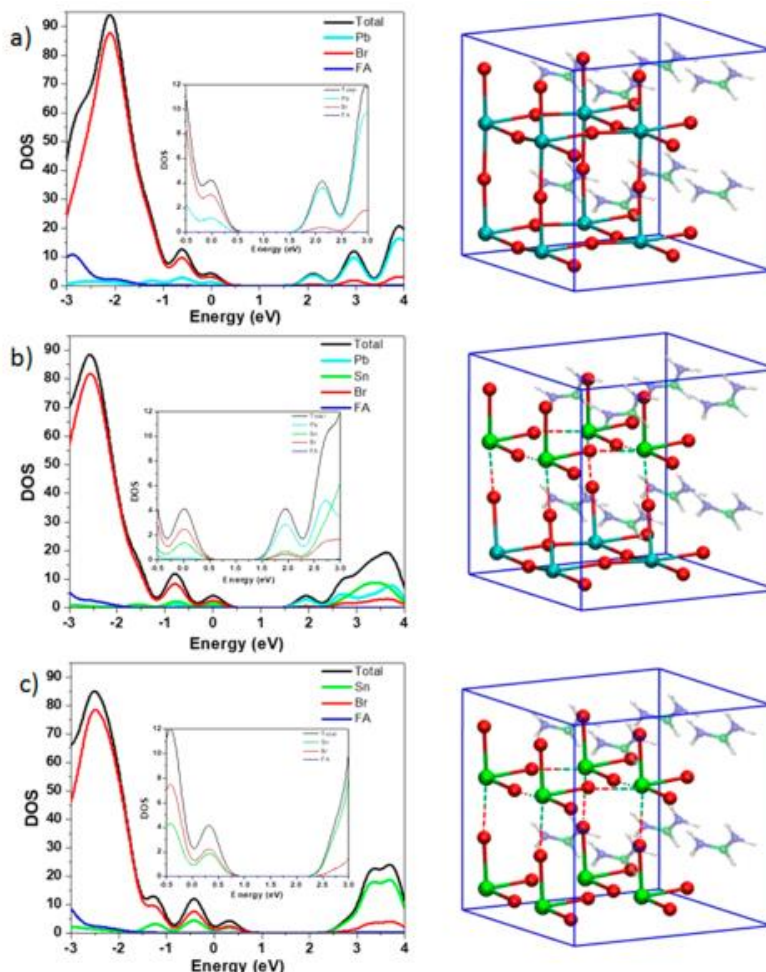


Figure 3.4. Left panels: Density of states (DOS) of cubic (a) FAPbBr_3 , (b) $\text{FAPb}_{0.5}\text{Sn}_{0.5}\text{Br}_3$ and (c) FASnBr_3 , as calculated by HSE06-SOC. Valence band maxima have been set to zero in panel a and have been aligned to the lowest carbon DOS peak in panels b and c. Right panels: optimized structures of cubic (a) FAPbBr_3 , (b) $\text{FAPb}_{0.5}\text{Sn}_{0.5}\text{Br}_3$ and (c) FASnBr_3 . The dashed lines indicate long Sn–Br distances. Pb light blue; I red and Sn green. FA molecules are shaded in the background for clarity. The blue boxes represent the $2 \times 2 \times 2$ supercell used for calculations

Because the band gap (and band structure) is the result of the metal halide connectivity, a partly decoupled network of SnBr_3 units has a band gap higher than that of a continuous 3D perovskite. As a matter of fact, for FASnBr_3 , the band gap is intermediate between that of the fully coupled CsSnBr_3 system (~ 1.7 eV) and that of a putative 0D FASnBr_3 phase made by totally uncoupled units, which we calculate here to have a band gap of 4.60 eV (see the Supporting Information for further details).

To gain clearer insight into the origin of the large metal halide bond alternation of FASnBr_3 , we simulated a series of cubic perovskites, varying A (FA, MA, Cs), M (Ge, Sn, Pb), and X (Br, I) (see Table 3.2). Notably a clear trend emerges, with the A-site cation modulating the distortion in ASnBr_3 perovskites; larger cations give larger distortions, with CsSnBr_3 being almost perfectly symmetric. The structural distortion has important consequences for the ASnBr_3 perovskites band gaps, which experimentally decrease from ~ 2.4 to ~ 1.7 eV across the $\text{FA} \rightarrow \text{MA} \rightarrow \text{Cs}$ series. The observed structural

A	M	X	M-X (Å)	E_g
FA	Sn	Br	2.79, 3.26	2.37
MA	Sn	Br	2.82, 3.08	2.00 ^b
Cs	Sn	Br	2.87, 2.93	1.75 ^c
FA	Sn	I	3.07, 3.21	1.41 ^d
MA	Sn	I	3.02, 3.22	1.20 ^d
Cs	Sn	I	3.06, 3.14	1.27 ^e
FA	Pb	Br	3.00, 3.02	2.18
MA	Pb	Br	2.93, 3.01	2.20 ^f
FA	Pb	I	3.18, 3.25	1.48 ^{d,h}
MA	Pb	I	3.12, 3.23	1.52 ^d
FA	Ge	I	2.75, 3.26 ^g	2.2 ^g
MA	Ge	I	2.77, 3.45 ^g	1.9 ^g
Cs	Ge	I	2.73, 3.58 ^g	1.6 ^g

Table 3.2: Calculated short-long metal halide bond lengths (M-X, Å) and experimental band gaps (E_g , eV) for a series of cubic perovskites varying A, M, X

asymmetry is partly lifted in ASnI_3 perovskites, with the largest deviation of the series (3.07 and 3.21 Å) being again observed for the FASnI_3 perovskite. The structural asymmetry is further reduced in APbX_3 perovskites, with a consequent band gap leveling (see Table 3.2).

Notably, in AGeI_3 perovskites, the structural distortion was present even for CsGeI_3 (smaller cation, larger anion) characterized by short-long distances of 2.75–3.26 Å, and it further increased moving to larger cations, up to 2.73–3.58 Å in FAGeI_3 .²¹ Taken altogether, these data seem to suggest a typical tolerance factor argument,^{34–36} with the smaller tin bromide inorganic sublattice being more sensitive to the size of the A-cations than lead halide and tin iodide compounds.

The observed structural distortion is apparently not consistent with the reported cubic phase of the investigated perovskites. Notice, however, that dynamical averaging may lead to an overall cubic structure, similar to the dynamically averaged cubic structure of MAPbI_3 ,³⁹ where the nominally cubic structure is actually the average of two distorted tetragonal structures. To check this point, we have carried out ab initio molecular dynamics simulations on a $3 \times 3 \times 3$ cubic FASnBr_3 supercell by means of the Car-Parrinello method,^{40,41} setting the temperature at 350 K. We looked at the structural evolution of a set of Sn-Br distances spanning the [100], [010], and [001] directions against their global average during the dynamics. In Figure 3.5 are reported the results for the [001] direction.

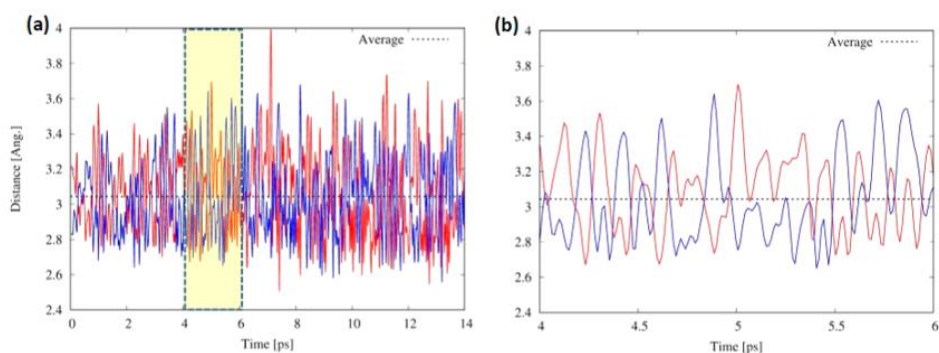


Figure 3.5: (a) Time evolution of Sn-Br bond distances along the [001] direction for a selected Sn center. (b) Detail of the time from 4 to 6 ps highlighted by the yellow rectangle in the left panel. Notice the inversion of initially long (red) and short (blue) distances in time

As can be seen, the average of the Sn-Br distances during the dynamics (3.04 Å) matches the average of the long and short distances calculated by structural optimizations. Furthermore, and more importantly, Figure 3.5b clearly shows that long Sn-Br bonds become short and vice versa within a typical time of ~ 0.15 ps. Thus, the structure is indeed cubic on average, though it is instantaneously distorted. This implies that on the long-time scale of structural characterizations, *e.g.* XRD, the structure is overall cubic, while on the short time scale of electronic transitions, *i.e.* upon resonantly exciting the material during absorption measurements, the structure is distorted, delivering an increased band gap value. This is confirmed by investigating the band gap variation against a collective distortion parameter, so that the average band gap is actually larger than the band gap of the average structure.³⁹ Similar analysis performed on FAGEI₃ revealed a more pronounced barrier across the double-well profile (0.06 vs 0.01 eV), suggesting that this system might be trapped in the distorted energy well for sufficient time to be observed through structural determination.

Conclusions

FASnBr₃ (and possibly MASnBr₃ and to some extent FAGEI₃) is the first example of such 3D perovskites originated by dynamical averaging of quasi-0D structures. As such, FASnBr₃ likely represents a limit compound in the compositional space of 3D perovskites. Notably, while FAPbI₃ manifests a structural instability toward a yellow non-perovskite phase, the different electronic structure of FASnBr₃ allows the system to “solve” the instability issue related to the large FA cation size by adopting a distorted structure characterized by partly uncoupled SnBr₃ units. Of possible technological relevance, intermediate FAPb_{1-x}Sn_xBr₃ compositions maintain an interesting band gap of ca. 1.8 eV up to a Sn content of ca. 85%, representing a potential lead-mitigated perovskite composition for tandem solar cells.

References

1. Jeon, N. J.; Noh, J. H.; Yang, W. S.; Kim, Y. C.; Ryu, S.; Seo, J.; Seok, S. I. Compositional Engineering of Perovskite Materials for High-Performance Solar Cells. *Nature* 2015, 517, 476–480.
2. Pellet, N.; Gao, P.; Gregori, G.; Yang, T.-Y.; Nazeeruddin, M. K.; Maier, J.; Gratzel, M. Mixed-Organic-Cation Perovskite Photovoltaics for Enhanced Solar-Light Harvesting. *Angew. Chem., Int. Ed.* 2014, 53, 3151–3157.
3. Jesper Jacobsson, T.; Correa-Baena, J.-P.; Pazoki, M.; Saliba, M.; Schenk, K.; Gratzel, M.; Hagfeldt, A. Exploration of the Compositional Space for Mixed Lead Halogen Perovskites for High Efficiency Solar Cells. *Energy Environ. Sci.* 2016, 9, 1706–1724.
4. Yang, W. S.; Noh, J. H.; Jeon, N. J.; Kim, Y. C.; Ryu, S.; Seo, J.; Seok, S. I. High-Performance Photovoltaic Perovskite Layers Fabricated through Intramolecular Exchange. *Science* 2015, 348, 1234–1237.
5. Arora, N.; Dar, M. I.; Abdi-Jalebi, M.; Giordano, F.; Pellet, N.; Jacopin, G.; Friend, R. H.; Zakeeruddin, S. M.; Gratzel, M. Intrinsic and Extrinsic Stability of Formamidinium Lead Bromide Perovskite Solar Cells Yielding High Photovoltage. *Nano Lett.* 2016, 16, 7155–7162.
6. Cho, K. T.; Paek, S.; Grancini, G.; Roldan-Carmona, C.; Gao, P.; Lee, Y.; Nazeeruddin, M. K. Highly Efficient Perovskite Solar Cells with a Compositionally Engineered Perovskite/Hole Transporting Material Interface. *Energy Environ. Sci.* 2017, 10, 621–627.
7. Pisanu, A.; Ferrara, C.; Quadrelli, P.; Guizzetti, G.; Patrini, M.; Milanese, C.; Tealdi, C.; Malavasi, L. The $\text{FA}_{1-x}\text{MA}_x\text{PbI}_3$ System: Correlations among Stoichiometry Control, Crystal Structure, Optical Properties, and Phase Stability. *J. Phys. Chem. C* 2017, 121, 8746–8751.
8. Zhumekenov, A. A.; Saidaminov, M. I.; Haque, M. A.; Alarousu, E.; Sarmah, S. P.; Murali, B.; Dursun, I.; Miao, X.-H.; Abdelhady, A. L.; Wu, T.; et al. Formamidinium Lead Halide Perovskite Crystals with Unprecedented Long Carrier Dynamics and Diffusion Length. *ACS Energy Lett.* 2016, 1, 32–37.
9. Minh, D. N.; Kim, J.; Hyon, J.; Sim, J. H.; Sowlih, H. H.; Seo, C.; Nam, J.; Eom, S.; Suk, S.; Lee, S.; et al. Room-Temperature Synthesis of Widely Tunable Formamidinium Lead Halide Perovskite Nanocrystals. *Chem. Mater.* 2017, 29, 5713–5719.
10. Protesescu, L.; Yakunin, S.; Bodnarchuk, M. I.; Bertolotti, F.; Masciocchi, N.; Guagliardi, A.; Kovalenko, M. V. Monodisperse Formamidinium Lead Bromide

- Nanocrystals with Bright and Stable Green Photoluminescence. *J. Am. Chem. Soc.* 2016, 138, 14202–14205.
11. Amat, A.; Mosconi, E.; Ronca, E.; Quarti, C.; Umari, P.; Nazeeruddin, M. K.; Gratzel, M.; De Angelis, F. Cation-Induced Band-Gap Tuning in Organohalide Perovskites: Interplay of Spin-Orbit Coupling and Octahedra Tilting. *Nano Lett.* 2014, 14, 3608–3616.
 12. Ogomi, Y.; Morita, A.; Tsukamoto, S.; Saitho, T.; Fujikawa, N.; Shen, Q.; Toyoda, T.; Yoshino, K.; Pandey, S. S.; Ma, T.; et al. $\text{CH}_3\text{NH}_3\text{Sn}_x\text{Pb}_{(1-x)}\text{I}_3$ Perovskite Solar Cells Covering up to 1060 nm. *J. Phys. Chem. Lett.* 2014, 5, 1004–1011.
 13. Hao, F.; Stoumpos, C. C.; Chang, R. P. H.; Kanatzidis, M. G. Anomalous Band Gap Behavior in Mixed Sn and Pb Perovskites Enables Broadening of Absorption Spectrum in Solar Cells. *J. Am. Chem. Soc.* 2014, 136, 8094–8099.
 14. Mosconi, E.; Umari, P.; De Angelis, F. Electronic and Optical Properties of Mixed Sn-Pb Organohalide Perovskites: A First Principles Investigation. *J. Mater. Chem. A* 2015, 3, 9208–9215.
 15. Eperon, G. E.; Leijtens, T.; Bush, K. A.; Prasanna, R.; Green, T.; Wang, J. T.-W.; McMeekin, D. P.; Volonakis, G.; Milot, R. L.; May, R.; et al. Perovskite-Perovskite Tandem Photovoltaics with Optimized Band Gaps. *Science* 2016, 354, 861–865.
 16. Zhao, Z.; Gu, F.; Li, Y.; Sun, W.; Ye, S.; Rao, H.; Liu, Z.; Bian, Z.; Huang, C. Mixed-Organic-Cation Tin Iodide for Lead-Free Perovskite Solar Cells with an Efficiency of 8.12%. *Adv. Sci.* 2017, 4, 1700204.
 17. Abate, A. Perovskite Solar Cells Go Lead Free. *Joule* 2017, 1, 659–664.
 18. Mancini, A.; Quadrelli, P.; Milanese, C.; Patrini, M.; Guizzetti, G.; Malavasi, L. $\text{CH}_3\text{NH}_3\text{Sn}_x\text{Pb}_{1-x}\text{Br}_3$ Hybrid Perovskite Solid Solution: Synthesis, Structure, and Optical Properties. *Inorg. Chem.* 2015, 54, 8893–8895.
 19. Ferrara, C.; Patrini, M.; Pisanu, A.; Quadrelli, P.; Milanese, C.; Tealdi, C.; Malavasi, L. Wide Bandgap Tuning in Sn-based Hybrid Perovskites through Cation Replacement: the $\text{FA}_{1-x}\text{MA}_x\text{SnBr}_3$ Mixed System. *J. Mater. Chem. A* 2017, 5, 9391–9395.
 20. Borriello, I.; Cantele, G.; Ninno, D. Ab Initio Investigation of Hybrid Organic-Inorganic Perovskites Based on Tin Halides. *Phys. Rev. B: Condens. Matter Mater. Phys.* 2008, 77, 235214.
 21. Stoumpos, C. C.; Frazer, L.; Clark, D. J.; Kim, Y. S.; Rhim, S. H.; Freeman, A. J.; Ketterson, J. B.; Jang, J. I.; Kanatzidis, M. G. Hybrid Germanium Iodide Perovskite Semiconductors: Active Lone Pairs, Structural Distortions, Direct and

- Indirect Energy Gaps, and Strong Nonlinear Optical Properties. *J. Am. Chem. Soc.* 2015, 137, 6804–6819.
22. Mancini, A.; Quadrelli, P.; Milanese, C.; Patrini, M.; Guizzetti, G.; Malavasi, L. $\text{CH}_3\text{NH}_3\text{Sn}_x\text{Pb}_{1-x}\text{Br}_3$ Hybrid Perovskite Solid Solution: Synthesis, Structure, and Optical Properties. *Inorg. Chem.* 2015, 54, 8893-8895.
 23. Mancini, A.; Quadrelli, P.; Amoroso, G.; Milanese, C.; Boiocchi, M.; Sironi, A.; Patrini, M.; Guizzetti, G.; Malavasi, L. Synthesis, structural and optical characterization of APbX_3 (A=methylammonium, dimethylammonium, trimethylammonium; X=I, Br, Cl) hybrid organic inorganic materials. *J. Solid State Chem.* 2016, 240, 55-60.
 24. Schueller, E. C.; Laurita, G.; Fabini, D. H.; Stoumpos, C. C.; Kanatzidis, M. G.; Seshadri, R. Crystal Structure Evolution and Notable Thermal Expansion in Hybrid Perovskites Formamidinium Tin Iodide and Formamidinium Lead Bromide. *Inorg. Chem.* 2018, 57, 695–701.
 25. Sabba, D.; Mulmudi, H. K.; Prabhakar, R. R.; Krishnamoorthy, T.; Baikie, T.; Boix, P. P.; Mhaisalkar, S.; Mathews, N. Impact of Anionic Br^- Substitution on Open Circuit Voltage in Lead Free Perovskite ($\text{CsSnI}_{3-x}\text{Br}_x$) Solar Cells. *J. Phys. Chem. C* 2015, 119, 1763–1767.
 26. Becker, M.; Kluner, T.; Wark, M. Formation of Hybrid ABX_3 Perovskite Compounds for Solar Cell Application: First-Principles Calculations of Effective Ionic Radii and Determination of Tolerance Factors. *Dalton Trans.* 2017, 46, 3500–3509.
 27. Kubelka, P.; Munk, F. Ein Beitrag zur Optik der Farbanstriche. *Z. Tech. Phys.* 1931, 12, 593–601.
 28. Kim, H.-S.; Lee, C.-R.; Im, J.-H.; Lee, K.-B.; Moehl, T.; Marchioro, A.; Moon, S.-J.; Humphry-Baker, R.; Yum, J.-H.; Moser, J. E.; et al. Lead Iodide Perovskite Sensitized All-Solid-State Submicron Thin Film Mesoscopic Solar Cell with Efficiency Exceeding 9%. *Sci. Rep.* 2012, 2, 591.
 29. Konstantakou, M.; Stergiopoulos, T. A Critical Review on Tin Halide Perovskite Solar Cells. *J. Mater. Chem. A* 2017, 5, 11518–11549.
 30. Perdew, J. P.; Burke, K.; Ernzerhof, M. Generalized Gradient Approximation Made Simple. *Phys. Rev. Lett.* 1996, 77, 3865–3868.
 31. Heyd, J.; Scuseria, G. E.; Ernzerhof, M. Hybrid Functionals Based on a Screened Coulomb Potential. *J. Chem. Phys.* 2003, 118, 8207–8215.

32. Du, M.-H. Density Functional Calculations of Native Defects in CH₃NH₃PbI₃: Effects of Spin–Orbit Coupling and Self-Interaction Error. *J. Phys. Chem. Lett.* 2015, 6, 1461–1466.
33. Umari, P.; Mosconi, E.; De Angelis, F. Relativistic GW Calculations on CH₃NH₃PbI₃ and CH₃NH₃SnI₃ Perovskites for Solar Cell Applications. *Sci. Rep.* 2015, 4, 4467.
34. Kieslich, G.; Sun, S.; Cheetham, A. K. Solid-State Principles Applied to Organic-Inorganic Perovskites: New Tricks for an Old Dog. *Chem. Sci.* 2014, 5, 4712–4715.
35. Travis, W.; Glover, E. N. K.; Bronstein, H.; Scanlon, D. O.; Palgrave, R. G. On the Application of the Tolerance Factor to Inorganic and Hybrid Halide Perovskites: A Revised System. *Chem. Sci.* 2016, 7, 4548–4556.
36. Gholipour, S.; Ali, A. M.; Correa-Baena, J.-P.; Turren-Cruz, S.- H.; Tajabadi, F.; Tress, W.; Taghavinia, N.; Gratzel, M.; Abate, A.; De Angelis, F.; et al. Globularity-Selected Large Molecules for a New Generation of Multication Perovskites. *Adv. Mater.* 2017, 29, 1702005.
37. Gupta, S.; Bendikov, T.; Hodes, G.; Cahen, D. CsSnBr₃, A Lead-Free Halide Perovskite for Long-Term Solar Cell Application: Insights on SnF₂ Addition. *ACS Energy Lett.* 2016, 1, 1028–1033.
38. Stoumpos, C. C.; Malliakas, C. D.; Kanatzidis, M. G. Semiconducting Tin and Lead Iodide Perovskites with Organic Cations: Phase Transitions, High Mobilities, and Near-Infrared Photoluminescent Properties. *Inorg. Chem.* 2013, 52, 9019–9038.
39. Quarti, C.; Mosconi, E.; Ball, J. M.; D’Innocenzo, V.; Tao, C.; Pathak, S.; Snaith, H. J.; Petrozza, A.; De Angelis, F. Structural and Optical Properties of Methylammonium Lead Iodide across the Tetragonal to Cubic Phase Transition: Implications for Perovskite Solar Cells. *Energy Environ. Sci.* 2016, 9, 155–163.
40. Car, R.; Parrinello, M. Unified Approach for Molecular Dynamics and Density-Functional Theory. *Phys. Rev. Lett.* 1985, 55, 2471–2474.
41. Giannozzi, P.; De Angelis, F.; Car, R. First-Principle Molecular Dynamics with Ultra soft Pseudopotentials: Parallel Implementation and Application to Extended Bioinorganic Systems. *J. Chem. Phys.* 2004, 120, 5903–5915.

CHAPTER 4:

MIXED A-CATION TIN-BASED PEROVSKITES

As reported in the second chapter, modulation of HPs properties by means of protonated amine substitution is a fascinating and powerful route explored since the discovery of these new photovoltaic materials. But, as it was shown in the previous chapter, it is also important to consider the Sn replacement for Pb in order to exploit the use of environmentally friendly hybrid perovskites. Tin-based perovskites have the advantages of smaller optical bandgaps and greater charge mobility than their lead-based perovskites counterpart, but their applications are limited because of the chemical instability under ambient condition, related to the tin oxidation state. Sn^{4+} acts as a p-dopant within the perovskite in a process so called *self-doping* and increases the concentrations of holes that could lead to severe recombination of charge carriers in these solar cells. Our group already showed that reliable structural and optical performances require a strict control over this parameter. (64) (65)

Early tests of MASnI_3 yielded device performance with PCE 5–6%, but the devices were unstable and lacked reproducibility due to oxidation of Sn^{2+} . To suppress that oxidation, one solution could be changing the electronic structure of perovskite. Since 2014, some important progress has been made in this field. For example, SnF_2 , as an additive, has been found to effectively suppress the doped hole density in Sn-based perovskites and improve device stability and reproducibility. The use of dimethyl sulfoxide (DMSO) as the precursor solvent has proven to be crucial in acquiring homogeneous films, as it forms a $\text{SnI}_2 \cdot 3\text{DMSO}$ intermediate phase that retards the rapid crystallization of Sn-based perovskites. Wang et al (66) investigated the role of organic cations comparing MA and FA, demonstrating that it strongly influences the oxidation of Sn and the binding of H_2O molecules to the lattice and concluding that their study suggests that stable Sn-based perovskite devices may be realized by making a proper selection of the organic cation. However, in the actual literature there are few reports about mixed A-cation compositions of tin perovskites as it has been extensively reported for Pb-based materials. In this chapter I will focus on this topic.

4.1 FA_(1-x)MA_xSnBr₃

Wide bandgap tuning in Sn-based hybrid perovskites through cation replacement: the FA_{1-x}MA_xSnBr₃ mixed system

Purpose and scope

To the best of my knowledge, when I published this first article about the mixed A cation Sn-based system, there were not report about composition engineering of pure Sn-based perovskites.

Our group investigated the synthesis, crystal structure and optical properties of the reported system with a special emphasis in defining the FA/MA ratio by means of Solid-State NMR. The results indicate the formation of a continuous solid solution between the two end members with a terrific modulation of the band gap, results which suggest the key role of protonated amines in the electronic structure of tin based systems.

This unprecedented wide tuning of the optical properties by cation replacement is impossible to reach using inorganic cation as proved in this recent article (67) of our group about the Cs_{1-x}Rb_xSnBr₃ system, where the band gap varies from 1.719 to 1.817 eV from CsSnBr₃ to Cs_{0.70}Rb_{0.30}SnBr₃ sample.

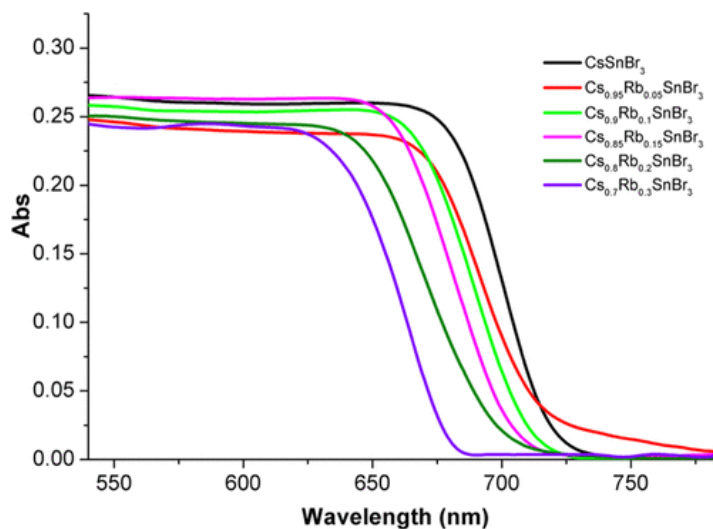


Figure 4.1: Total absorption spectra of Cs_{1-x}Rb_xSnBr₃ samples with 0 ≤ x ≤ 0.3

Experimental section

Samples of the general formula $\text{FA}_{1-x}\text{MA}_x\text{SnBr}_3$ (with nominal $x = 0, 0.05, 0.2, 0.3, 0.6, 0.8$ and 1) were synthesized according to a general and original procedure we developed.^{8,9} In a typical synthesis, a proper stoichiometric amount of Sn acetate is dissolved in an HBr excess under continuous mechanical stirring under a nitrogen atmosphere. Hypophosphoric acid is added to the solution and an inert atmosphere is maintained in the reaction environment in order to prevent Sn oxidation. Subsequently, the solution is heated to $100\text{ }^\circ\text{C}$ and the corresponding amine solutions (40% wt in water) are added in the stoichiometric amount to achieve the desired FA : MA ratio. The as obtained final solution is then cooled down to $46\text{ }^\circ\text{C}$ at $1\text{ }^\circ\text{C min}^{-1}$, until the formation of a precipitate that is immediately filtered and dried under vacuum overnight. All the reagents were purchased from Sigma Aldrich in pure form and were used without any further purification. The final products are handled and stored in a glove box with oxygen and water contents lower than 1 ppm. The crystal structure of the samples has been characterized at room temperature. Cu-radiation laboratory X-ray powder diffraction (XRD) data were acquired with a Bruker D5005 diffractometer by using a Bruker dome sealed in the glove box avoiding air exposure. High-resolution synchrotron data for FASnBr_3 have been collected on ID22 (ESRF) in transmission mode with $\lambda=0.176\text{ \AA}$ with the sample filled into a quartz capillary. Diffraction data have been refined according to the Rietveld method to derive cell parameters and the volume with the use of FullProf package.²⁵ The optical diffuse reflectance spectra of the different perovskites were measured from 0.8 to 4.5 eV (250–1500 nm, with steps of 1 nm) with a Varian Cary 6000i instrument equipped with an integrating sphere. For this kind of measurement, polycrystalline powders were loaded in 1 mm optical path cuvettes made of special optical glass (Hellma). ^1H solid-state NMR room temperature measurements have been performed on a 9.4 T ($^1\text{H} = 400.16\text{ MHz}$) Bruker Advance III with the use of TopSpin 3.1 software; spectra have been collected with a 4 mm MAS probe under 8 kHz spinning conditions. ^1H quantitative one-pulse experiments have been conducted with a pulse length of 4.65 ms, recycle delay of 120 s and 16 scans. Pulse lengths and recycle delay have been carefully calibrated before the acquisition of the final spectra to ensure the full relaxation of the magnetization and fulfill the conditions for the quantitative data acquisition. Chemical shifts are referred to TMS using adamantane as a secondary standard. The analysis of the obtained data has been performed with the use of DMFit program.²⁶ All the manipulations and measurements of the samples have been carried out under inert conditions in order to avoid tin oxidation.

Results and discussion

As mentioned above, in order to provide the most reliable and accurate correlation between physical properties and composition, the prepared samples have been investigated by solid-state ^1H NMR spectroscopy in order to determine their real FA : MA content. Such an approach has already been shown to be effective in estimating the A-site composition.²⁷ ^1H MAS spectra of the whole $\text{FA}_{1-x}\text{MA}_x\text{SnBr}_3$ series, together with the corresponding attribution and the best fit for the two end members, are reported in Figure 4.2.

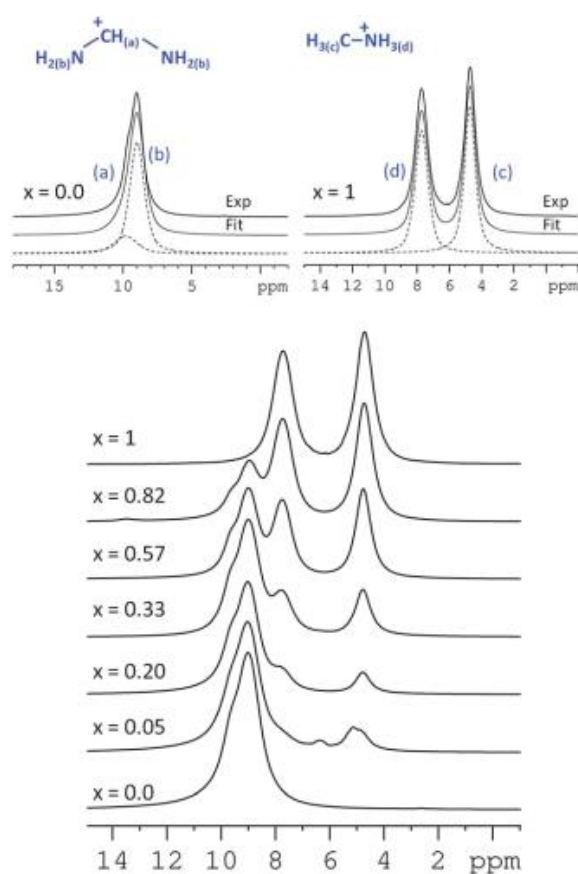


Figure 4.2: Solid-state NMR spectra of the $\text{FA}_{1-x}\text{MA}_x\text{SnBr}_3$ solid solution. The top panel shows the NMR spectra of FASnBr_3 (left) and MASnBr_3 (right) where dashed lines represent fit contributions and the solid light line represents the overall best-fit to the experiment spectra

The quantitative spectrum of the FASnBr_3 composition presents two peaks at 9.81 ppm and 9.02 ppm with a relative ratio of 4 : 1 and these signals can be attributed to the $-\text{NH}_2$ and $-\text{CH}$ protons, respectively. Similar chemical shifts have been observed for the NMR signal (liquid) of the $\text{HC}(\text{NH}_2)_2\text{I}$ and FAI precursors used for the synthesis of FAPI .^{28,29} Similarly, the attribution for the MASnBr_3 composition has been made considering the presence of the two resonances at 7.73 and 4.72 ppm with a $\approx 1 : 1$ ratio. These two signals have been previously correlated, respectively, to the $-\text{NH}_3^+$ and $-\text{CH}_3^+$ protons of the methylammonium group for the series MAPbX_3 ($\text{X} = \text{I}, \text{Br},$ and Cl).³⁰ The signals of the two MA and FA species are only partially overlapped and under the experimental MAS speed (8 kHz) the observed lines are sufficiently sharp. The acquisition parameters (pulse

length and recovery delay) have been optimized to obtain fully relaxed signals and allow for the quantitative analysis of the data. Each spectrum has been fitted considering four peaks; during the fitting procedure no constraints were imposed on the peak position, intensity and width that were allowed to vary. The stoichiometry derived from best fit

results is reported in Figure 4.2 for each spectrum. It must be stressed that the internal ratio of the integrals for the MA and FA groups were well reproduced and maintained during the fitting, despite the absence of imposed constraints on the intensity and linewidth. The ratio of peak integrals of the characteristic MA and FA cation resonances

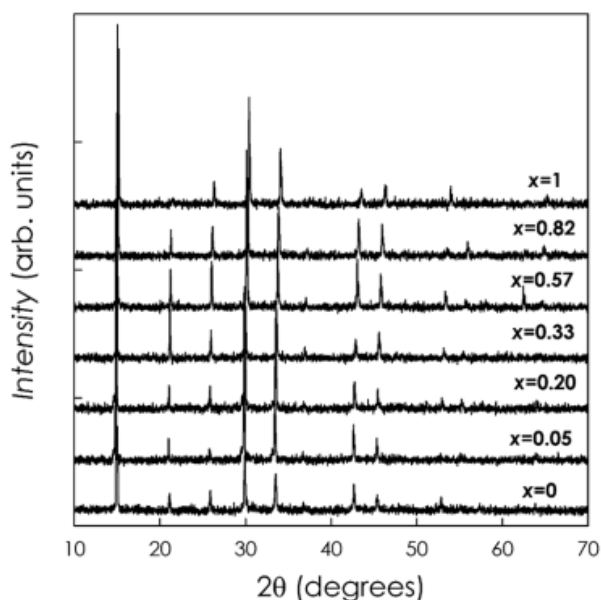


Figure 4.3: XRD patterns for the samples of the $FA_{1-x}MA_xSnBr_3$ system. The patterns are vertically shifted to clarify viewing

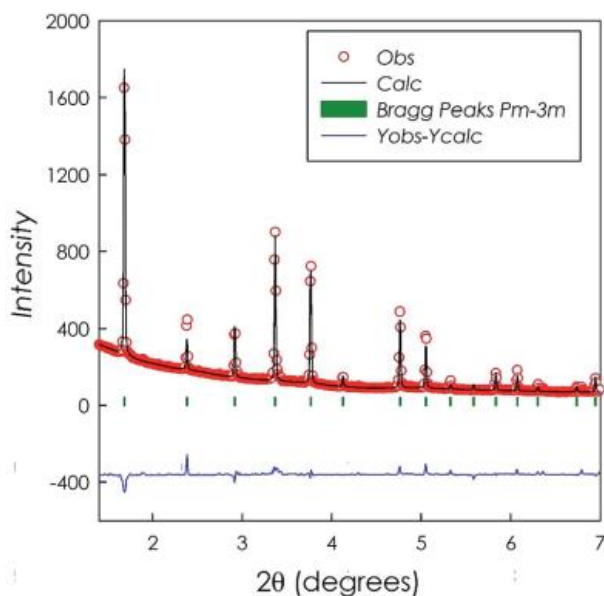


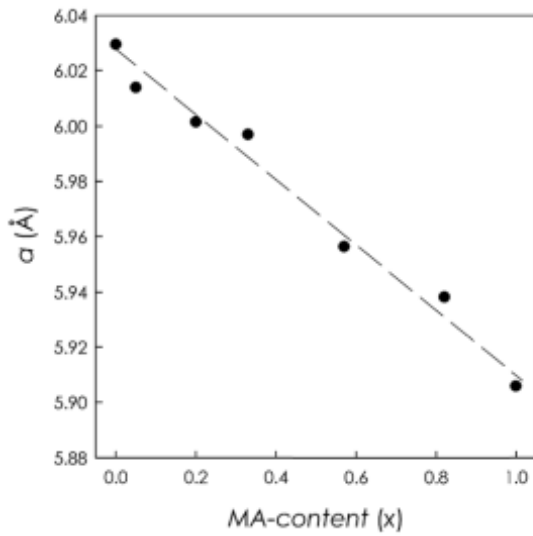
Figure 4.4: Rietveld refinement of synchrotron data ($\lambda=0.176\text{\AA}$) for $FASnBr_3$

was calculated for each spectrum to determine the stoichiometry of the compound. It was found that the actual FA : MA stoichiometries, determined by NMR, were in good agreement with the nominal compositions (*i.e.*, those used in the preparation of the samples) within an estimated standard deviation of about 5%. From this point on, we will refer to the sample by quoting the “real” stoichiometries found with NMR measurements.

The prepared samples have been characterized by means of laboratory X-ray diffraction (XRD). Figure 4.3 reports the patterns of the $FA_{1-x}MA_xSnBr_3$ series in the 10–70 range. The crystal structure of $MASnBr_3$ has been the object of detailed structural analysis and has been indexed with a cubic lattice (space group $Pm\bar{3}m$).³¹ On the other hand, $FASnBr_3$ has never been reported in the current literature. From the comparison of the laboratory XRD patterns reported in Figure 4.3, we could observe that all the samples of the $FA_{1-x}MA_xSnBr_3$ system present analogous reflections in the diffraction patterns, which are also free from detectable impurities.

For the FASnBr_3 sample, due to the lack of previous structural studies, we collected a high-resolution synchrotron diffraction pattern ($\lambda=0.176 \text{ \AA}$). The Rietveld refinement of this pattern using, as starting model, the cubic $\text{Pm}\bar{3}\text{m}$ symmetry as for MASnBr_3 , is reported in Figure 4.4.

The good agreement of the refinement ($R_{\text{wp}}=7.94$, $\chi^2=1.65$) suggests that the cubic lattice of MASnBr_3 is retained along with the MA/FA substitution on the perovskite A-lattice for the whole x -range. The trend of the cubic lattice parameter, a , as a function of x , determined from the patterns of the $\text{FA}_{1-x}\text{MA}_x\text{SnBr}_3$ system shown in Figure 4.4, is



reported in Fig. 4.5. As can be apprehended from this figure, a linear decrease of the cubic a lattice parameter is found along with the increase of the amount of the smaller MA cation in the system ($\text{MA } r_{\text{eff}} = 217 \text{ pm}$ and $\text{FA } r_{\text{eff}} = 253 \text{ pm}$).⁶ This behaviour is consistent with Vegard's law of solid solution formation, along with the same symmetry for the two end-members of the series (*i.e.*, FASnBr_3 and MASnBr_3), and indicates the formation of a continuous solid solution in the $\text{FA}_{1-x}\text{MA}_x\text{SnBr}_3$ system, in analogy with the previous observation on $\text{FA}_{1-x}\text{MA}_x\text{SnBr}_3$.⁶

Figure 4.5: (a) Cubic lattice parameters and (b) cell volume of the $\text{FA}_{1-x}\text{MA}_x\text{SnBr}_3$ system as a function of x

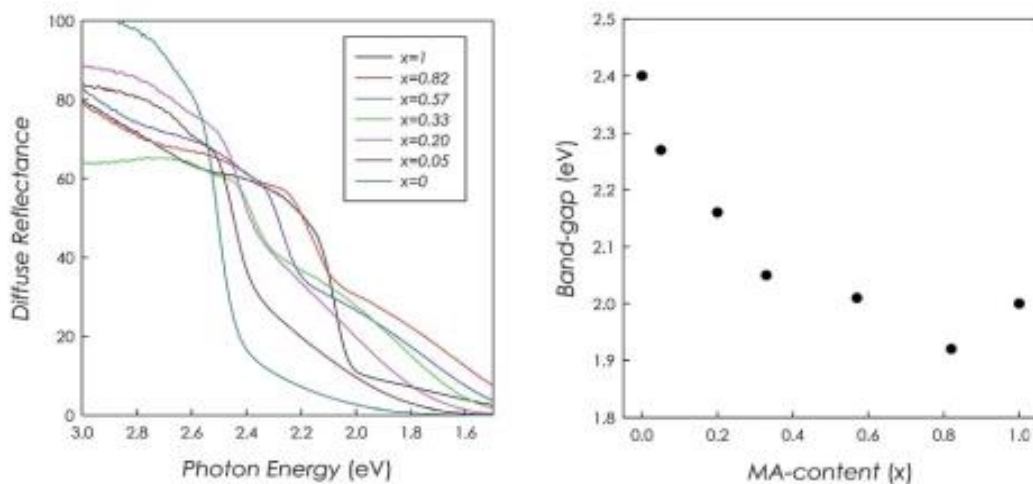


Figure 4.6: (a) Diffuse reflectance spectra of the $\text{FA}_{1-x}\text{MA}_x\text{SnBr}_3$ solid solution; (b) energy gap trend as a function of

x

As a matter of fact, the structural results reported here are the first evidence of the existence of a solid solution in a tin-based hybrid perovskite. The search for solid solution in this class of materials is of significant importance since the modulation of x may allow a corresponding optical property modulation.

Optical measurements have been carried out on the $\text{FA}_{1-x}\text{MA}_x\text{SnBr}_3$ samples in order to define the band-gap values as a function of cation stoichiometry. Figures 4.6a and 4.6b report the vis-NIR diffuse reflectance spectra (R) and the trend of band-gap energy as a function of x , respectively. The E_g values have been obtained from the extrapolation of the linear part of $[F(R)hv]^2$ where $F(R)$ is the Kubelka–Munk function $F(R) = (1 - R)^2/2R$.^{32,33}

From Figure 4.6 it is possible to observe a progressive decrease of the band gap by increasing x up to 0.82, where an upturn is observed for MASnBr_3 . The E_g value of FASnBr_3 has not yet been measured in the current literature, but only theoretically estimated to be around 2.58 eV.³⁴ The present experimental value of ca. 2.40 eV is fairly in good agreement with the value calculated from the GW-BSE theory (the Bethe–Salpeter equation).³⁴ The band-gap value for the other end-member of the solid solution, namely MASnBr_3 , has been reported to be around 2.15 eV, which is in good agreement with the present value of about 2.0 eV. The small discrepancy between the two E_g values is probably due to the nature of the samples (films in ref. 33 and powders in the present paper) and to the measurement method.³⁵

Starting from FASnBr_3 , the band-gap value progressively reduces from 2.4 eV ($x = 0$) down to ~1.92 eV ($x = 0.82$), *i.e.* of about 0.5 eV, which is a huge energy variation for a cation replacement. Such high values are usually observed for B-cation or X-anion replacements.^{3,9,36–40} This trend is in contrast with other FA/MA mixed systems, such as the $\text{FA}_{1-x}\text{MA}_x\text{SnBr}_3$ solid solution, where a progressive increase of the band gap is observed by decreasing the FA content.⁶ Moreover, the complete FA/MA replacement in $\text{FA}_{1-x}\text{MA}_x\text{SnBr}_3$ leads to an overall shift in the band gap of less than 0.1 eV across the whole composition range (*i.e.*, $0 \leq x \leq 1$). These results are quite surprising considering that the contribution of the A site cation to the density of states close to valence or conduction band edges is usually expected to be negligible, and thus the effect of cation replacement on the energy gap is indirect and related to the variation of the lattice size.⁶

However, the experimental results reported here for the $\text{FA}_{1-x}\text{MA}_x\text{SnBr}_3$ solid solution, clearly show a very wide tuning of the band gap induced by the FA/MA substitution suggesting a contribution of the A-site cation to the joint density of states in this system. As a matter of fact, our evidence is in very good agreement with recent theoretical calculations showing that, for cubic Sn-based hybrid perovskites, the p-

electrons of N and C atoms partially contribute to the valence band top.⁴¹ In particular, for FASnX_3 perovskites the p-electrons of both N and C atoms give a contribution to the VBT (Valence Band Top) while for MASnX_3 systems only the p-states of N atoms partially contribute to the VBT.

With these theoretical arguments, the strong variation of the band gap from FASnBr_3 up to $x = 0.82$ in the mixed $\text{FA}_{1-x}\text{MA}_x\text{SnBr}_3$ system may result by the interplay of the N and C p states contributing to the DOS and a lattice effect induced by the size difference between the two cations. When reaching the pure MASnBr_3 system, we are facing a different situation where C electronic states no longer affect the electronic structure and, looking from this side of the solid solution, already a small amount of the FA cation (*i.e.*, 0.18) effectively reduces the band gap of about 0.081 eV. The experimental results reported in this work, showing an impressive modulation of the band gap as a function of A-site cation replacement, merit to be further investigated from a theoretical point of view, in particular considering the role of mixed FA/MA composition in tin-based halides.

Conclusions

In the present paper have been investigated the synthesis, crystal structure and optical properties of the $\text{FA}_{1-x}\text{MA}_x\text{SnBr}_3$ system, with particular care in defining the FA/MA stoichiometries by means of NMR and reporting for the first time the FASnBr_3 material. The results confirm the formation of a solid solution between the two end members, which possess a cubic symmetry with lattice parameter and cell volume obeying Vegard's law. The investigation of the optical properties revealed an impressive and unexpected variation of the band gap induced by the FA/MA substitution, which leads to a wide tuning of the E_g in the $\text{FA}_{1-x}\text{MA}_x\text{SnBr}_3$ system from 2.4 to 1.9 eV just by adjusting the ratio of the protonated amines. One possible origin of this new phenomenon in hybrid perovskites is the contribution of MA and/or FA to the density of states and in turn to the valence band characteristics, as indicated by theoretical calculations. If further confirmed by additional electronic structure modelling works, the $\text{FA}_{1-x}\text{MA}_x\text{SnBr}_3$ solid solution would represent the first example of an organic–inorganic hybrid perovskite system where the A-site cation has a profound impact on the electronic structure and allows an unprecedented wide tuning of optical properties by cation replacement.

References

1. J. Jeon, J. H. Noh, W. S. Yang, Y. Kim, S. Ryu, J. Seo and S. Seok, *Nature*, 2015, 517, 476.
2. N. Pellet, P. Gao, G. Gregori, T.-Y. Yang, M. Nazeeruddin and J. Maier, *Angew. Chem., Int. Ed.*, 2014, 53, 3151.
3. T. J. Jacobsson, J.-P. Correa-Baena, M. Pazoki, M. Saliba, K. Schenk, M. Graetzel and A. Hagfeldt, *Energy Environ. Sci.*, 2016, 9, 1706.
4. W. S. Yang, J. H. Noh, N. J. Jeon, Y. C. Kim, S. Ryu, J. Seo and S. Seok, *Science*, 2015, 348, 1234.
5. Z. Yang, C.-C. Chueh, P.-W. Liang, M. Crump, F. Lin, Z. Zhu and A. K.-Y. Jen, *Nano Energy*, 2016, 22, 328.
6. O. J. Weber, B. Charles and M. T. Weller, *J. Mater. Chem. A*, 2016, 4, 15375.
7. A. Mancini, P. Quadrelli, G. Amoroso, C. Milanese, M. Boiocchi, A. Sironi, M. Patrini, G. Guizzetti and L. Malavasi, *J. Solid State Chem.*, 2016, 240, 55.
8. M. Patrini, P. Quadrelli, C. Milanese and L. Malavasi, *Inorg. Chem.*, 2016, 55, 12752.
9. A. Mancini, P. Quadrelli, C. Milanese, M. Patrini, G. Guizzetti and L. Malavasi, *Inorg. Chem.*, 2015, 54, 8893.
10. F. Hao, C. C. Stoumpos, R. P. H. Chang and M. G. Kanatzidis, *J. Am. Chem. Soc.*, 2014, 136, 8094.
11. C. C. Stoumpos, C. D. Malliakas and M. G. Kanatzidis, *Inorg. Chem.*, 2013, 52, 9019.
12. T. M. Koh, T. Krishnamoorthy, N. Yantara, C. Shi, W. L. Leong, P. P. Boix, A. C. Grimsdale, S. G. Mhaisalkar and N. Mathews, *J. Mater. Chem. A*, 2015, 3, 14996.
13. M.-C. I. Jung, S. R. Raga and Y. Qi, *RSC Adv.*, 2016, 6, 2819.
14. I. Borriello, G. Cantele and D. Ninno, *Phys. Rev. B: Condens. Matter Mater. Phys.*, 2008, 77, 235214.
15. E. Mosconi, P. Umari and F. de Angelis, *J. Mater. Chem. A*, 2015, 3, 9208.
16. T.-B. Song, T. Yokoyama, C. C. Stoumpos, J. Logsdon, D. H. Cao, M. R. Wasielewski, S. Aramaki and M. G. Kanatzidis, *J. Am. Chem. Soc.*, 2017, 139, 836.
17. L. Ma, F. Hao, C. C. Stoumpos, B. T. Phelan, M. R. Wasielewski and M. G. Kanatzidis, *J. Am. Chem. Soc.*, 2016, 138, 14750.
18. W. Liao, D. Zhao, Y. Yu, N. Shrestha, K. Ghimire, C. R. Grice, C. Wang, Y. Xiao, A. J. Cimaroli, R. J. Ellingson, N. J. Podraza, K. Zhu, R.-G. Xiong and Y. Yan, *J. Am. Chem. Soc.*, 2016, 138, 12360.

19. F. Hao, C. C. Stoumpos, D. H. Cao, R. P. H. Chang and M. G. Kanatzidis, *Nat. Photonics*, 2014, 8, 489.
20. N. K. Noel, S. D. Stranks, A. Abate, C. Wehrenfennig, S. Guarnera, A.-A. Haghighirad, A. Sadhanala, G. E. Eperon, S. K. Pathak, M. B. Johnston, A. Petrozza, L. M. Herz and H. J. Snaith, *Energy Environ. Sci.*, 2014, 7, 3061.
21. M.-C. Jung, S. R. Raga and Y. Qi, *RSC Adv.*, 2016, 6, 2819.
22. T. Yokoyama, T.-B. Song, D. H. Cao, C. C. Stoumpos, S. Aramaki and M. G. Kanatzidis, *ACS Energy Lett.*, 2017, 2, 22.
23. S. J. Lee, S. S. Shin, Y. C. Kim, D. Kim, T. K. Ahn, J. H. Noh, J. Seo and S. Il Seok, *J. Am. Chem. Soc.*, 2016, 138, 3974.
24. W. Liao, D. Zhao, Y. Yu, C. R. Grice, C. Wang, A. J. Cimaroli, P. Schulz, W. Meng, K. Zhu, R.-G. Xiong and Y. Yan, *Adv. Mater.*, 2016, 9, 9333.
25. J. Rodr'iguez-Carvajal, *J. Phys.: Condens. Matter*, 1993, 192, 55.
26. D. Massiot, F. Fayon, M. Capron, I. King, S. Le Calve, B. Alonso, J. O. Durand, B. Bujoli, Z. Gan and G. Hoatson, *Magn. Reson. Chem.*, 2002, 40, 70.
27. O. J. Weber, B. Charles and M. T. Weller, *J. Mater. Chem. A*, 2016, 4, 15375.
28. J.-W. Lee, D.-J. Seol, A.-N. Cho and N.-G. Park, *Adv. Mater.*, 2014, 26, 4991.
29. Y. Fu, H. Zhu, A. W. Schrader, D. Liang, Q. Ding, P. Joshi, L. Hwang and X.-Y. Zhu, *Nano Lett.*, 2016, 16, 1000.
30. T. Baikie, N. S. Barrow, Y. Fang, P. J. Keenan, P. R. Slater, R. O. Piltz, M. Gutmann, S. G. Mhaisalkar and T. J. A. White, *J. Mater. Chem. A*, 2015, 3, 9298.
31. I. Swainson, L. Chi, J. H. Her, L. Cranswick, P. Stephens, B. Winkler, D. J. Wilson and V. Milman, *Acta Crystallogr., Sect. B: Struct. Crystallogr. Cryst. Chem.*, 2010, 66, 422.
32. P. Kubelka and F. Munk, *Zeit. Fur Techn. Physik*, 1931, 12, 593.
33. H.-S. Kim, C. R. Lee, J.-H. Im, K.-B. Lee, T. Moehl, A. Marchioro, S.-J. Moon, R. Humphry-Baker, J.-H. Yum, J. E. Moser, M. Graetzel and N.-G. Park, *Sci. Rep.*, 2012, 2, 591.
34. M. Bokdam, T. Sander, A. Stroppa, S. Picozzi, D. D. Sarma, C. Franchini and G. Kresse, *Sci. Rep.*, 2016, 6, 28618.
35. F. Hao, C. C. Stoumpos, D. H. Cao, R. P. Chang and M. G. Kanatzidis, *Nat. Photonics*, 2014, 8, 489.
36. F. Brivio, K. T. Butler, A. Walsh and M. Van Schilfgaarde, *Phys. Rev. B: Condens. Matter Mater. Phys.*, 2014, 89, 155204.
37. I. Borriello, G. Cantele and D. Ninno, *Phys. Rev. B: Condens. Matter Mater. Phys.*, 2008, 77, 235214.

38. T. Umebayashi, K. Asai, T. Kondo and A. Nakao, *Phys. Rev. B: Condens. Matter Mater. Phys.*, 2003, 67, 155405.
39. H.-Y. Ye, W.-Q. Liao, C.-L. Hu, Y. Zhang, Y.-M. You, J.-G. Mao, P.-F. Li and R.-G. Xiong, *Adv. Mater.*, 2016, 13, 2579.
40. W.-Q. Liao, Y. Zhang, C.-L. Hu, J.-G. Mao, H.-Y. Ye, P.-F. Li, S. D. Huang and R.-G. Xiong, *Nat. Commun.*, 2015, 6, 7338.
41. Z.-Q. Ma, H. Pan and P. K. Wong, *J. Electron. Mater.*, 2016, 45, 5956.

4.2 MA_(1-x)DMA_xSnBr₃

Enhanced air-stability of Sn-based hybrid perovskites induced by dimethylammonium (DMA): synthesis, characterization, aging and hydrogen photogeneration of the MA_{1-x}DMA_xSnBr₃ system

Purpose and Scope

Based on the experience gained in the study of the mixed-system MA_{1-x}DMA_xPbBr₃ (68) and mindful about the complete lack of experimental studies on the incorporation of this cation into Sn-based materials, during my last year of PhD we decided to work on the same mixed system but based on Sn. Here we show that methylammonium tin bromide can have up to 60% dimethylammonium incorporated in the crystal structure, even though this ion is often considered too large to fit in the cubic structure. The progressive alloying on the A-site results in a linear blue-shift of the absorption edge with the DMA content, mixed phase samples maintain the cubic crystal structure of parent MASnBr₃ with a quasi-linear expansion of the cell volume as the DMA content increases.

We performed aging test, coupling them with X-ray photoelectron spectroscopy, to prove the DMA_xSnBr₃ high tolerance against air-exposure in terms of both crystal structure and optical properties. This solid solution represents one of the first example of highly stable Sn(II)-containing hybrid perovskite.

Evidence of air-stable Sn(II)-containing perovskites represent a significant further step in the development of tin-containing photovoltaic devices. Driven by the improved stability of DMA_xSnBr₃ we also performed a test by immersing the material into deionized water (DI), which not only does not dissolve, but once dried, the pristine phase is formed.

Ahead of that, we decided to test DMA_xSnBr₃ as a possible photo-catalyst for hydrogen production evidencing quite low performance with respect to the most active photocatalysts, but even so it is an encouraging result which may further provoke a rich experimental research by designing nanocrystals.

Results and Discussion

Bulk powder samples of the $MA_{1-x}DMA_xSnBr_3$ system in the whole compositional range have been synthesized according to the synthetic procedure reported in the Experimental section. The appearance of some of the samples of the above-mentioned series are shown in Figure 4.7.

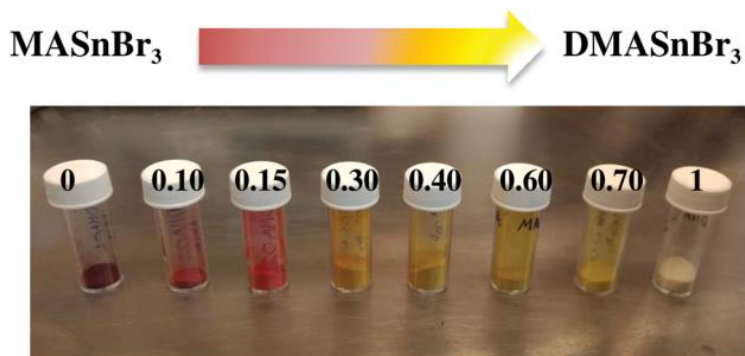


Figure 4.7: Appearance of bulk samples of the $MA_{1-x}DMA_xSnBr_3$ system from pure $MASnBr_3$ ($x=0$, left) to pure $DMASnBr_3$ ($x=1$, right)

From Figure 4.7, it is possible to observe a clear and progressive color change of the samples from intense purple for pure $MASnBr_3$ to off-white for pure $DMASnBr_3$ suggesting a relevant impact of alloying in this system. The laboratory Cu-K α X-ray diffraction patterns of all the synthesized samples are shown in Figure 4.8, with increasing DMA content from the bottom to the top of the figure.

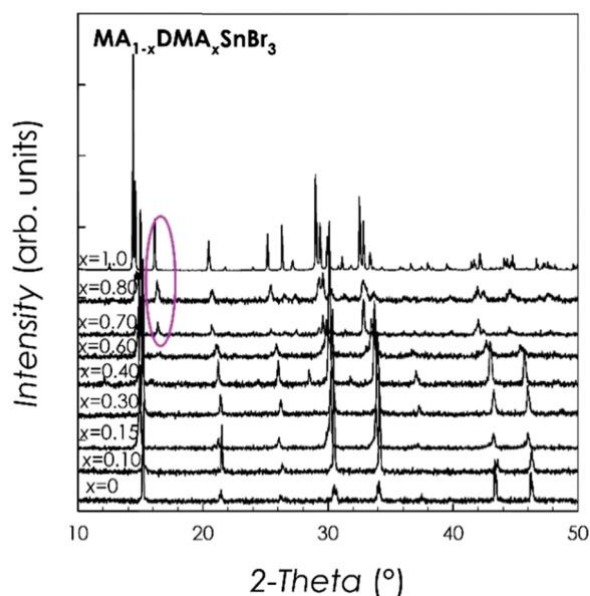


Figure 4.8: X-ray diffraction patterns of the $MA_{1-x}DMA_xSnBr_3$ samples

The starting $MASnBr_3$ sample has a cubic symmetry ($Pm\bar{3}m$ space group) and a lattice parameter of $5.9121(6)$ Å, in agreement with our previous investigation on the

FA_{1-x}MA_xSnBr₃ solid solution.⁷ By introducing DMA into the MASnBr₃ lattice, the samples retain a cubic unit cell up to $x = 0.60$. Above this composition, further MA/DMA alloying leads to the appearance of additional peaks in the pattern with the most intense one located around $2\theta = 161$ and highlighted with a pink circle in Fig. 4.8.

The new peaks appearing in the diffraction patterns of $x = 0.70$ and $x = 0.80$ samples correspond to peaks found in the orthorhombic structure of DMASnBr₃ ($x = 1.0$ in Fig. 4.8).¹⁹ As a matter of fact, $x = 0.70$ and $x = 0.80$ samples are not single-phase but a mixture of cubic and orthorhombic phases with the main orthorhombic one having the same lattice parameters of pure DMASnBr₃. The results of the optical measurements (see later in the text) support the existence of a two-phase system for $x = 0.70$ and $x = 0.80$. For this reason, these two-phase samples have been discarded from further analysis and discussion. Figure 4.9 shows the trend of lattice volume (normalized for the number of unit formula) of single-phase samples shown in Fig. 4.7, obtained by means of Rietveld refinement of the diffraction patterns, while the unit cell data are tabulated in Table 4.1. A progressive increase of the unit cell is found in the $0 \leq x \leq 0.60$ range, where the samples are cubic, and this trend fits well with the size of the orthorhombic unit cell of DMASnBr₃ ($x = 1$) being one of the two endmembers of the solid solution. The data reported suggest that the solid-solubility in the MA_{1-x}DMA_xSnBr₃ system is found up to about $x = 0.60$ which is larger than the solubility in the Pb-based analogous system.¹⁷

Table 4.1: Lattice parameter and band gap values

x	a (Å)	b (Å)	c (Å)	E_g (eV)
0	5.9129(5)	5.9129(5)	5.9129(5)	2.05
0.10	5.9198(5)	5.9198(5)	5.9198(5)	2.11
0.15	5.9210(6)	5.9210(6)	5.9210(6)	2.14
0.30	5.9543(3)	5.9543(3)	5.9543(3)	2.33
0.40	5.9700(4)	5.9700(4)	5.9700(4)	2.44
0.60	6.0110(8)	6.0110(8)	6.0110(8)	2.56
1.0	12.3216(4)	12.1812(3)	12.3265(3)	2.88

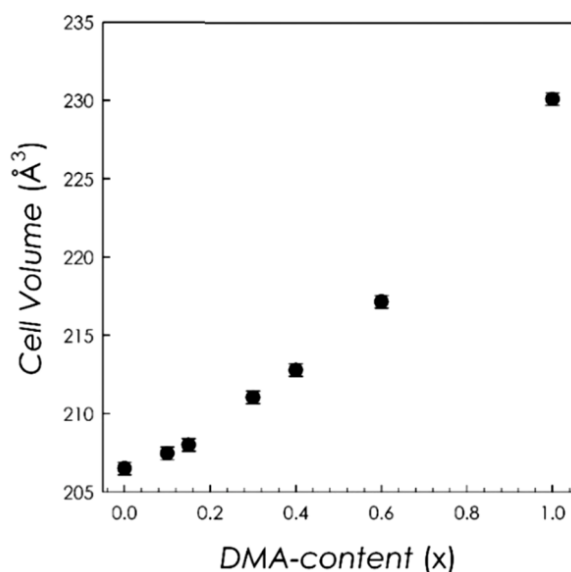


Figure 4.9: Lattice volume as a function of x for the $MA_{1-x}DMA_xSnBr_3$

The trend of the absorption measurements for the single-phase samples of the $MA_{1-x}DMA_xSnBr_3$ system, *i.e.* all the samples reported in Fig. 4.9, are plotted in Fig. 4.10a, while Fig. 4.10b reports the Tauc plots determined from the absorption measurements. These last data were used to determine the energy bandgap of the samples. The spectra reported below show a continuous blue shift of the data by increasing the amount of DMA into the lattice. The bandgaps (E_g) estimated from the data of Figure 4.10b are reported in

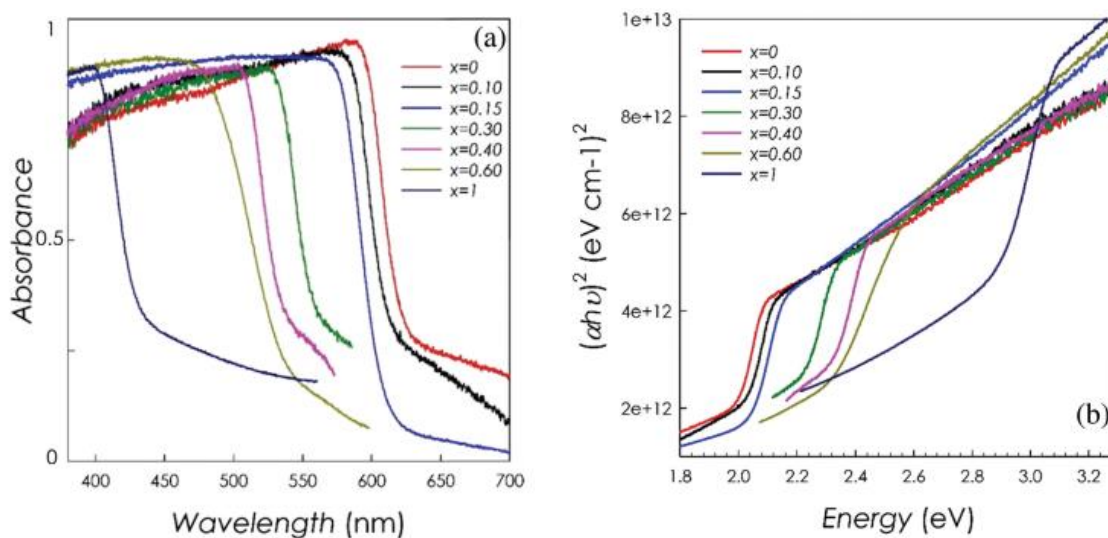


Figure 4.10: (a) Absorption spectra of the single-phase samples of the $MA_{1-x}DMA_xSnBr_3$ system from $MASnBr_3$ (red) to $DMASnBr_3$ (dark blue); (b) Tauc plots determined from the absorption measurements

Table 1 as a function of DMA-content, together with lattice parameters. The E_g value of about 2 eV for $MASnBr_3$ reported here is in agreement with the previous report.⁷ On the other hand, only the color (off-white) of $DMASnBr_3$ has been reported in the paper discussing the single crystal structure of this phase, and that information is in agreement with the measured band-gap of about 2.88 eV.¹⁴ The analogous Pb-containing dimethylammonium halide, *i.e.* $DMA PbBr_3$, has been characterized by our group and

shows a band-gap of about 3.03 eV, thus confirming the red-shift usually found when substituting Sn for Pb.²⁰ Another interesting difference between DMASnBr_3 and the Pb-analogue is the crystal structure. While DMASnBr_3 crystallizes in an orthorhombic distorted perovskite structure, DMAPbBr_3 has a non-perovskite hexagonal crystal structure.²⁰ This last evidence was interpreted as a consequence of a tolerance factor higher than 1 which is, however, also the case for DMASnBr_3 which, however, not only crystallizes into a perovskite lattice, but also into a distorted one, typical of materials with a tolerance factor significantly lower than 1. The increasing availability of structural data of hybrid perovskites with organic cations different from the usual MA and FA, highlights the fact that the use of the tolerance factor arguments when dealing with organic-inorganic hybrid materials containing large cations should be done with care. Plotting the band gap data reported in Table 4.1 (Figure 4.11), it is possible to note that the blue shift of the $\text{MA}_{1-x}\text{DMA}_x\text{SnBr}_3$ optical properties with increasing amount of DMA follows a nearly linear trend. The absorption spectra of the two samples which resulted, from the XRD analysis, to be composed of a mixture of a cubic and an orthorhombic phase ($x = 0.70$ and 0.80), are shown in Figure 4.12. They show very broad absorbance composed of two clear components with the first absorption falling in the region of DMASnBr_3 , thus supporting the conclusion derived from diffraction. The study of the present solid solution has been further extended by looking at its stability against

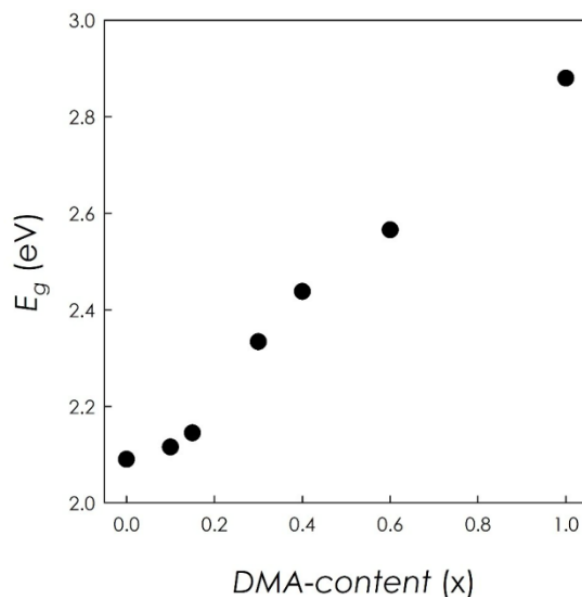


Figure 4.11: Band gap as a function of x for $\text{MA}_{1-x}\text{DMA}_x\text{SnBr}_3$ samples

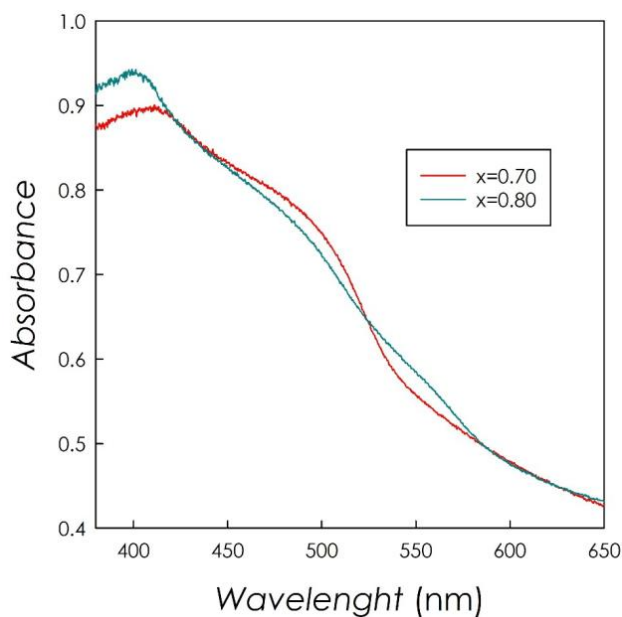


Figure 4.12: Absorption spectra of the $\text{MA}_{1-x}\text{DMA}_x\text{SnBr}_3$ samples for $x=0.7, 0.8$

moist air by keeping selected samples in open containers in the laboratory environment (22 °C, RH about 40%). Such study has been conducted on the two end members of the solid solution, namely MASnBr_3 and DMASnBr_3 , at 1 day and 6 days of exposure and recording XRD patterns and absorption spectra and also trying to correlate the results to the actual Sn oxidation state by X-ray photoelectron spectroscopy (XPS).

This kind of investigation is of general relevance in the field of hybrid organic–inorganic perovskites and in particular when Sn(II) is present. Further interest in such studies comes from the proposed use of 2D systems as a good way of reducing the sensitivity of hybrid materials to external factors as a consequence of the presence of a layer of large organic cations.²¹ Even in a simple 3D perovskite system, it is possible that a bigger organic cation such as DMA could enhance the chemical stability. Fig. 4.13a and 4.13b report the XRD data and the absorption spectra of MASnBr_3 after synthesis (“as-prep”: the sample has been always kept in a glovebox) and after 1 day and 6 days of exposure to the laboratory environment.

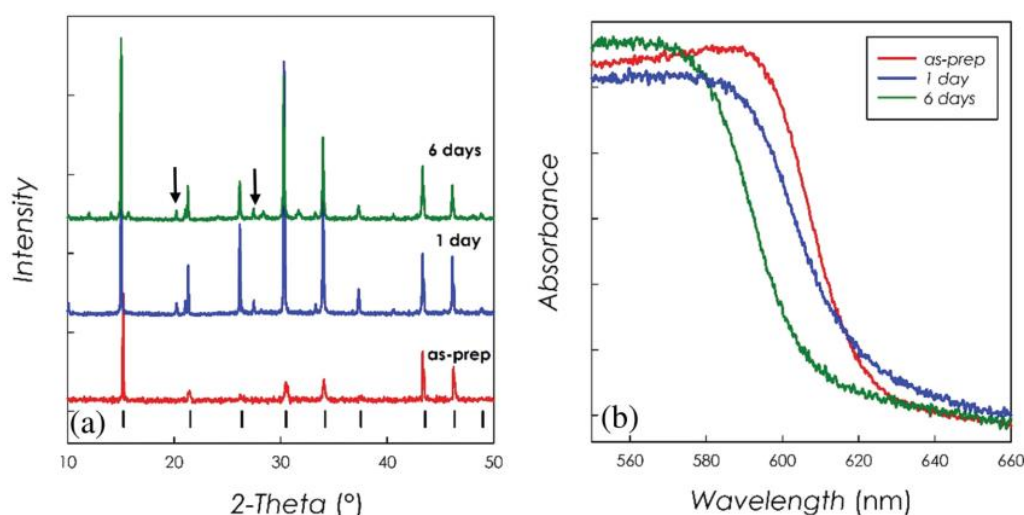


Figure 4.13: (a) XRD of MASnBr_3 after synthesis (“as prep”) and after 1 day and 6 days of air exposure, black vertical bars refer to the cubic perovskite cell of MASnBr_3 and (b) absorption spectra of the same samples

The XRD data reported in Fig. 4.13a show that additional peaks are found after 1 day of air-exposure (marked with arrows in the figure). At the end of the aging test (6 days) the main crystalline phase has been conserved but several further peaks can be seen in the pattern. However, it is of relevance to note that even under these conditions, the cubic phase of MASnBr_3 still represents the majority of the sample. Interestingly, the cubic cell volume is practically constant even for the aged samples, as shown in the table beside. The additional diffraction peaks found in the patterns of the aged samples could

not be related to any starting reagent (MABr or SnBr₂) or to simple oxidation products of tin and, possibly, mixed unknown phases could be formed. The amount of these spurious phases is too small for reliable phase identification and further work is planned to understand their exact nature. The absorption spectra of the aged samples, reported in Fig. 4.12b, show a slight while progressive blue-shift along with the air-exposure of the sample. Overall, the absorption edge maintains a sharp shape and the estimated bandgap moves from about 2.05 to 2.09 eV passing from the “as-prepared” sample to the one aged for 6 days.

An analogous aging-test has been carried out for the other endmember of the solid-solution, namely DMASnBr₃, and the XRD and absorption data are reported in Figure 4.14a and 4.14b, respectively.

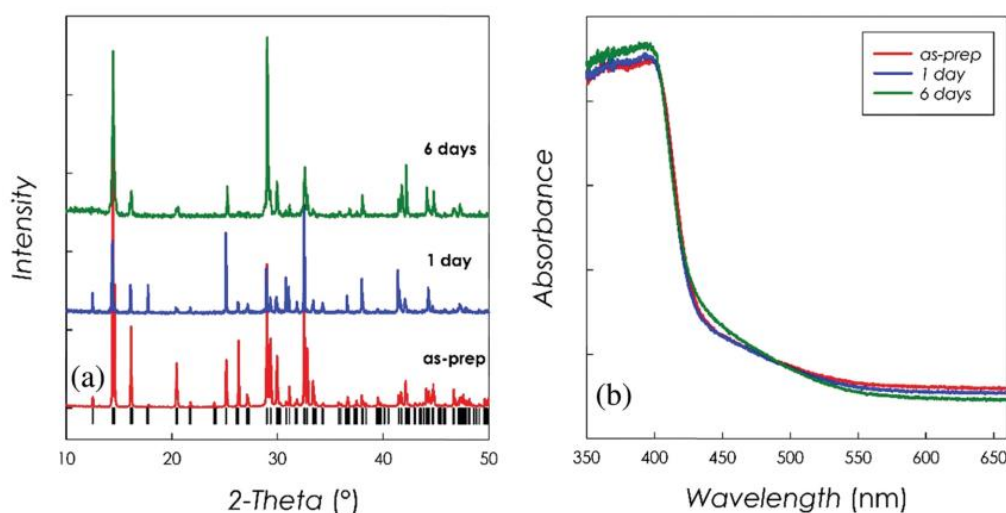


Figure 4.14: (a) XRD of DMASnBr₃ after synthesis (“as prep”) and after 1 day and 6 days of air-exposure, black vertical bars refer to the orthorhombic perovskite cell of DMASnBr₃ and (b) absorption spectra of the same samples

In the case of DMASnBr₃, it is interesting to note that the diffraction patterns do not change with air-exposure, as can be seen by comparing the data of Figure 4.14a with the reference pattern of the orthorhombic perovskite structure of DMASnBr₃ reported at the bottom of the plot (vertical black bars). The differences which can be observed between the patterns are only due to iso-orientation effects of the crystals (which have a typical needle-like shape). The lattice parameters, also in this case, do not show any appreciable difference, except for a slight reduction in the unit cell size (data reported in Table 4.2) along with the aging time. At the same time, a striking feature of the DMASnBr₃ aged samples is the invariance of the absorption spectra reported in Figure 4.14b. This result agrees well with the trend of the XRD patterns but it is quite unexpected considering the common – more or less pronounced – air-instability of

Sample	<i>a</i> (Å)	<i>b</i> (Å)	<i>c</i> (Å)
<i>x</i> =0 As-prep	5.9129(5)	5.9129(5)	5.9129(5)
<i>x</i> =0 1- day	5.9127(5)	5.9198(5)	5.9198(5)
<i>x</i> =0 6 - days	5.9112(5)	5.9210(6)	5.9210(6)
<i>x</i> =1 As-prep	12.3216(4)	12.1812(3)	12.3265(3)
<i>x</i> =1 1- day	12.3145(4)	12.1791(3)	12.3042(3)
<i>x</i> =1 6 - days	12.2895(6)	12.1737(5)	12.2917(5)

Table 4.2: Lattice parameters of $MASnBr_3$ and $DMASnBr_3$ aged sample at 1- and 6-days

Sn(II)-containing phases, as also reported for $MASnBr_3$ in Figure 4.12a and b. Very recently, a study on $DMASnI_3$ single crystals, reported an unusual band-gap reconstruction due to aging of the pristine phase which changed from yellow to black by air exposure in few minutes.²¹ In that paper, the authors claimed that such change is due to the formation of iodide vacancies and that the crystal structure is not changing upon air exposure. This may not be fully consistent, as we prepared both the yellow and black phases of $DMASnI_3$ and

observed few changes in the patterns (reported in Figure 4.15) at a low angle.

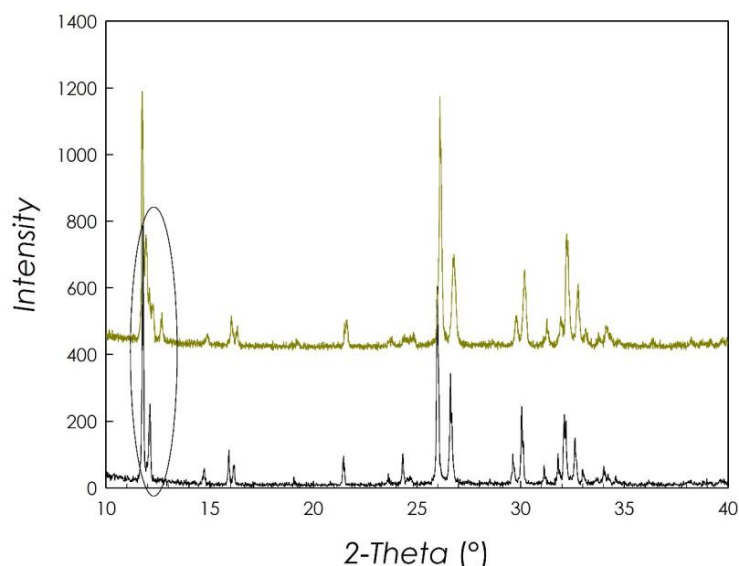


Figure 4.15: X-ray diffraction pattern of black and yellow phases of $DMASnI_3$. The intensity in the pattern of yellow phase has been shifted by 400 for ease of visualization

However, further investigation of $DMASnI_3$ is beyond the scope of the present paper. We just highlight that $DMASnBr_3$ does not present any change in the optical properties upon moist air exposure. The origin of this improved stability when DMA is present in the lattice needs further investigation, also with computational modelling, but it could be correlated to an increased possibility of hydrogen bond formation which promotes moisture-stability, as recently shown to occur in guanidinium-based hybrid perovskites.²²

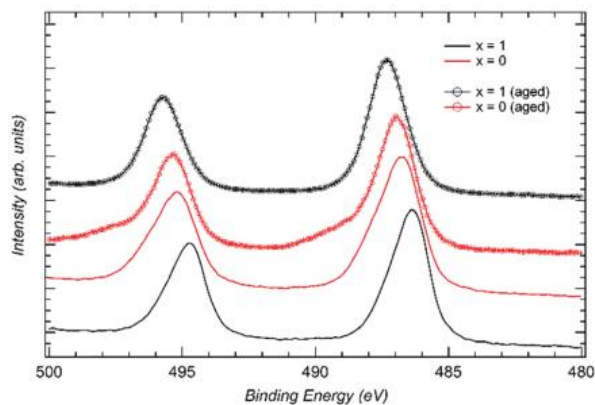


Figure 4.16: Sn 3d XPS data for “as-prepared” and 6-days aged MASnBr_3 ($x=0$) and DMASnBr_3 ($x=1$)

In order to further characterize the aged samples, we performed XPS analysis of the 6-days aged MASnBr_3 and DMASnBr_3 samples, focusing on the possible changes in the oxidation state of tin. XPS data have been recorded on a properly calibrated VG-Scientia R3000 analyzer with a Mg K α line of a PsP anode source.²³ Figure 4.16 shows the Sn 3d XPS peaks of the “as-prepared” samples (black and red lines) and of the samples after 6 days of aging (round markers). In Figure 4.16, it is possible to observe slightly different binding energies for as-prepared samples, probably due to the different chemical environment. After 6 days of aging the spectra show a strong shift toward lower binding energies, which corresponds to a higher valence state; this shift is particularly noticeable for the DMASnBr_3 case. This energy shift has been observed only on Sn photoelectron peaks and thus could not be ascribed to XPS surface charging effects. It is interesting to note that the XPS data suggest that a certain degree of Sn(II) oxidation is also present in DMASnBr_3 which however preserves the crystal structure and the absorption properties (see Figure 4.14a and b) after air-exposure. Similar oxidation of Sn(II) to Sn(IV) in MASnBr_3 has a bigger impact on both structure and optical properties (see Fig. 4.13a and b). It can be concluded that DMASnBr_3 can in some way tolerate a partial oxidation of tin without altering its structural and optical characteristics and this point is worth of further investigation. Triggered by the improved stability of DMASnBr_3 we also performed a test by immersing the material into deionized water (DI). We observed that the hybrid perovskite does not dissolve but forms an opalescent solution and once the material is dried, the pristine phase is formed. In view of this peculiar behavior, we preliminarily tested DMASnBr_3 as a possible photocatalyst for hydrogen production. The experiment was carried out as indicated in the experimental section by suspending 2 g L⁻¹ of DMASnBr_3 in DI and irradiating the solution under simulated solar light using a Solar Box with a power factor of 500 W m². In this peculiar experiment no co-catalysts were used. In parallel with the DI containing the perovskite, we also tested a sample made only of DI as a reference (control sample). The intriguing result was the observation of hydrogen photoproduction on the order of

6 $\mu\text{mol g}^{-1} \text{h}^{-1}$ for DMASnBr_3 (the reference sample provided an undetectable amount of H_2).

SAMPLE	H_2 Production ($\mu\text{mol/g/h}$)
$\text{DMASnBr}_3 + \text{DI}$	6
$\text{DMASnBr}_3 + \text{DI} + \text{TEOA } 10\% + 1 \text{ wt}\% \text{ Pt}$	11
DI	0.0
DI+TEOA	0.0

Table 4.3: Results of hydrogen production

An additional experiment in the presence of triethanolamine (as a donor) and 1 wt% of Pt led to the production of 11 $\mu\text{mol g}^{-1} \text{h}^{-1}$ of hydrogen. While this performance may be quite low with respect to the most active photocatalysts, it is an encouraging result also considering the bulk nature of the phase used and the significant activity also in absence of a co-catalyst. Such results may further prompt a rich experimental research by designing nanocrystals of this phase as well as by employing DMASnBr_3 in photocatalytic nanocomposites.

Conclusions

In this paper we reported the synthesis and characterization of a novel Sn-based system with MA/DMA alloying at the A-site of the perovskite structure. The limit of the $\text{MA}_{1-x}\text{DMA}_x\text{SnBr}_3$ solid solution is found at about $x = 0.60$. The crystal structure remains cubic for all the mixed phases, in agreement with the symmetry of the MASnBr_3 endmember, and a progressive increase in the cell volume is found with the increase in content of the bigger DMA cation. As for the optical properties, the replacement of DMA for MA leads to a progressive blue-shift of the absorbance edge from about 2.0 eV for $x = 0$ to 2.9 eV for $x = 1$. Due to the presence of Sn(II) in this system, we were able to study the stability of samples by exposing the powdered samples to moist air in the laboratory. The results indicate a slight aging effect on MASnBr_3 with the appearance of additional peaks in the diffraction patterns and a slight blue-shift from the fresh sample to the most aged one (6 days). On the other hand, the other endmember of the solid solution, *i.e.* DMASnBr_3 , is very stable against aging. The diffraction patterns of the fresh sample and aged samples have no detectable differences and, most importantly, the absorption spectra of fresh 1- and 6-days aged samples are superimposable. This is an unexpected while exciting result for a Sn(II) containing hybrid perovskites. The XPS data collected show that a degree of tin oxidation may be present in the samples aged for 6 days.

However, while such effect corresponds to changes in the diffraction and optical properties of MASnBr_3 , DMASnBr_3 seems to be robust against partial oxidation of Sn(II). The improved stability of DMASnBr_3 is possibly related to the hydrogen bonding network and/or related to the electronic structure of this phase and modelling studies will be performed to clarify such aspect. The analogous I-based phase, *i.e.* DMASnI_3 , does not show such level of stability and the formation of iodide vacancies with time has been proposed to occur with aging.²¹ In analogy with 2D-perovskites where the presence of a full layer of relatively big organic cation preserve the perovskites from degradation, it may be possible that large cations in 3D perovskites have an analogous effect and make such phases highly air-stable. Finally, we reported preliminary results indicating an effective hydrogen photogeneration of $6 \mu\text{mol g}^{-1} \text{h}^{-1}$ for DMASnBr_3 in deionized water under simulated solar light which merits to be further investigated from an experimental and theoretical point of view.

Experimental Section

Synthesis. All the samples of general formula $\text{MA}_{1-x}\text{DMA}_x\text{SnBr}_3$ (with nominal $x = 0, 0.10, 0.15, 0.30, 0.40, 0.60, 0.70, 0.80$ and 1) were synthesized according to a general and original procedure we developed.²⁰ In a typical synthesis, a proper stoichiometric amount of Sn acetate is dissolved in an excess of HBr under continuous mechanical stirring under a nitrogen atmosphere. Hypophosphoric acid is added to the solution and an inert atmosphere is maintained in the reaction environment in order to prevent Sn oxidation. Subsequently, the solution is heated to $100 \text{ }^\circ\text{C}$ and the corresponding amine solutions (40 wt% in water) are added in the stoichiometric amount to achieve the desired MA : DMA ratio. The as-obtained final solution is then cooled down to $46 \text{ }^\circ\text{C}$ at $1 \text{ }^\circ\text{C min}^{-1}$, until the formation of a precipitate, that is immediately filtered and dried under vacuum overnight. All the reagents were purchased from Sigma Aldrich in pure form and were used without any further purification. The final products are handled and stored in a glove box with oxygen and water contents lower than 1 ppm. To check the reliability of the result, several batches of most of the samples have been done, confirming the same results in terms of structures and optical properties.

Diffraction. The crystal structure of the samples has been characterized at room temperature. Cu-radiation laboratory X-ray powder diffraction (XRD) patterns were acquired on a Bruker D5005 diffractometer using a Bruker dome sealed in the glove box avoiding air exposure. Diffraction data have been refined according to the Rietveld method to derive cell parameters and volume with the use of the FullProf package.³

Optical properties. The optical diffuse reflectance spectra of the different perovskites were measured from 0.8 to 4.5 eV (250–1500 nm, with steps of 1 nm) using a Varian Cary 6000i instrument equipped with an integrating sphere. For this kind of measurements, polycrystalline powders were loaded in 1 mm optical path cuvettes made of special optical glass (Hellma). All the manipulations and measurements of the samples have been carried out under inert conditions in order to avoid tin oxidation.

XPS experimental details. XPS data have been recorded on a VG-Scienta R3000 analyzer operating in a spatial resolved acquisition mode with the Mg Ka line of a PsP anode source.²³ Samples have been pressed into pellets and mounted on the sample holder with a carbon-based paste; samples did not show any signs of discoloration after X-ray exposure, which lasted 12 h for each considered sample. The base pressure in the measurement chamber was $2 \cdot 10^{-10}$ mbar. We used the C 1s environmental contamination peak (set at a binding energy of 284.8 eV) as the reference for binding energy scale calibration. The final energy resolution was 0.85 eV.

Photocatalytic hydrogen gas production tests. Experiments were conducted in aqueous solution with and without triethanolamine (TEOA, Z99% Sigma-Aldrich) (10%, v/v) irradiated in Pyrex glass containers (28 mL capacity, 21 mL sample). After the addition of the catalyst (2 g L^{-1}), the suspension was deoxygenated by Ar (99.999%, Sapio S.r.l.) bubbling (20 min) to obtain anoxic conditions, and irradiated under magnetic stirring for 5 h. Pt was loaded on the catalyst surface (1 wt%) by in situ photo deposition using H_2PtCl_6 (~38% Pt basis, Sigma-Aldrich). Irradiation was performed under simulated solar light using a Solar Box 1500e (CO.FO.- ME.GRA S.r.l., Milan, Italy) set at a power factor 500 W m^{-2} and equipped with UV outdoor filter of IR-treated soda lime glass. The headspace evolved gas was quantified by gas chromatography coupled with thermal conductivity detection (GC-TCD), as previously described (see ref. Photochem. Photobiol. Sci. 2014, 13, 1410–1419). Results in the manuscript are expressed in terms of the H_2 evolution rate (HER), as $\mu\text{moles of evolved gas per gram of the catalyst per hour}$ ($\mu\text{mol g}^{-1} \text{ h}^{-1}$).

References

1. N. J. Jeon, J. H. Noh, W. S. Yang, Y. C. Kim, S. Ryu, J. Seo and S. Seok, *Nature*, 2015, 517, 476.
2. N. Pellet, P. Gao, G. Gregori, T.-Y. Yang, M. K. Nazeeruddin, J. Maier and M. Graetzel, *Angew. Chem., Int. Ed.*, 2014, 53, 3151.
3. T. J. Jacobsson, J.-P. Correa-Baena, M. Pazoki, M. Saliba, K. Schenk, M. Graetzel and A. Hagfeldt, *Energy Environ. Sci.*, 2016, 9, 1706.

4. W. S. Yang, J. H. Noh, N. J. Jeon, Y. C. Kim, S. Ryu, J. Seo and S. Seok, *Science*, 2015, 348, 1234.
5. Y. Zhou, Z. Zhou, M. Chen, Y. Zong, J. Huang, S. Pang and N. P. Padture, *J. Mater. Chem. A*, 2016, 4, 17623–17635.
6. A. Pisanu, C. Ferrara, P. Quadrelli, G. Guizzetti, M. Patrini, C. Milanese, C. Tealdi and L. Malavasi, *J. Phys. Chem. C*, 2017, 121(16), 8746–8751.
7. C. Ferrara, M. Patrini, A. Pisanu, P. Quadrelli, C. Milanese, C. Tealdi and L. Malavasi, *J. Mater. Chem. A*, 2017, 5, 9391–9395.
8. D. Chi, S. Huang, M. Zhang, S. Mu, Y. Zhao, Y. Chen and J. You, *Adv. Funct. Mater.*, 2018, 28, 1804603.
9. E. L. Unger, L. Kegelmann, K. Suchan, D. Soerell, L. Korte and S. Albrecht, *J. Mater. Chem. A*, 2017, 5, 11401–11409.
10. S. Shao, J. Liu, G. Portale, H.-H. Fang, G. R. Blake, G. H. ten Brink, L. J. Anton Koster and M. A. Loi, *Adv. Energy Mater.*, 2018, 8, 1702019.
11. O. Nazarenko, M. R. Kotyrba, S. Yakunin, M. Aebli, G. Raino, M. B. Benin, M. Woerle and M. V. Kovalenko, *J. Am. Chem. Soc.*, 2018, 140, 3850–3853.
12. A. D. Jodlowski, C. Roldan-Carmona, G. Grancini, M. Salado, M. Ralaiarisoa, S. Ahmad, N. Koch, L. Camacho, G. de Miguel and M. K. Nazeeruddin, *Nat. Energy*, 2017, 2, 972–979.
13. L. Dimesso, A. Quintilla, Y.-M. Kim, U. Lemmer and W. Jaegermann, *Mater. Sci. Eng., B*, 2016, 240, 27–33.
14. M. Daub and H. Hillebrecht, *Z. Anorg. Allg. Chem.*, 2018, 644, 1393–1400.
15. W. M. J. Franssen, B. J. Bruijnaers, V. H. Portengen and A. P. M. Kentgens, *ChemPhysChem*, 2018, 19, 3107–3115.
16. W. Ke, I. Spanopoulos, C. C. Stoumpos and M. G. Kanatzidis, *Nat. Commun.*, 2018, 9, 4785.
17. C. Anelli, M. R. Chierotti, S. Bordignon, P. Quadrelli, D. Marongiu, G. Bongiovanni and L. Malavasi, *Inorg. Chem.*, 2019, 58, 944–949.
18. G. Kieslich, S. Sun and A. K. Cheetham, An extended Tolerance Factor approach for organic–inorganic perovskites, *Chem. Sci.*, 2015, 6, 3430.
19. G. Thiele and B. R. Serr, *Z. Kristallogr.*, 1996, 211, 47.
20. A. Mancini, P. Quadrelli, G. Amoroso, C. Milanese, M. Boiocchi, A. Sironi, M. Patrini, G. Guizzetti and L. Malavasi, *J. Solid State Chem.*, 2016, 240, 55–60.
21. D. Ju, X. Zheng, J. Liu, Y. Chen, J. Zhang, B. Cao, H. Xiao, O. F. Mohammed, O. M. Bakr and X. Tao, *Angew. Chem., Int. Ed.*, 2018, 57, 14868–14872.

22. A. D. Jodlowski, C. Roldan-Carmona, G. Grancini, M. Salado, M. Ralaiarisoa, S. Ahmad, N. Koch, L. Camacho, G. de Miguel and M. K. Nazeeruddin, *Nat. Energy*, 2017, 2, 972–979.
23. G. Drera, G. Salvinelli, J. Ahlund, P. G. Karlsson, B. Wannberg, E. Magnano, S. Nappini and L. Sangaletti, *J. Electron Spectrosc. Relat. Phenom.*, 2014, 195, 109–116.

CHAPTER 5.

ANION SUBSTITUTION IN NANOCRYSTALS

When a comprehensive understanding about substitution mechanisms has been acquired, we decided to exploit it in another field of hybrid perovskites: in fact, this experimental chapter of the thesis focus on substitution on perovskite nanocrystals. Before talking specifically about the anionic exchange, it is necessary to introduce something about the big world of colloidal semiconducting nanocrystals, without falling in rigorous and detailed descriptions of the physics and chemistry behind them, which can be found in classical textbooks and it is not the aim of this thesis.

Semiconductors are one of the most important type of materials in our daily lives as they are the core of every diode, transistor, LED and processor. Since the society relies on so many devices based on semiconductors much research has been devoted to synthesizing them with new and efficient compositions. One interesting way of implementing semiconductors is by producing them in form of colloidal nanocrystals, which not only decrease their size, allowing for smaller devices, but also opens the possibility for a new and easy way of properties tuning, due primely to the size depended quantum confinement effects. This additional property tunability has driven the scientific community to the “nano” world. Colloidal means that these NCs can be synthesized as small, stable solid NCs in a solution, which does not only allow for more control over the size, shape and composition, but also has a large processability advantage, as colloidal solutions can be deposited using simple deposition techniques.

Mainly driven by the field of photovoltaics, lead halide perovskites (LHPs) are one of the latest materials to be added to the family of colloidal NCs (69) and the first report on LHPs NCs started to emerge in 2015 (70). These nanocrystals have a “soft” and predominantly ionic lattice, for this reason they form within seconds even at room-temperature (RT), from a vast selection of precursors and the optical and electronic properties are highly tolerant to structural defects making them deeply different from the conventional chalcogenides NCs.

Initially the synthesis and processing of LHPs NCs were approached with the same methods as conventional QDs. For example, ligand-assisted hot-injection was used to synthesize the first CsPbX₃ NCs, the first to exhibit bright PL over the entire visible spectral range, without electronic surface passivation and characterized by high PLQYs up to 90% and a narrow FWHM in the range of 12-42 nm (70). An alternative strategy is the ligand-assisted re-precipitation method, wherein an ionic solution of the respective ions in a polar solvent is rapidly destabilized by mixing with a non-solvent inducing a burst of nucleation, as originally proposed for MAPbBr₃ NCs (71). In both methods, the reaction conditions can be adjusted to yield non-cuboidal shapes, such as nanoplatelets, nanowires, etc. (72) (73) (74) (75). Other facile routes include microwave-assisted synthesis, sonication in solvent/ligand mixture and ball-milling (76) (77) (78)

As they bulk counterpart, stability will remain the foremost challenge for LHP NCs in the research spotlight. A funny sentence about this NCs is that:

As easy as it is to make them, it is just as easy to break them.

Hence, the retention of their colloidal and structural integrity during isolation, purification and handling has been a problem of huge importance. LHP NCs are terminated by oleyl ammonium halide and/or oleyl ammonium carboxylate. These ligands tend to quickly desorb. (79) The most dramatic consequence of such loss is the difficulty met in isolating and purifying colloids using standard methods for QDs.

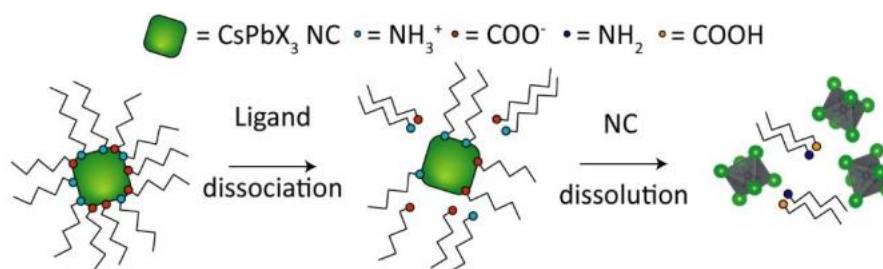


Figure 5.1 Structural lability of LHP NCs

To obtain a more stable ligand shell, ligands containing several anchoring groups, such as zwitterionic molecules, with quaternary ammonium and carboxylate groups (or sulfonate, phosphonate, or other groups) could be used. Oligomeric ligands with a larger number of these charged groups and long hydrocarbon chains per molecule can be considered as well. Due to the fairly ionic bonding character and low crystal lattice energy, LHPs are soluble in nearly all polar organic solvents; in practice, this eventually disintegrates LHP NCs upon exposure to such solvents. This problem will remain difficult to mitigate until a strategy for the full encapsulation of individual LHP

NCs in an inert shell is identified (for instance, within silica, titania, alumina, salts with extremely low solubility products such as BaSO_4 or similar). As a result of LHP NCs being so fragile, complex morphologies, such as core-shell NCs and other NC heterostructures, have not been demonstrated to this date. A promising alternative path to stable LHP emitters is the melt-growth of glass-embedded LHP NCs, such as in recent reports employing typical phosphate or borosilicate glasses. (80) (81) (82) Thus-obtained crystalline NCs, whose size is tunable by melt-quenching and by adjusting the subsequent thermal conditions, are surrounded by an amorphous, chemically stable, water- and oxygen-impermeable glass matrix. LHP NCs are all highly prone to sintering. This poses a great challenge for any device architecture relying on the retention of quantum-confined states in a densely packed array of LHP NCs or for devices operating at elevated temperatures, such as lasers or remote phosphors.

Another form of structural lability is observed in red-emitting CsPbI_3 . In this case, the Cs^+ ions are too small to be included in a 3D perovskite Pb-iodide cage, causing the transition to another polymorph of a lower dimensionality and, hence, a much wider bandgap. (83) Considerable work has been done, both with NCs and thin films, to stabilize CsPbI_3 by partially replacing Cs^+ with larger cations (the foremost example being FA^+), and by partially replacing I⁻ with Br⁻. (84) (85)

5.1 Exploitation of lability in post-synthetic reactions

The high ionicity and structural instability of LHP NCs can also be exploited for post-synthetic reactions, either with the retention of the original crystal structure, or through reorganization into a new one. Such transformations take place while preserving the overall NC size and shape, or at least the initial size uniformity (84) (86) (87), as depicted in the Figure 5.2.

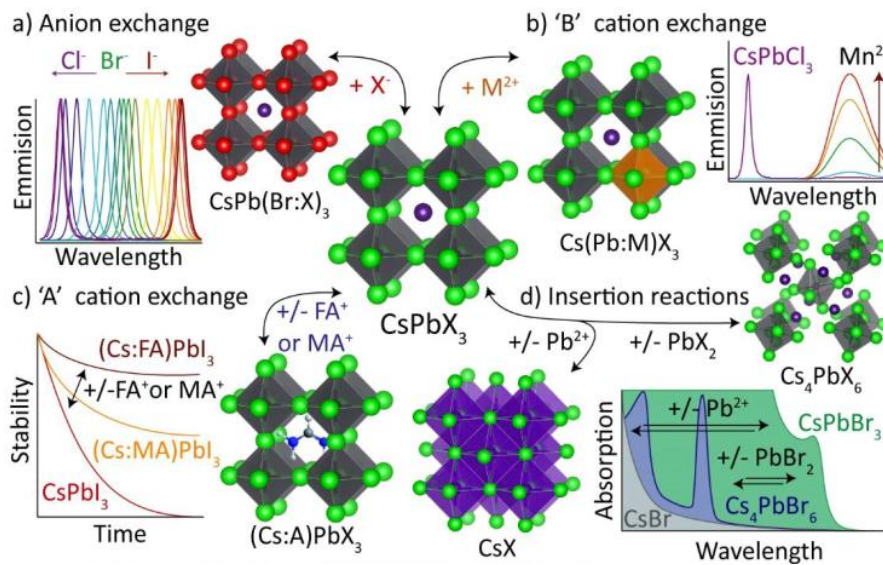


Figure 5.2 Structural and compositional post-synthetic engineering of lead halide

Anion exchange (5.2a) enables bandgap tuning over the whole visible spectrum, B-cation exchange (5.2b) allows the study of the optical properties of other divalent metals such as Mn^{2+} in an LHP environment, A-cation exchange (5.2c) allows the tuning of the thermodynamic stability but there can be also a phase transformation from 3D to other dimensionalities

5.2 FA_{0.8}Cs_{0.2}Pb(Br/X)₃

Facile anion-exchange reaction in mixed-cation lead bromide perovskite nanocrystals

Purpose and Scope



Figure 5.3: Dispersion of FAPbBr₃ NCs in toluene under daylight (left panel) and under UV lamp (right panel)

The idea of synthesizing nanocrystals of hybrid perovskites came out at the end of my first year of PhD, when we tried to reproduce the synthesis of monodisperse formamidinium lead bromide nanocrystals reported by the group of Kovalenko (88). The excellent results obtained convinced us to continue working on this type of materials. Beyond the new and unique optical properties and all the charming applications, one of the most appealing aspects of these nanocrystals is their

broadly tunable photoluminescence, modulation that is carried out by preparing solid solutions of the cations or the anions.

The most endearing strategies are post-synthetic exchange reactions of the anion, but the most common anion-exchange reaction reported in literature requires the use of halide precursors difficult to synthesize, high temperatures and inert atmosphere.

In this paper it is described a new simple and fast anion exchange reaction applied to a mixed-cation sample, namely FA_{0.8}Cs_{0.2}PbBr₃, which just employs lead halide precursors at room temperature. This brand-new procedure allowed us to achieve a significant shift in the nanocrystal's emission: within 30 minutes reaction time and a molar ratio between the NCs and the halide precursors of 1 : 1, it was possible to cover more than 120 nm in the visible region. The exchanged NCs maintained their cubic-shaped morphology and narrow emission peak width for the whole compositional range explored. The present approach also allowed for a reduction in solvent use, since it does not require any halide precursor synthesis nor complex post-synthesis treatments.

Introduction

Lead halide semiconductors with a perovskite crystal structure have been thoroughly investigated during the last several years as a new class of optoelectronic materials. Starting with photovoltaic applications, with power conversion efficiencies beyond 22%, they are now particularly attractive in applications such as light-emitting devices, lasers and photodetectors.¹⁻⁵ The majority of research has focused on bulk, single crystals and thin films perovskites, while colloidal synthesis to hybrid or to fully inorganic perovskite nanocrystals is a completely new method firstly reported in 2015.⁶ Controlled size reduction to the nanoscale dimension is a challenging issue because it gives rise to brand new and unique properties which pave the way for different research directions and applications.

Cesium and formamidinium lead halide nanocrystals have been shown to retain striking optical properties such as broadly tunable photoluminescence adjusting the nanocrystal size, small full width at half-maxima and high photoluminescence (PL) quantum yields up to 90%. In the future, the most viable application of these nanocrystals will be in television displays and related devices.^{6,7} Mixed cations perovskites show a significant enhancement of the power conversion efficiency and improved stability, in particular Zhang et al. proved that the optimized composition $\text{FA}_{0.8}\text{Cs}_{0.2}\text{PbBr}_3$ exhibit a superior behaviour than others compositions in terms of high quantum efficiency, proper energy level and air stability, which together contribute to its outstanding luminance performance (55005 cd m^{-2}) in the LEDs.⁸

Beyond the optical properties and the charming applications, one of the most appealing aspect of perovskites nanocrystals is their wide band gap tunability. Up to now the modulation of the band gap has been carried out above all at the synthesis step, by preparing different compositions or solid solutions of the cations or the anions.⁷⁻¹⁵ However, appealing post-synthetic strategies rely on the anion exchange of the prepared colloidal nano-dispersions, as it has been previously demonstrated on CsPbBr_3 .¹⁶⁻²² One of the most common routes for anion exchange in lead halide nanocrystal was reported by Nedelcu et al. and makes use of Schlenk line where lead halogens and OAmX as anion sources were mixed with octadecene (ODE) in neck flask and kept under vacuum at 120 °C. The dried oleic acid (OA) and oleyl amine (OLA) were injected at 120 °C under N_2 flow.¹⁷ While this approach is highly suitable to provide a full anion exchange, it would be desirable to provide more easy and facile routes to perform such anion modification on lead halide nanocrystals and also provide evidence of such exchange on mixed cation compositions.

For these reasons, in this work we selected the $\text{FA}_{0.8}\text{Cs}_{0.2}\text{PbBr}_3$ optimized composition to perform a halide exchange reaction with I and Cl providing a facile and fast method to perform it.

Experimental

Preparation of oleyl ammonium bromide (OAmBr). Ethanol (100 mL, Aldrich, absolute) and oleyl amine (OLA, 12.5 mL, Acros Organics) were combined in a 3-neck flask under vigorous stirring. The solution was cooled in an ice-water bath and 8.56 mL HBr (48% aqueous solution, Aldrich) were added very slowly and then the mixture was left to react overnight under N_2 flow. The next day the reaction mixture was cooled again in an ice-water bath for 2 hours. The product (a white powder) was obtained after filtering, purifying by rinsing multiple times with diethyl ether and vacuum-drying at 60 °C in an Abderhalden's drying pistol overnight.

Synthesis of $\text{FA}_{0.8}\text{Cs}_{0.2}\text{PbBr}_3$. It follows the typical hot-injection method described by Protesescu et al. in their work⁷ on formamidinium nanocrystals: a precursor solution was prepared using Pb (0.2 mmol), formamidinium (FA) (0.6 mmol) and Cs (0.15 mmol) acetates (Sigma Aldrich) with dried oleic acid (2 mL, Acros Organics) and dried octadecene (8 mL, Acros Organics); at 130 °C, under N_2 flow, oleyl ammonium bromide (0.6 mmol) dissolved in toluene (2 mL) was injected. After few seconds the nanocrystals were quenched in ice, to the crude solution were added 10 mL of toluene and 5 mL of acetonitrile and the mixture was centrifuged for 5 min at 12 krpm. The precipitate was dispersed in 5 mL of toluene.

Exchange reactions. The anion exchange reactions reported were conducted at room temperature in toluene by mixing a specific ratio of the desired lead halide salt. In particular, 0.113 mmol of PbX_2 were loaded in 4 mL of $\text{FA}_{0.8}\text{Cs}_{0.2}\text{PbBr}_3$ NCs toluene solution 28.3 mM, followed by 1, 5, 10, 15 and 30 minutes of vigorous stirring. The transparent dispersion was immediately separated from the solid phase by centrifugation and then analyzed.

X-ray diffraction. The crystal structures of the samples were characterized by room temperature Cu-radiation Powder X-ray diffraction (XRD) on a Bruker D8 diffractometer. Scans were performed in the 10–40 range, with a step size 0.04 and a counting time of 3 s per step.

Absorbance. UV-Vis absorption spectra for colloidal solutions were run on Varian Cary 50 Scan spectrophotometer in absorbance mode with quartz cuvettes of 1 cm path length.

Photoluminescence (PL). A PerkinElmer LS 50B spectrofluorometer was used to acquire steady-state PL spectra from colloidal solutions.

Transmission electron microscopy (TEM). TEM images were collected on a JEOL JEM-1200 EX II microscope operating at 100 kV (tungsten filament gun) and equipped with the TEM CCD camera Olympus Mega View G2 with 1376 1032-pixel format. Samples were prepared by drop-casting the solution on coated copper grids.

Results and discussion

The synthesis of the optimized $\text{FA}_{0.8}\text{Cs}_{0.2}\text{PbBr}_3$ follows the typical hot-injection method described by Protesescu et al. in their work on formamidinium nanocrystals: a precursor solution was prepared using Pb, FA and Cs acetates with dried oleic acid and dried octadecene; at 130 °C oleyl ammonium bromide dissolved in toluene was injected and after few seconds the nanocrystals were quenched in ice and purified.⁷ This simple synthesis allowed us to obtain luminescent cubic shaped nanocrystals (Figure 5.4) with average size around 15 nm. Both nanocrystal size and emission properties agree with the results reported previously for $\text{FA}_{0.8}\text{Cs}_{0.2}\text{PbBr}_3$.⁸



Figure 5.4: (A) Dispersion of $\text{FA}_{0.8}\text{Cs}_{0.2}\text{PbBr}_3$ NCs in toluene under UV lamp; (B) and (C) TEM images of $\text{FA}_{0.8}\text{Cs}_{0.2}\text{PbBr}_3$ NCs

In Fig. 5.5A are shown the XRD patterns of the $\text{FA}_{0.8}\text{Cs}_{0.2}\text{PbBr}_3$ sample together with FAPbBr_3 and CsPbBr_3 prepared with the same method as well as the reference pattern of the orthorhombic cell found for these halides (space group, Pnma). Fig. 5.5B reports a selected region of the patterns in order to discuss better and highlight the effects of cation composition on lattice size.

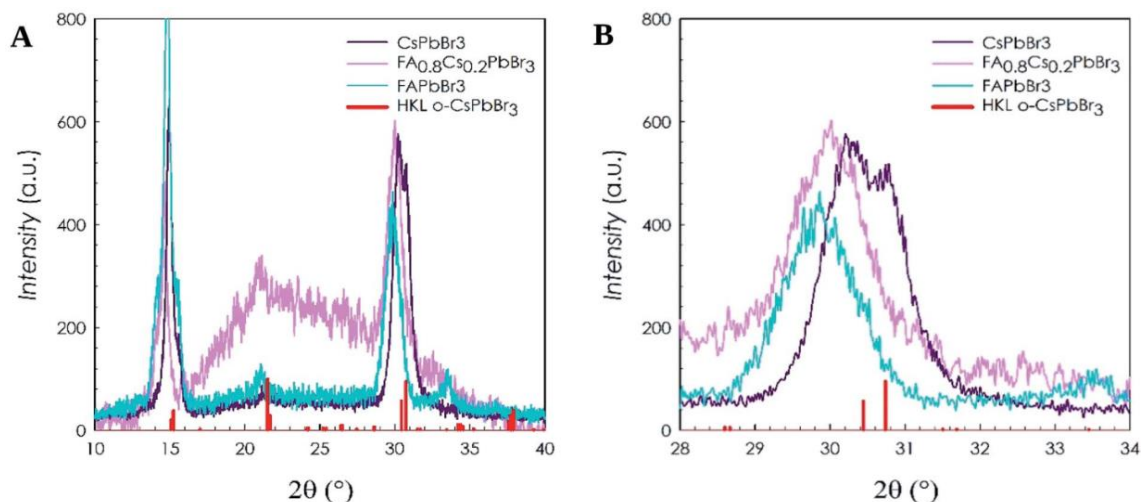


Figure 5.5: (A) XRD patterns of CsPbBr_3 , FAPbBr_3 and $\text{FA}_{0.8}\text{Cs}_{0.2}\text{PbBr}_3$ NCs; (B) same XRD patterns zoomed around 30°

First of all, all the samples are single phase without detectable impurities. Moreover, from Fig. 5.5B, it can be appreciated that the (040) and (202) reflections of the reference pattern of CsPbBr_3 (vertical red lines) are found in good agreement with the experimental data indicating the proper chemical composition of the sample. The same peaks are found at lower angle by replacing Cs with FA, indicating an increase of the cell size in agreement with the difference in the ionic radii between the two cations (r_{Cs} : 1.81 Å, r_{FA} : 2.79 Å). Finally, the mixed sample, *i.e.* $\text{FA}_{0.8}\text{Cs}_{0.2}\text{PbBr}_3$, is found at peak positions close to FAPbBr_3 but at slightly higher angle, in agreement with the 20% Cs-content. The optical properties of the $\text{FA}_{0.8}\text{Cs}_{0.2}\text{PbBr}_3$ sample, together with the two endmembers CsPbBr_3 and FAPbBr_3 , have been measured by means of PL spectroscopy.

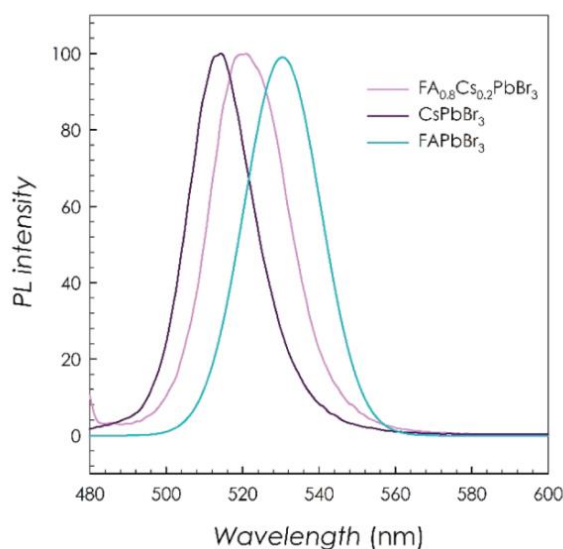


Figure 5.6: Normalized PL spectra of CsPbBr_3 , FAPbBr_3 and $\text{FA}_{0.8}\text{Cs}_{0.2}\text{PbBr}_3$ NCs

The results are reported in Figure 5.6. For all the three samples reported, the PL shows a single narrow peak (FWHM ca. 10 nm). The emission of pure CsPbBr₃ is centered at about 513 nm in agreement with previous literature data for an analogous crystal size.⁶⁻⁸ On the other hand, the replacement of Cs with FA red-shift the emission peak initially to 2.38 eV (FA_{0.8}Cs_{0.2}PbBr₃) and then to 2.33 eV (FAPbBr₃ sample).

Now that the properties of the FA_{0.8}Cs_{0.2}PbBr₃ starting sample have been properly characterized and compared to the data of the two end-members of the mixed compositions, we realized an anion-exchange reaction using lead halide precursors, with a simple dynamic solution process, a fast method to tune the optical properties in a post-synthetic reaction with the preservation of the crystal structure and morphology. The anion exchange reactions reported were conducted at room temperature in toluene by mixing a specific ratio of the desired lead halide salt. In particular, 0.113 mmol of PbX₂ were loaded in 4 mL of FA_{0.8}Cs_{0.2}PbBr₃ NCs toluene solution 28.3 mM, followed by 10 seconds of vigorous stirring which were found to be enough to appreciate a first color change suggesting the occurrence of anion exchange. After a minute the transparent solution was separated from the solid phase by centrifugation and analyzed.

Compared to most of the reported methods, this one is facile, fast and environmentally friendly.¹⁶⁻²⁴ The halide precursors do not need any solvent to be dissolved in, they can be separated by a simple filtration and, most relevant, the reaction can be carried out at room temperature and under ambient conditions. The products were characterized by means of X-ray diffraction, UV absorbance, photoluminescence and high resolution TEM.

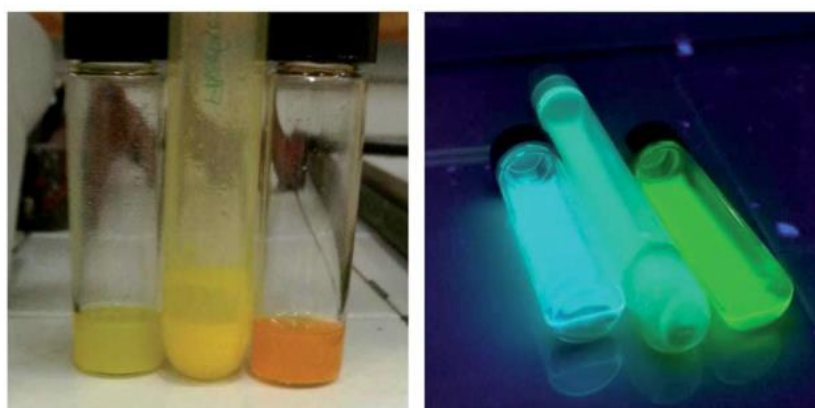


Figure 5.7: FA_{0.8}Cs_{0.2}Pb(Br/Cl)₃, FA_{0.8}Cs_{0.2}PbBr₃ and FA_{0.8}Cs_{0.2}Pb(Br/I)₃ NC's under daylight (left panel) and under UV light (right panel)

Fig. 5.7 shows the appearance of mixed Br/Cl, pure Br and mixed Br/I nanocrystals solutions under daylight and UV light illumination after 1 minute of exchange reaction. Already from this simple visual inspection, a blue-shift of $FA_{0.8}Cs_{0.2}PbBr_3$ NCs is observed after the exchange with Cl ions while a red-shift of the emission is clear for the sample exchanged with I anions.

The XRD patterns reported in Figure 5.8 for the $FA_{0.8}Cs_{0.2}PbBr_3$, $FA_{0.8}Cs_{0.2}Pb(Br/I)_3$ and $FA_{0.8}Cs_{0.2}Pb(Br/Cl)_3$ NCs display the typical reflections of the orthorhombic perovskite structure of $CsPbBr_3$. All the samples are single phase, anion exchange did not alter the crystal phase of the initial NCs.

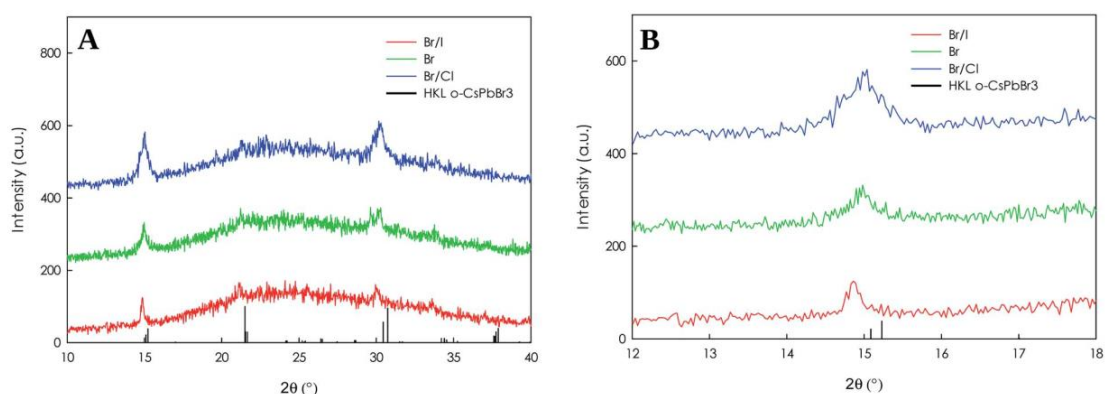


Figure 5.8: (A) XRD patterns of $FA_{0.8}Cs_{0.2}PbBr_3$, $FA_{0.8}Cs_{0.2}Pb(Br/I)_3$ and $FA_{0.8}Cs_{0.2}Pb(Br/Cl)_3$ NCs; (B) same XRD patterns zoomed around 15°

In Fig. 5.8B is reported a selected region to better analyze the effects of halide substitution: as expected the incorporation of I- cause an expansion of the cell and the peaks shift at lower angles, while upon the incorporation of Cl-, the cell shrunk, and the peaks shift to higher angles. The optical properties of mixed Br/Cl, pure Br and mixed Br/I nanocrystals have been measured by means of UV absorbance and PL spectroscopy. The results are reported in Fig. 5.9.

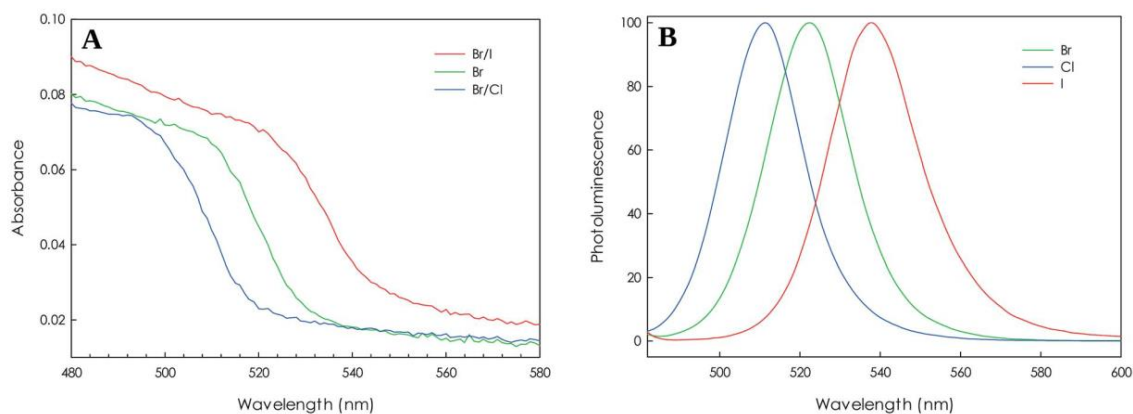


Figure 5.9: (A) UV spectra and (B) normalized PL spectra of $FA_{0.8}Cs_{0.2}PbBr_3$, $FA_{0.8}Cs_{0.2}Pb(Br/I)_3$ and $FA_{0.8}Cs_{0.2}Pb(Br/Cl)_3$ NCs

In the absorption spectra, with respect to Br-based NCs, the sample exchanged with Cl-ions shows a blue shift, while a red shift is observed for the iodide one: the composition tuning of the samples enabled the band gap to display absorption over the range of 500–540 nm for a very short time of exchange reaction. Along with the orthorhombic crystal structure, bright PL is retained, and the spectra are in good agreement with literature. For all the three samples reported the PL shows a single narrow peak (FWHM ca. 10 nm). The emission of pure Br is centered at about 523 nm; the replacement of Br with I red-shift the emission peak to 538 nm while the replacement with Cl blue-shift the peak to 511 nm.

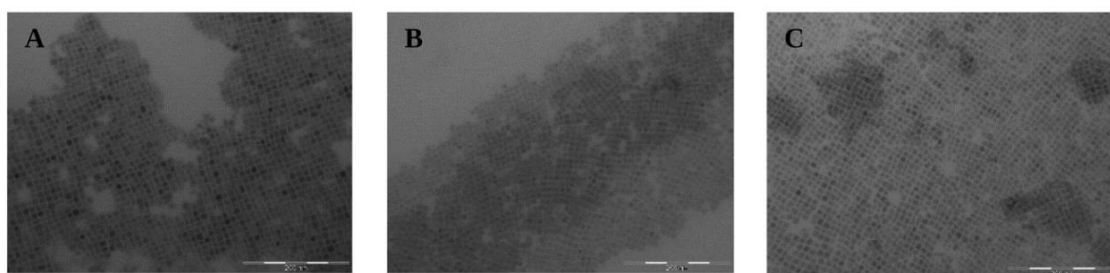


Figure 5.10: TEM images of (A) $FA_{0.8}Cs_{0.2}PbBr_3$, (B) $FA_{0.8}Cs_{0.2}Pb(Br/I)_3$ and (C) $FA_{0.8}Cs_{0.2}Pb(Br/Cl)_3$ NCs

From the TEM images reported in Figure 5.10, it is possible to observe that the morphology of the nanocrystals does not change, the cubic shape of the NC's whit bromide (Fig. 5.10A) is retained adding PbI_2 and $PbCl_2$ (Fig. 5.10B and C).

After assessing that this exchange methodology is effective in inducing an anion compositions modulation already for very short times (1-minute exchange), without changing the stoichiometry ratios between NCs and lead halide salts, the exchange was further investigated by increasing the reaction time to 5, 10, 15 and 30 minutes. The PL spectra of the samples for the corresponding reaction times and exchanged anions are

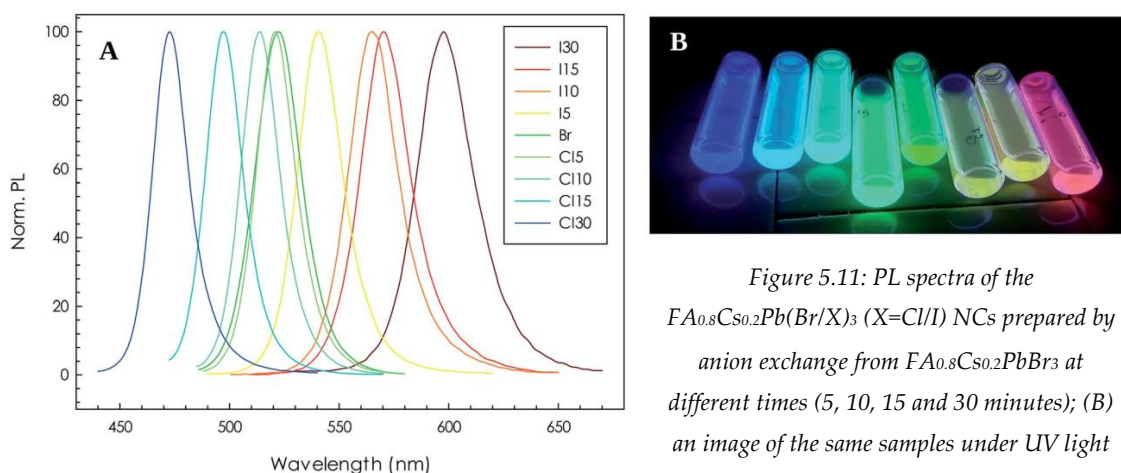


Figure 5.11: PL spectra of the $FA_{0.8}Cs_{0.2}Pb(Br/X)_3$ ($X=Cl/I$) NCs prepared by anion exchange from $FA_{0.8}Cs_{0.2}PbBr_3$ at different times (5, 10, 15 and 30 minutes); (B) an image of the same samples under UV light

reported in Fig. 5.11A, while Fig. 5.11B shows the appearance of the colloidal dispersions to which the PL spectra refer.

As can be appreciated, by simply increasing the stirring time the emission peaks significantly blue- and red-shift. Details about the PL peak maximum and FWHM are reported in Table 5.1.

Table 5.1 Emission properties and FWHM of the exchanged samples

Sample label	Emission (nm)	Emission (eV)	FWMH (nm)
Cl30	473.3	2.62	8.8
Cl15	497.7	2.49	9.1
Cl10	514.2	2.41	9.4
Cl5	521.4	2.38	9.6
Br	522.3	2.37	11.0
I5	541.5	2.29	10.9
I10	565.8	2.19	12.3
I15	571.3	2.17	12.7
I30	605.7	2.04	13.9

Overall, a 120 nm shift is achieved with this procedure and these mixing times. In addition, the peak widths remain quite narrow with a slight increase for the mixed Br/I samples by increasing the exchange reaction time which however is around 13 nm. An increase of the peak width for mixed Br/I samples has been previously observed but with FWHM reaching values around 45 nm for mixed Br/I samples.⁶ By comparing the actual PL emission values for the most exchanged samples with current literature for analogous crystal size, we may conclude that the maximum exchange level reached is around 1 : 2 Br : X (X = Cl, I).¹⁶ This result is in agreement with the data reported by Akkerman and co-workers where, however, they employed for the exchange, octadecyl ammonium halides (ODA-X) precursors which requires a not trivial separate reaction step and a 20- fold halide excess to achieve results analogous to those reported here.¹⁶ Still with reference to this last paper, the authors attempted as well the use of PbX₂ salts for the exchange but concluded that the reaction was too slow and required more than 1 day to achieve a significant exchange and for this reason was not investigated.¹⁶ The reasons for this significant disagreement between the data reported here and previous literature is not clear and might be due to the different quality of the reagents employed.

It is clear that a lot of space is left to further investigate the simple and effective anion exchange reaction proposed here, such as, for example, by further increasing the reaction time or by changing the molar ratio between the precursor NCs and the lead halide source, which in the present case was fixed to 1 : 1.

Conclusions

In summary, cubic shaped $\text{FA}_{0.8}\text{Cs}_{0.2}\text{PbBr}_3$ NCs were synthesized by solution reaction with the hot-injection method. These NCs were transformed in $\text{FA}_{0.8}\text{Cs}_{0.2}\text{Pb}(\text{Br}/\text{I})_3$ and $\text{FA}_{0.8}\text{Cs}_{0.2}\text{Pb}(\text{Br}/\text{Cl})_3$ by a fast and simple post-synthetic halide exchange reaction using PbI_2 and PbCl_2 directly in the form of powders in a 1 : 1 molar ration with respect to the NCs with the preservation of shape and crystal structure of the starting sample.

The innovative aspects of this work are the conditions of the halide exchange reactions reported: they were conducted in toluene at room temperature, without the necessity of N_2 atmosphere, with the simple use of lead halides thus not requiring the synthesis of complex halide precursors; in addition such precursors do not require the use of any solvent to be dissolved in and the exchanged nanocrystals can be separated by a simple filtration or centrifugation.

By using the present NCs : halide precursors molar ratio and extending the reaction time to 30 min the exchanged nanocrystals covered a large part of the visible region of the spectrum, with a fine tuning of the emission with reaction time and by preserving a high quality of the final crystals with very narrow FWHM.

References

1. <https://www.nrel.gov/pv/assets/pdfs/pv-efficiencies-07-17-2018.pdf>.
2. J. P. C. Baena, L. Steier, W. Tress, M. Saliba, S. Neutzner, T. Matsui, F. Giordano, T. J. Jacobsson, A. R. S. Kandada, S. M. Zakeeruddin, A. Petrozza, A. Abate, M. Khaja Nazeeruddin, M. Gratzel and A. Hagfeldt, *Energy Environ. Sci.*, 2015, 8, 2928.
3. Z. K. Tan, R. S. Moghaddam, M. L. Lai, P. Docampo, R. Higgler, F. Deschler, M. Price, A. Sadhanala, L. M. Pazos, D. Credgington, F. Hanusch, T. Bein, H. J. Snaith and R. H. Friend, *Nat. Nanotechnol.*, 2014, 9, 687.
4. M. Saliba, S. M. Wood, J. B. Patel, P. K. Nayak, J. Huang, J. A. Alexander-Webber, B. Wenger, S. D. Stranks, M. T. Horantner, J. Tse-Wei Wang, R. J. Nicholas, L. M. Herz, M. B. Johnston, S. M. Morris, H. J. Snaith and M. K. Riede, *Adv. Mater.*, 2016, 28, 923.
5. R. Dong, Y. Fang, J. Chae, J. Dai, Z. Xiao, Q. Dong, Y. Yuan, A. Centrone, X. C. Zeng and J. Huang, *Adv. Mater.*, 2015, 27, 1912.
6. L. Protesescu, S. Yakunin, M. I. Bodnarchuk, F. Krieg, R. Caputo, C. H. Hendon, R. X. Yang, A. Walsh and M. V. Kovalenko, *Nano Lett.*, 2015, 15, 3692.

7. L. Protesescu, S. Yakunin, M. I. Bodnarchuk, F. Bertolotti, N. Masciocchi, A. Guagliardi and M. V. Kovalenko, *J. Am. Chem. Soc.*, 2016, 138, 14202.
8. X. Zhang, H. Liu, W. Wang, J. Zhang, B. Xu, K. L. Karen, Y. Zheng, S. Liu, S. Chen, K. Wang and X. W. Sun, *Adv. Mater.*, 2017, 29, 1606405.
9. A. Amat, E. Mosconi, E. Ronc, C. Quarti, P. Umari, M. K. Nazeeruddin, M. Grätzel and F. De Angelis, *Nano Lett.*, 2014, 14, 3608.
10. M. Mittal, A. Jana, S. Sarkar, P. Mahadevan and S. Sapra, *J. Phys. Chem. Lett.*, 2016, 7, 3270.
11. W. Van der Stam, J. J. Geuchies, T. Altantzis, K. H. W. van den Bos, J. D. Meeldijk, S. Van Aert, S. Bals, D. Vanmaekelbergh and C. de Mello Donega, *J. Am. Chem. Soc.*, 2017, 139, 4087.
12. M. R. Linaburg, E. T. McClure, J. D. Majher and P. M. Woodward, *Chem. Mater.*, 2017, 29(8), 3507.
13. T. C. Jellicoe, J. M. Richter, H. F. J. Glass, M. Tabachnyk, R. Brady, S. E. Dutton, A. Rao, R. H. Friend, D. Credgington, N. C. Greenham and M. L. Böhm, *J. Am. Chem. Soc.*, 2016, 138, 2941.
14. Q. A. Akkerman, G. Rainò, M. V. Kovalenko and L. Manna, *Nat. Mater.*, 2018, 17, 394.
15. L. Wang, N. E. Williams, E. W. Malachosky, J. P. Otto, D. Hayes, R. E. Wood, P. Guyot-Sionnest and G. S. Engel, *ACS Nano*, 2017, 11, 2689.
16. Q. A. Akkerman, V. D'Innocenzo, S. Accornero, A. Scarpellini, A. Petrozza, M. Prato and L. Manna, *J. Am. Chem. Soc.*, 2015, 137(32), 10276.
17. G. Nedelcu, L. Protesescu, S. Yakunin, M. I. Bodnarchuk, M. J. Grotevent and M. V. Kovalenko, *Nano Lett.*, 2015, 15(8), 5635.
18. Y. Bekenstein, B. A. Koscher, S. W. Eaton, P. Yang and A. P. Alivisatos, *J. Am. Chem. Soc.*, 2015, 137(51), 16008.
19. S. E. Creutz, E. N. Crites, M. C. De Siena and D. R. Gamelin, *Chem. Mater.*, 2018, 30, 4887.
20. D. Parobek, Y. Dong, T. Qiao, D. Rossi and D. H. Son, *J. Am. Chem. Soc.*, 2017, 139(12), 4358.
21. M. Li, X. Zhang, K. Matras-Postolek, H.-S. Chen and P. Yang, *J. Mater. Chem. C*, 2018, 6, 5506–5513.
22. M. Li, X. Zhang, T. Dong, P. Wang, K. Matras-Postolek and P. Yang, *J. Phys. Chem. C*, 2018, 122, 28968–28976.

23. D. Zhang, Y. Yang, Y. Bekenstein, Y. Yu, N. A. Gibson, A. B. Wong, S. W. Eaton, N. Kornienko, Q. Kong, M. Lai, A. P. Alivisatos, S. R. Leone and P. Yang, *J. Am. Chem. Soc.*, 2016, 138(23), 7236.
24. D. M. Jang, K. Park, D. H. Kim, J. Park, F. Shojaei, H. S. Kang, J. P. Ahn, J. W. Lee and J. K. Song, *Nano Lett.*, 2015, 15, 5191– 5199.

CHAPTER 6.

ANION SUBSTITUTION IN 2D PEROVSKITES

This sixth experimental chapter of the thesis will focus on another type of hybrid perovskite. As previous chapters have amply illustrated, hybrid 3D perovskites are currently one of the most active fields of research owing to their enormous potential for photovoltaics; their performance has increased at an incredible rate, reaching power conversion efficiencies comparable to those of many established technologies. However, the commercial application of 3D hybrid perovskites is inhibited by their poor stability. Relative to 3D hybrid perovskites, low-dimensional 2D hybrid perovskites have demonstrated higher moisture and light stability, offering new approaches to stabilizing perovskite-based photovoltaic devices. Furthermore, 2D hybrid perovskites have versatile structures, enabling an even higher tunability of their optoelectronic properties through compositional engineering. In the paragraphs below, before introducing my very last work, I will discuss the state of art in 2D perovskites along with recent developments and the main limitations of 3D ones in terms of stability.

6.1 Stability issue and advantages of 2D perovskites

Despite the incredible increase in performance, the commercial potential of 3D perovskite solar cells has recently been questioned owing to their relatively poor stability under real operative conditions (89) (90) (91). Perovskite instability is largely attributable to moisture-induced degradation. Degradation affects the active layer itself as well as the interfacial layers of devices. 3D perovskites react with water, leading to collapse of the structure and to formation of either a 0D hydrated phase or to irreversible decomposition into the precursors. Local heating and UV light also accelerate perovskite decomposition. Other phenomena such as light-induced ion movement, ‘photo-instability’ or structural deformations not only affect the stability of the material but also alter device behaviour, contributing to the anomalous hysteresis observed in the

current–voltage characteristics, which is not yet clearly understood (92). Although degradation factors such as moisture, oxygen and heat can be circumvented by controlled encapsulation, instability upon light illumination is inevitable. Perovskite devices currently last for a few months outdoors, failing the 25-year warranty requirement for a marketable product (93). To overcome the stability issues, several approaches have been explored to reduce or retard device degradation. These include tailoring 3D perovskite materials through compositional engineering or by adding additives such as ionic liquids, reducing water infiltration into the active layer by device encapsulation with moisture-resistant layers or using alternative device architectures with more robust HTM and/or ETM layers (94) (95) (96).

Exploiting the superior stability of 2D perovskites has been recently proposed as an approach to solve the perovskite solar cells stability issue. 2D perovskites represent a particular class of low-dimensional perovskites, that can be obtained from the parent perovskite structure by slicing it along one of the crystallographic planes and inserting a long organic cation between, yielding a layered structure with corner-sharing octahedral inorganic quantum wells held together by Coulombic forces and separated by an organic barrier.

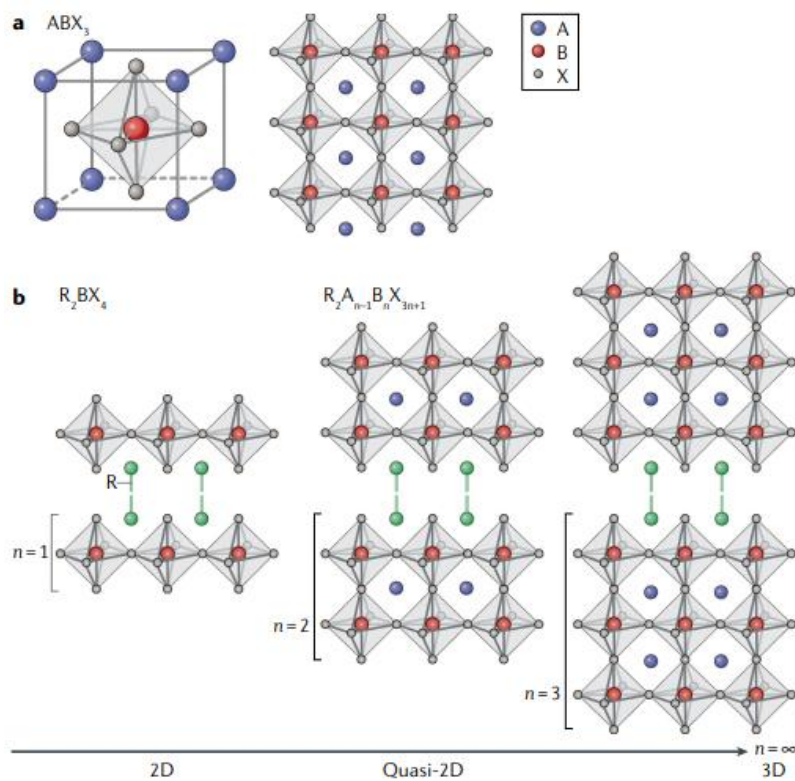


Figure 6.1 **a)** Illustration of the 3D hybrid perovskite structure ABX_3 ; **b)** Illustration of the structures of low-dimensional perovskites with different numbers of perovskite layers (n). The pure 2D perovskite ($n = 1$) has a R_2BX_4 structure, where R is a bulky organic cation.(111)

In practice, it is achieved by substitution of a small cation at the *A* position of AMX_3 by a bulky amine R^+ . If only a part of *A* is substituted, so-called multilayered perovskites can be obtained (97). The generic chemical formula of the multilayered perovskites with corner-sharing octahedra is $R_2(A)_{n-1}M_nX_{3n+1}$ (if *R* is a monobasic amine), where *n* represents the number of octahedral layers within one inorganic sheet (Fig

Organic cation	Molecular structure
$n\text{-BA}^+$	
iso-BA^+	
$C_6H_{13}NH_3^+$	
$FC_2H_4NH_3^+$	
AVA^+	
PMA^+	
PEA^+	
2-NMA^+	

Figure 6.2: Examples of organic cations commonly used to form 2D perovskites (111)

6.1) (98) (99). In the 2D hybrid halide perovskites the layered structure relaxes the limits on the cation dimensions imposed by the Goldschmidt tolerance factor paving the way to a wider choice of organic cations.

These organic cations act as insulating barriers that confine the charge carriers in two dimensions, but they also serve as dielectric moderators. The specific arrangement of alternating organic–inorganic layers generates a crystallographically ordered 2D multiple-quantum-well (MQW) electronic structure that forms stable excitons with large binding energies, able to interact more strongly with phonons, spins, and defects. Layered perovskites have been shown to be more structurally stable under non-ambient

conditions than the 3D ones, with maintaining the same phase longer under increasing pressure or decreasing temperature (100). 2D perovskites have narrower absorption owing to their larger bandgaps, which vary with the number of layers.

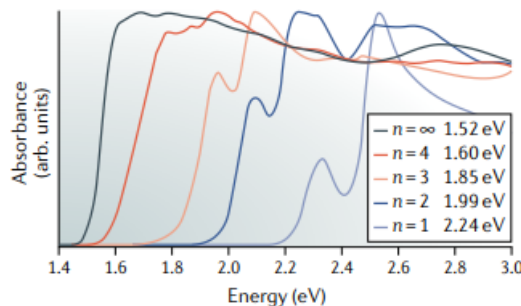


Figure 6.3: Absorption spectra of quasi-2D $BA_2MA_{n-1}Pb_nI_{3n+1}$ perovskite (111)

The structural flexibility of 2D perovskites can be used to modify the optoelectronic behaviour: when $n \leq 2$, the perovskites exhibit strong excitonic behaviour owing to quantum confinement effects, which leads to a high photoluminescence yield at room temperature and makes them suitable for light-emitting applications. However, $n \leq 2$ perovskites also have a narrow absorption and high exciton binding energy, which leads to a considerable loss in potential and makes them unsuitable for PVs. When $n \geq 3$, instead, the perovskites have a lower exciton binding energy, smaller bandgap and thus extended light absorption in the visible region, suggesting their suitability for sunlight-to-energy conversion.

6.2 BZA₂SnX₄

Exploring the Role of Halide Mixing in Lead-Free BZA₂SnX₄ (BZA=Benzylammonium) Two-Dimensional Hybrid Perovskites

Purpose and scope

The next generation of hybrid perovskites is characterized by reduced dimensionality. These derivatives expand the field of semiconducting hybrid perovskites and possess even higher tunability and excellent physical properties which make them suitable for optoelectronic properties.

In this view my very last work is focused on a two-dimensional system. Thus far, a great deal of attention has been focused on the solid solubility of mixed organic cations on the A-site, but very little has been studied about the halide mixing approach and still less have been said on the preparation and characterization of lead-free systems. Given this situation, we decided to explore the role of halide mixing on a tin-based 2D hybrid perovskite, preparing two novel compositions, BZA₂SnBr₄ and BZA₂SnCl₄, and the mixed composition BZA₂Sn(Br_xI_{1-x})₄ (0 ≤ x ≤ 1) confirming the existence of a wide solid solubility between the two end-members.



Figure 6.4: Some of the BZA₂SnI_(4-x)Br_x samples synthesized by ball-milling

We introduce the high energy ball-milling as a new approach for the synthesis of the mixed 2D system BZA₂SnI_(4-x)Br_x which is very interesting being simple, green and scalable. All the stoichiometric samples (BZA₂SnX₄, X=Cl, Br and I) were grown also as single crystals for a more rigorous determination of the crystal structure.

Introduction

The field of organic-inorganic hybrid halide perovskites has recently moved towards two-dimensional (2D) systems, which provide an impressive space for material engineering and tailoring of desired functions with concomitant excellent photo-physical properties.¹⁻⁶ Among the several classes of 2D perovskites, recently and deeply reviewed in ref. 1, the one comprising (100)-oriented 2D materials is by far the most abundant and explored. They consist of alternating organic-inorganic layers with corner-sharing $[MX_6]^4$ units and organic spacers between them. They can form Ruddlesden-Popper (RP) and Dion-Jacobson phases depending on the nature of the A-site organic group(s).¹ Further, among the RP phases, the $n=1$ members, with general formula A_2PbX_4 (A=monovalent organic cation; X=halide) have received significant attention for their optoelectronic properties and material robustness.^{1,7-11} However, the plethora of organic spacers and the extension of the homologous series ($n>1$), allow for a huge variety of materials to be engineered for tailored applications, including the solid solubility of mixed organic cations on the A-site of the 2D perovskite.¹ On the opposite, the exploration of halide mixing approach on 2D hybrid perovskites has been very limited to date, with few examples related to the optimization of quantum yield of white-light emission.^{1,12,13} This is quite surprising, considering the success of this approach on 3D materials and 0D nanocrystals.^{7,14-19} Finally, another poorly explored area of research on 2D hybrid perovskites is the preparation and characterization of lead-free systems. The few examples available confirm the known (on 3D perovskites) tunability of bandgap and optical properties induced by tin or germanium replacement.^{9,20}

Based on the above considerations, we explored the role of halide mixing on a tin-based 2D hybrid perovskite, namely BZA_2SnX_4 (BZA=benzylammonium; X=Cl, Br and I). In particular, we afforded the preparation of the novel Br/I mixed system in order to define the possible existence and extension of such solid solution, as well as the preparation of BZA_2SnCl_4 . We highlight that among the compound of this series, only BZA_2SnI_4 is actually known in the current literature.⁹ Mao and co-workers, in ref. 9, explored the synthesis of the $BZA_2Pb_{1-x}Sn_xI_4$ solid solution, showing a significant reduction of the band-gap by progressively replacing Sn for Pb, with an anomalous (non Vegard) trend with metal mixing.⁹ In the same work, the crystal and electronic structures were provided, showing, for example, that the inorganic layers in the compound adopt a staggered motif.⁹ Due to the peculiar structural properties of 2D halide perovskite, it is of significant interest to investigate the evolution of the crystal and optical properties as a function of the halide substitution, being the two BZA groups coordinating two adjacent halides.

Results and discussion



Figure 6.5: BZA_2SnBr_4 (yellow) and BZA_2SnI_4 (dark violet) samples, synthesized as single-crystals

were grown as single crystals for a more rigorous determination of their crystal structure.

The crystal structure of BZA_2SnI_4 was re-evaluated, and agrees with the previous determination provided in ref. 9, showing an orthorhombic unit cell (space group, s.g., $Pbca$) with lattice parameters of $a=9.1105(1)$ Å, $b=8.6776(1)$ Å, and $c=28.754(6)$ Å.⁹ The crystal structures of the novel compounds BZA_2SnBr_4 and BZA_2SnCl_4 were as well determined, and resulted to be both orthorhombic (s.g. $Cmc2_1$), with lattice parameters $a=33.2806(1)$ Å, $b=8.1046(4)$ Å, and $c=8.1036(4)$ Å for BZA_2SnBr_4 , and $a=33.505(3)$ Å, $b=7.7784(6)$ Å, and $c=7.7678(5)$ Å for BZA_2SnCl_4 , respectively. Although the $Pbca$ and $Cmc2_1$ space groups have different settings (mainly due to the different Bravais lattice), we use that of BZA_2SnI_4 for sake of clarity and data representation taking into account that $aI = cBr, Cl$, $bI = bBr, Cl$, and $cI = aBr, Cl$ (the subscripts I, Br, and Cl indicate the

Samples of the $BZA_2Sn(Br_xI_{1-x})_4$ series have been prepared in form of polycrystalline powders by high energy ball-milling. Such approach, very scarcely applied to 2D hybrid perovskites, is becoming of wider interest because it is a green, scalable, and can easily allow the synthesis of hybrid perovskites as well as all-inorganic perovskites for photovoltaics. Besides, stoichiometric BZA_2SnX_4 compounds ($X=Cl, Br$, and I)

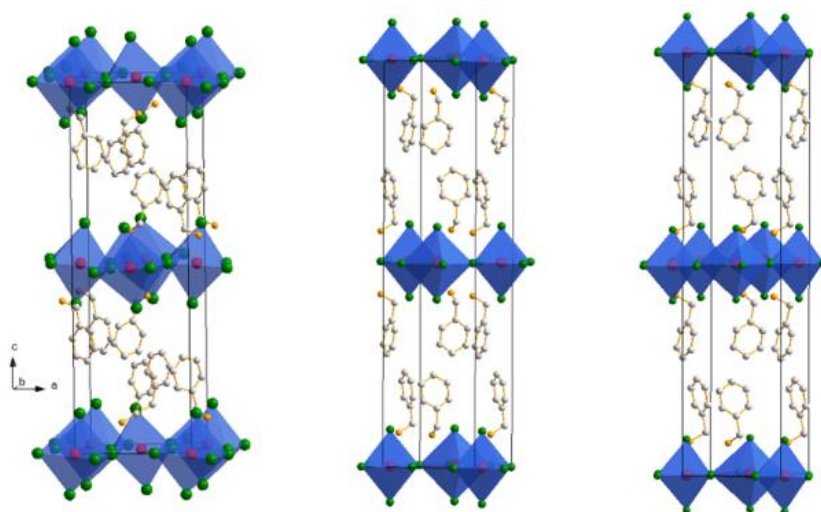


Figure 6.6: Room temperature sketch as determined from single crystal diffraction for (a) BZA_2SnI_4 , (b) BZA_2SnBr_4 , and (c) BZA_2SnCl_4 . Sn atoms are depicted in red, halide in green, C in white and N in yellow.

halogen of the different compounds). A sketch of the three structures is reported in Figure 6.6.

As it can be appreciated from the lattice parameters data reported, the change from iodide to bromide induces an expansion of the *c*-axis of the crystal structure, passing from about 28 Å in BZA₂SnI₄ to about 33 Å in BZA₂SnBr₄, and a reduction of the in-plane parameters (due to the relative ion size of Br⁻ and I⁻). Such elongated structure is also found for the chloride member, with even a slight further expansion of the *c*-axis with respect to BZA₂SnBr₄. The out-of-plane elongation is essentially due to the change in the staggering of the two benzylammonium cations which move apart the two halides passing from an interlayer halide-halide distance of 9.31 Å (I-I) to 11.44 Å (Br-Br), and 11.76 Å (Cl-Cl). The tilt of the organic molecule with respect to the long cell axis raises from ~9° for BZA₂SnBr₄ and BZA₂SnCl₄, up to 17.4° for BZA₂SnI₄, thus facilitating the staggering of the organic cations with consequence shrinking of the long cell axis. The protonated ammonium ion connects to the apical halides through hydrogen bonding showing a significant reduction of the donor-acceptor distance passing from about 3.6 Å for BZA₂SnI₄ to about 3.5 Å for BZA₂SnBr₄ down to 3.2 Å for BZA₂SnCl₄. The role of hydrogen bonding in driving electronic and structural properties of hybrid perovskites is well known and discussed in many recent papers²¹⁻²⁵.

The distortion inside the inorganic framework was evaluated by looking at the Sn-X-Sn angle and the Sn-X bond distances. For BZA₂SnI₄ the Sn-I-Sn angle is 160.6°, in agreement with previous determinations, while the distortion index of the bond length has been found to be 0.0049, which compares to 152° and 0.0039 for BZA₂SnBr₄. As for BZA₂SnCl₄, the equatorial site split leads to an alternation of wide (154°) and narrow (144°) Sn-X-Sn angles, indicating a greater distortion between the octahedra moving towards the smaller halide.^{9,26} Interestingly, the octahedral distances evolve significantly with the nature of the halide: the apical bond length contracts moving from I (3.16 Å) through Br (2.98 Å) and Cl (2.82 Å), in keeping with the halide ionic radii. A similar behaviour is observed for the average of equatorial bonds, which decreases from 3.192(10) Å for I to 2.964(14) Å for Br and 2.85(16) Å for Cl. Therefore, the octahedra become more distorted moving to Cl. A possible Cl-site splitting is discussed in the Experimental methods.

The in-plane lattice parameters follow, on the other hand, a trend reflecting the different size of the halide, with *a* and *b* axes reducing progressively passing from BZA₂SnI₄ to BZA₂SnCl₄. The orthorhombic distortion of the unit cell is relevant for the iodide-containing perovskite while it becomes significantly smaller for the other two compositions.

After having elucidated the specific crystal structure of line compounds, providing the information on the novel BZA_2SnBr_4 and BZA_2SnCl_4 materials, we afforded the investigation of the polycrystalline samples of the possible $BZA_2Sn(Br_xI_{1-x})_4$ solid solution. The synthesized samples, as obtained from the ball-milling synthesis, show a progressive change of colour from brilliant yellow of BZA_2SnBr_4 to dark violet of BZA_2SnI_4 . Their powder X-ray diffraction (XRD) patterns are shown in Figure 6.7.

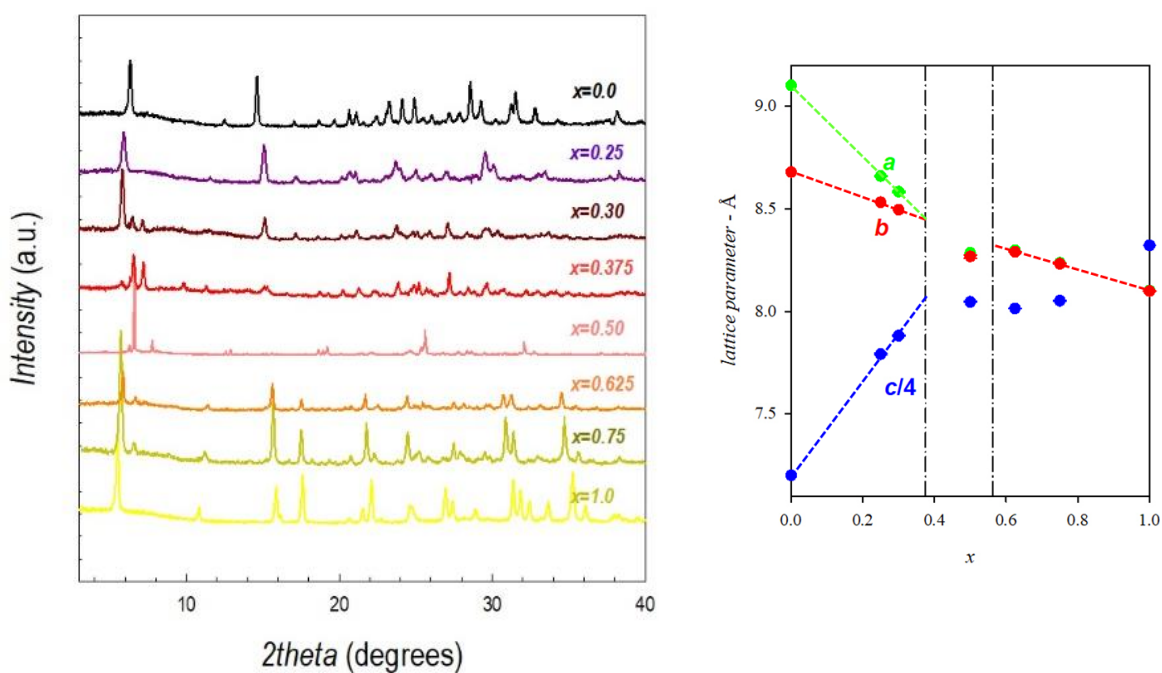


Figure 6.7: a) room temperature XRD patterns of the samples of the $BZA_2Sn(Br_xI_{1-x})_4$ system; b) lattice parameters of the samples reported in Figure 2b keeping the setting of the I-member for simplicity.

From the analysis of the diffraction patterns of Figure 6.7a, we found that single-phase materials do not exist in the complete compositional range of Br/I halide mixing. In the $\sim 0.40 < x < \sim 0.55$ compositional region we observed peaks pertaining to a new phase that will be discussed in the next paragraph.

The XRD patterns of the single-phase samples of the $\text{BZA}_2\text{Sn}(\text{Br}_x\text{I}_{1-x})_4$ solid solution, shown in the Figure 6.8, were refined in order to determine the lattice parameters reported in Figure 6.7b.

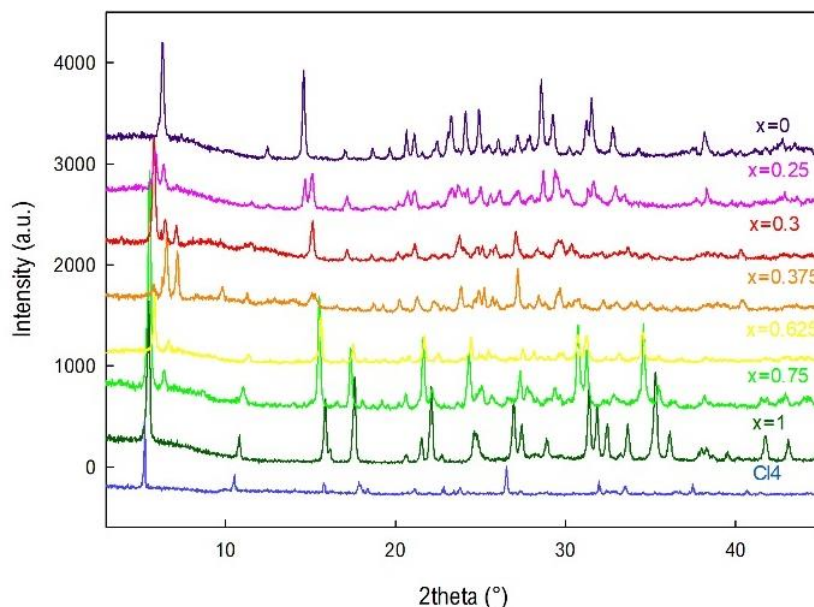


Figure 6.8: XRD patterns without the sample $x=0.5$

Looking at the a , b parameters, we note a progressive linear contraction passing from BZA_2SnI_4 to $\text{BZA}_2\text{SnBr}_4$, accompanied by a reduction of their relative difference. Let us remember that in $\text{BZA}_2\text{SnBr}_4$ we observed $a=8.1046(4)$ Å and $b=8.1036(4)$ Å, *i.e.* an extremely small orthorhombic distortion. Below $x=0.625$, the two parameters have always a very small orthorhombic distortion, which starts to be significant from $x=0.3$, *i.e.* in the iodide-rich samples. This behaviour correlates to the reduced octahedral distortion of $\text{BZA}_2\text{SnBr}_4$ (see above) which clearly manifests already for mixed halide compositions of the Br-rich side. Also, the linear dependence of lattice parameters with x helped us to estimate the compositional region where the 2D perovskite is likely not to occur, indicated by vertical dashed lines in Figure 6.7b.

An interesting behaviour is shown by the trend of c -axis. As we reported above, there is an elongation of nearly 5 Å when moving from iodide to bromide, which is due to the different orientation of the benzylammonium cations between the inorganic layers. The expansion of the c -axis from BZA_2SnI_4 up to $x=0.3$ is linear (see Figure 6.7b) and becomes flatter in the Br-rich side of the solid solution, until the final value of 33.2806(1) Å is attained for $\text{BZA}_2\text{SnBr}_4$. There are several factors that play a role when moving from $x=0$ to $x=1$, such as the change of the staggering mode of organic cations,

the distortion of the octahedra and the hydrogen bonding between the halide and the hydrogen of the amine group. The interplay of such effects, clearly more effective in the Br-rich mixed compositions, defines the trend of the c -axis. Interestingly, an anomalous trend in the lattice parameters has been very recently observed in the $\text{BZA}_2\text{Pb}(\text{Br}_x\text{Cl}_{1-x})_4$ system.²⁸

Thermal properties of the $\text{BZA}_2\text{Sn}(\text{Br}_x\text{I}_{1-x})_4$ solid solution have been determined by thermogravimetry (TGA) and Differential Scanning Calorimetry (DSC). TGA curves show a general stability of the phases up to about 150°C after that a significant weight loss is found with an apparent slightly greater temperature stability for $\text{BZA}_2\text{SnBr}_4$. (Figure 6.9a) DSC measurements in the $-80^\circ\text{C} < T < 100^\circ\text{C}$ interval do not show any thermal event suggesting phase transition in the system (Figure 6.9b).

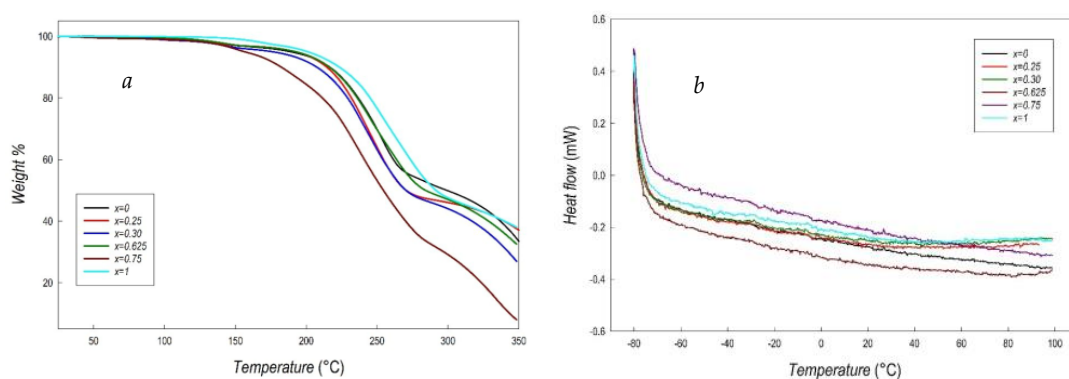


Figure 6.9: a) TGA traces for the $\text{BZA}_2\text{Sn}(\text{Br}_x\text{I}_{1-x})_4$ solid solution as a function of x in the range from RT to 350°C; b) DSC traces for the $\text{BZA}_2\text{Sn}(\text{Br}_x\text{I}_{1-x})_4$ solid solution as a function of x in the range from -80°C to 100°C

The samples are fully stable after six months of storage under inert atmosphere in the glovebox, as confirmed by UV-Vis spectra and diffraction measurements. On the other hand, we performed an aging test on the BZA_2SnI_4 sample (selected as representative) by exposing it to laboratory air (RH around 40%) and collecting UV-Vis spectra and diffraction patterns after 1, 5 and 10 days (Figure 6.10a and 6.10c). The same test has been performed on the lead-based analogue, i.e. BZA_2PbI_4 . (Figure 6.10b and 6.10d)

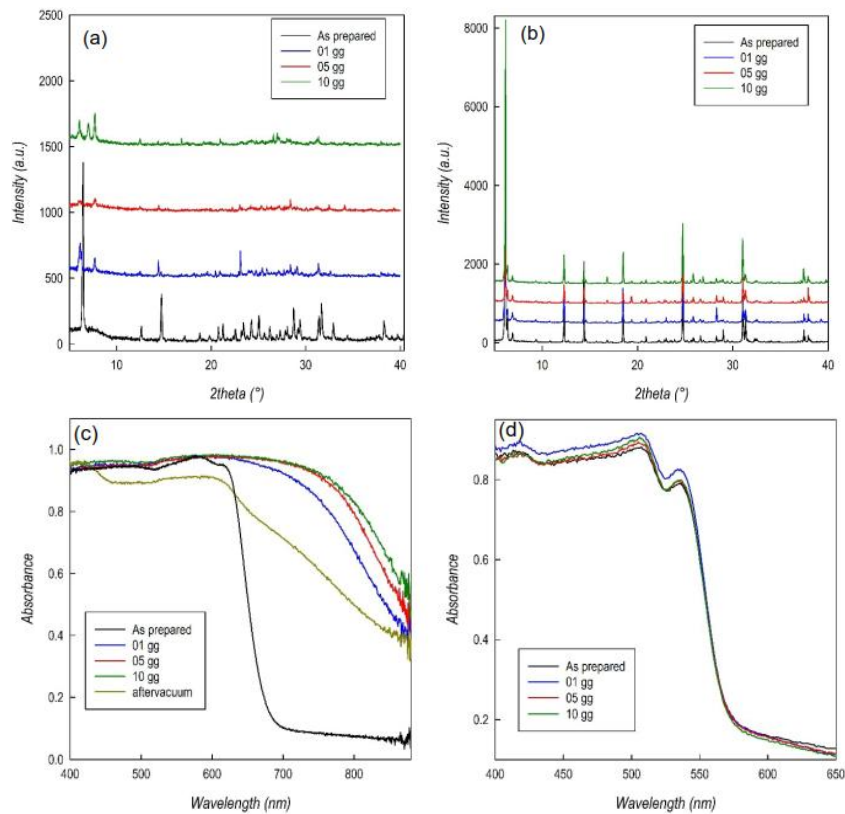


Figure 6.10: XRD patterns of BZA₂SnI₄ (a) and BZA₂PbI₄ (b) as a function of time under laboratory-air exposure and UV-Vis spectra of BZA₂SnI₄ (c) and BZA₂PbI₄ (d) as a function of time under laboratory-air exposure.

The BZA₂SnI₄ sample shows a clear change of diffraction as well as optical properties under air already after 24 hours. It is worth noticing that the absorbance significantly red-shifts during aging and that a vacuum treatment after 10 days of air-exposure partially relieves the initial situation suggesting a certain level of reversibility of the air-induced effects. On the other hand, BZA₂PbI₄ sample is fully stable up to 10 days, indicating a positive effect of a large organic cation towards moisture stability.

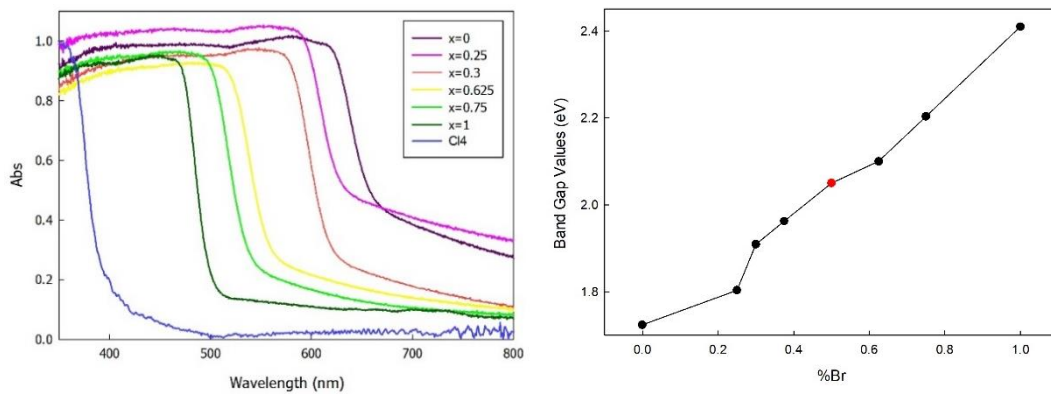


Figure 6.11: a) Absorption spectra of the BZA₂Sn(Br_xI_{1-x})₄ system; b) trend of the bandgap as a function of x

The optical properties of the samples have been investigated by absorption and steady-state photoluminescence (PL) spectroscopies. The sample with $x=0.375$ has been excluded because of the large presence of the 1D phase, which could have distorted some results. Figure 6.11a reports the absorption spectra of the single-phase mixed samples of the $\text{BZA}_2\text{Sn}(\text{Br}_x\text{I}_{1-x})_4$ system together with the $\text{BZA}_2\text{SnCl}_4$, while Figure 6.11b shows the trend of the bandgap determined from the Tauc plots of the spectra for the single-phase samples of the solid solution.

A clear blue-shift is observed in the spectra by moving from BZA_2SnI_4 to $\text{BZA}_2\text{SnBr}_4$, with a linear increase of the band-gap from 1.74 eV to 2.41 eV.^{9,28} The analogous lead-based 2D hybrid perovskites, namely BZA_2PbI_4 to $\text{BZA}_2\text{PbBr}_4$, exhibit band-gaps of about 2.20 eV and 2.90 eV, respectively, thus confirming the usual ~0.6-0.7 eV difference between Pb and Sn systems found in 3D perovskites.²⁹⁻³² This is quite interesting considering the different local environment of 3D and 2D hybrid perovskites.

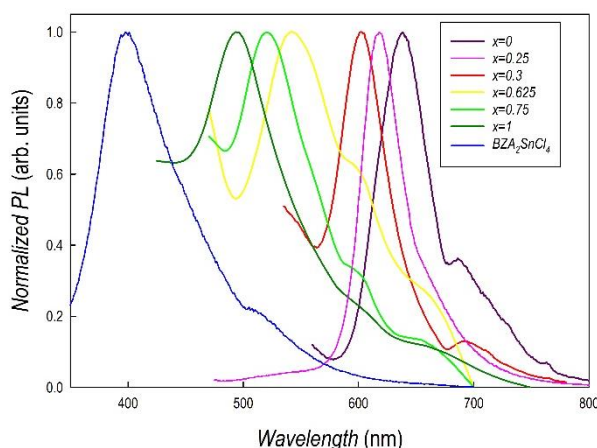


Figure 6.12: a) Normalized photoluminescence spectra of the $\text{BZA}_2\text{Sn}(\text{Br}_x\text{I}_{1-x})_4$ system; b) Emission properties and FWHM of the exchanged samples

However, DFT calculations performed on similar systems revealed that, in general, the valence band maximum (VBM) is dominated by metal s -orbitals and halide p -orbitals, while the conduction band minimum (CBM) is dominated by empty metal p -orbitals. This indicates that, qualitatively, the electronic structure is similar to that of the 3D perovskites, which agrees with the “rigid” shift of about 0.5 eV observed when passing from Pb to Sn systems. With these arguments, the fact

that the bandgap of 1D $\text{BZA}_3\text{Sn}(\text{I}_{0.5}\text{Br}_{0.5})_5$ perovskite (2.05 eV) well fits on the trend of Figure 5b (see red solid dot), suggests that this is true for even lower dimensionality systems. The bandgap of $\text{BZA}_2\text{PbCl}_4$ is found at about 3.04 eV which again is in line with the expected variations moving from bromide to chloride.³⁰

Figure 6.12a reports the normalized steady-state PL spectra of the single-phase mixed samples of the $\text{BZA}_2\text{Sn}(\text{Br}_x\text{I}_{1-x})_4$ system. As can be appreciated, by simply adjusting the halide content, the emission peaks significantly blue shift covering almost the entire spectra. Details about the PL peak maximum and FWHM are reported in Figure 6.12b.

Sample label	Emission (nm)	Emission (eV)	FWHM (nm)
x=0	638	1.94	37
x=0.25	634	1.96	37
x=0.3	602	2.06	34
x=0.625	541	2.29	43
x=0.75	521	2.38	38
x=1	493	2.52	40

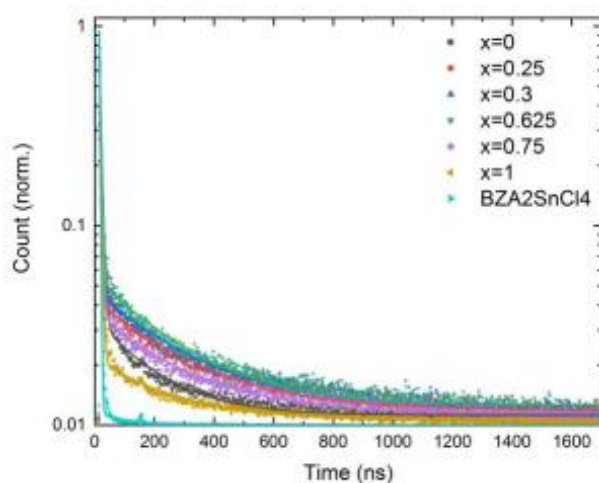


Figure 6.13: PL decay at the peak emission upon excitation at 375 nm

Overall, a nearly 300 nm shift is achieved from I to Cl. For all the samples the PL show a very narrow peak ($37 < \text{FWHM} < 43$ nm), which is an incredible result for Sn-based 2D perovskites.

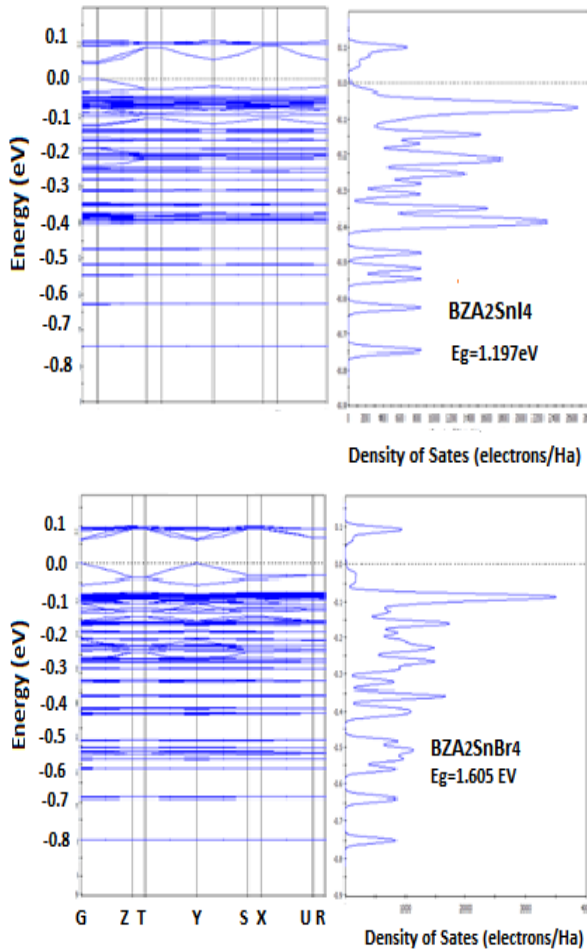
Figure 6.13 reports the PL decay upon excitation at 375 nm. The decay shows only marginal difference among the samples, with a first fast component followed by a slower decay which is completed in the first microsecond time window. The fast component can be assigned to rapid electron-hole recombination while the longer living tail to trap-mediated recombination. Notably, for the Cl sample only a fast decay is observed while the second component is vanished out.

Further insight into the electronic structure of the present samples has been obtained by DFT calculations. For the structural optimization, the structure determined experimentally was used as the starting geometry. The theoretical ground-state structure was obtained from this, by full geometry optimization, that is, the atom positions and cell parameters were fully relaxed. Geometry optimization of BZA_2SnX_4 ($X=\text{I}$, Br , and Cl) in orthorhombic structure ($Pbca$ (61) for $X=\text{I}$, $Cmc2_1$ (36) for $X=\text{Br}$, Cl) was performed using the DMol3 program in the spin unrestricted approach. The calculated structural parameters and related reference data are shown in Table 6.1 where the simulated parameters of BZA_2SnX_4 correspond to experimental values with an error range of 0.08-5.5 %, which confirms the validity of our calculation.

Table 6.1: Optimized lattice parameters for BZA_2SnX_4 ($X=Cl, Br, \text{ and } I$) with experimental values

Systems	$a(\text{\AA})$	$b(\text{\AA})$	$c(\text{\AA})$
BZA₂SnI₄			
Theory	9.317	8.867	30.3618
Exp.	9.1105(14)	8.6776(13)	28.75(4)
Error %	2.26	2.18	5.59
BZA₂SnBr₄			
Theory	33.979	8.111	8.0226
Exp.	33.2806(15)	8.1046(4)	8.1036(4)
Error %	2.09	0.08	0.99
BZA₂SnCl₄			
Theory	34.68	8.1139	7.873
Exp.	33.505	7.7784	7.7678
Error %	3.4	4.1	1.33

The calculated electronic band structure of BZA_2SnX_4 ($X=I, Br, \text{ and } Cl$) along high symmetry points of the first Brillouin zone plotted in Figure 6.14. Where the labelled k-points are present as $\Gamma(0, 0, 0)$, $Z(0, 0, 0.5)$, $T(-0.5, 0, 0.5)$, $Y(-0.5, 0, 0)$, $S(-0.5, 0.5, 0)$, $X(0, 0.5, 0)$, $U(0, 0.5, 0.5)$, and $R(-0.5, 0.5, 0.5)$. The maximum of the valence band (VBM) and



the minimum of the conduction band (CBM) occur at $\Gamma(0, 0, 0)$ for BZA_2SnI_4 and at $Y(-0.5, 0, 0)$ for BZA_2SnBr_4 and BZA_2SnCl_4 , points in the Brillouin zone. All of the BZA_2SnX_4 ($X=I, Br, \text{ and } Cl$) structures were found to have direct band gaps which are consistent with the observed steepness of the absorption edges in the spectra. The calculated energy gaps are 1.197 eV, 1.605 eV, and 2.503 eV which are underestimated compared to the experimental value of 1.7 eV, 2.4 eV, and 3.04 eV. This value of the energy gap demonstrates that the material belongs to the semiconductor family. When we go to from Cl to I, the band gap decreases due to increasing electronic charge density and lattice constants. Therefore, from Cl to I,

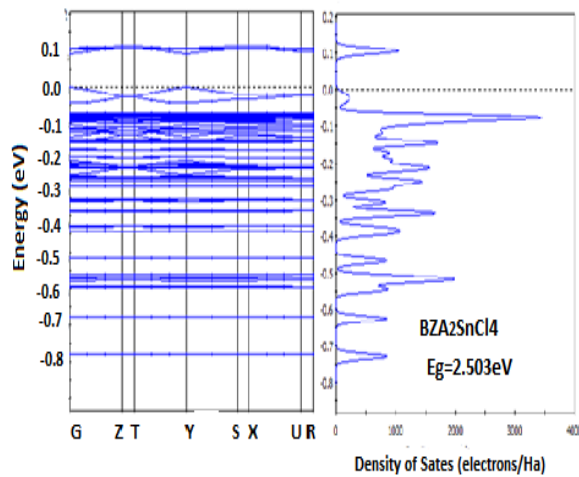


Figure 6.14: DFT calculations of electronic band structures for BZA_2SnX_4 ($X=I, Br, \text{ and } Cl$)

number of atom and number of electrons in the crystals increases. As a result, the valence band shifts up to Fermi level due to the occupation of electrons in the position near Fermi level, result in a decrease in the energy gap between valance and conduction bands. Such an underestimation of the calculated band gaps is an intrinsic property of the ab initio method and is related to the DFT limitations, namely, not considering the discontinuity in the exchange-correlation potential [x]. Our obtained band gap value for BZA_2SnI_4 (1.197eV) is good agreement with other DFT result (1.33 eV) by Mao et al⁹.

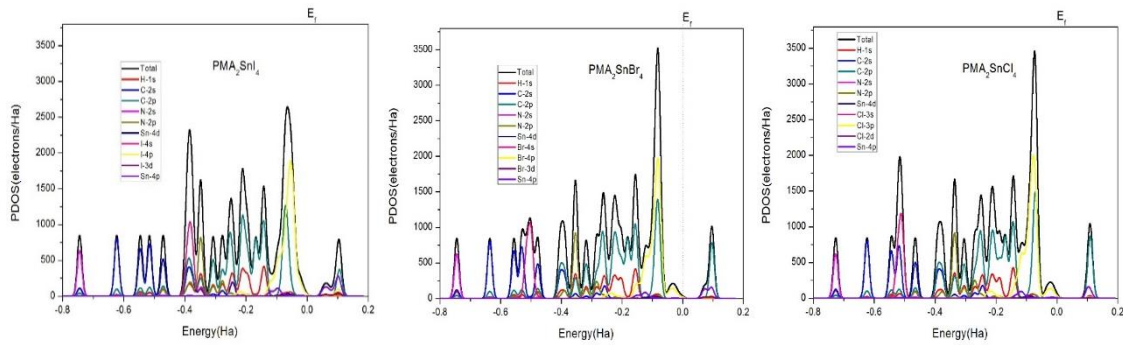


Figure 6.15: DFT calculations of total and partial density of states (PDOS) for BZA_2SnX_4 ($X=I, Br, \text{ and } Cl$)

The total electronic density of states (TDOS) and partial density of states (PDOS) using the calculated lattice constants of BZA_2SnX_4 ($X=I, Br, \text{ and } Cl$) are given in Figure 6.15. The properties observed in the PDOS spectra are similar to each others. From the PDOS of BZA_2SnX_4 , it is possible to see the distribution of various electronic states in the valence band and the conduction band. In the lower valance band region, s-states of N and C are dominant. The s-states of H and p-states of N can overlap with the p-states of C in the energy range between -0.45 Ha and -0.3 Ha and can form covalent bonds. The d- and p-states for Sn and C atoms, respectively, are dominantly contributing to the valence band in the range between -0.3 Ha and -0.22 Ha. Both s- and p-states of H and Sn atoms also contribute to the VB. The p-states of C and s-states of H are distributed energetically in the same range and thus they can effectively overlap and form very

strong covalent bonds. Although the p-state of I/Br/Cl is energetically degenerate with that of Sn, in the whole valence band, the spatial separation of these two atoms makes no covalent bonding between Sn and I/Br/Cl. The d-state of Sn is well localized which leads to ionic bonding between Sn and I/Br/Cl. Below to Fermi level, VBM is dominated by I/Br/Cl p-orbitals and less C-p orbitals. The conduction bands are derived largely from the C p and Sn p-states. Moreover, to Cl from I, the hybridism interaction between C and Sn atoms increased because of the smaller electronegativity of I, which shifts the C p states to high energy, as can be seen from Figure 6.15. This result is in agreement with the the band gap increase from I to Cl and may be attributed to the hybridization of C p and Sn p-states near the Fermi level. Notably, it is found that C p-states have a relatively high value, which indicates that the electron transit directly from the Sn p to C p-states. This result shows a high mobility and low resistivity in BZA_2SnX_4 .

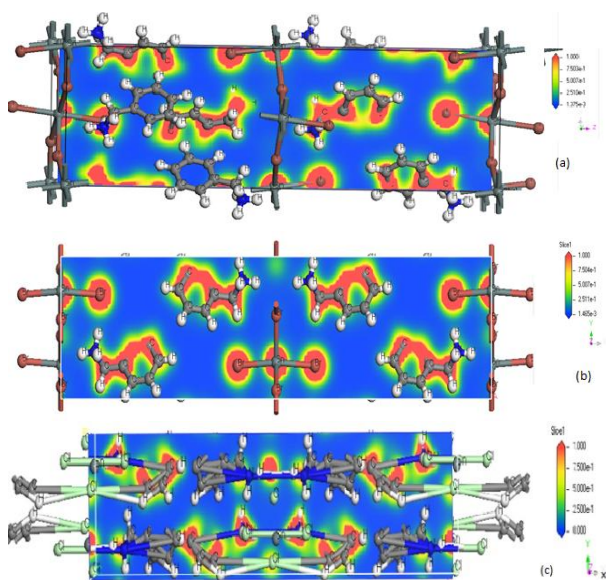


Figure 6.16: Calculated charge density for BZA_2SnX_4 ($X=I, Br, \text{ and } Cl$) in $[110]$ plane

To further improve the understanding of the bonding interactions, we turned our attention to charge density analyses. From the illustration in Figure 6.16, it is clear that C, H, and N atoms in the organic linker form an BZA_2SnX_4 ($X=I, Br, \text{ and } Cl$) structural subunits. As a result, the C-C, C-H, and C-N bonding interactions are dominantly covalent in character. Moreover, there is a substantial charge density distributed between C atoms, and between C and H and N atoms. This shows the presence of covalent bonding. From Figure 6.16, it can be

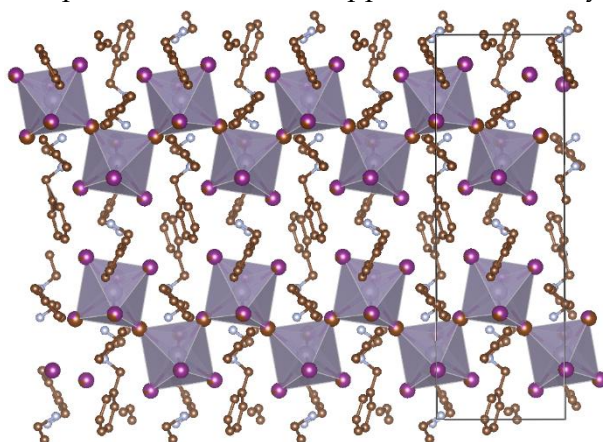
seen that the charges are spherically distributed at the X and Sn sites, which is characteristic of systems having ionic interactions. Additionally, there is no noticeable charge density distributed between I/Br and Sn atoms which clearly demonstrate the presence of ionic bonding.

Concerning the hydrogen bonding, the three H atoms of the $-NH_3^+$ group in BZA are attracted toward the surrounding halogen atoms of the perovskite cage in BZA_2SnX_4 , forming at least three $X \cdots H(-N)$ intermolecular contacts. This is evidence of the occurrence of intermolecular contacts; two of these contacts are short and equivalent, with $d(X-H(-N)) = 1.036 \text{ \AA}$, 1.038 \AA and 1.051 \AA . These are hydrogen bonds since each of

these three intermolecular distances is significantly smaller than the sum of the van der Waals radii of the Sn and H atoms, 3.62 Å (Sn = 2.42 Å and H = 1.20 Å).³³⁻³⁵ This result indicates that there is big penetration between the non-covalently bound X and H atoms involved in hydrogen bond formation in this system, making the entire structure compact and stable.^{34,35} The H atoms of the -CH₃ group of the BZA also form intermolecular contacts with the X atoms of the perovskite cage. C-H bond lengths are 1.093 Å, 1.097 Å and 1.091 Å for BZA₂SnX₄. Each of these contact distances is slightly smaller than the sum of the van der Waals radii of the H (1.2 Å) and X (2.04, 1.86 and 1.82 Å) atoms, 3.24 Å. This means that the hydrogen bonds formed between the H atoms of the -CH₃ group and the Sn-atoms of the perovskite cage may have a relevance. The X···H(-N) hydrogen bonds are stronger than the X···H(-C) hydrogen bonds in BZA₂SnX₄ because of shorter bond lengths. However, from the angle of approach for hydrogen bond formation, it can be concluded that the X···H(-C) hydrogen bonds are more directional than the X···H(-N) hydrogen bonds. It is generally believed that the more linear (directional) non-covalent interactions are stronger than others. This means that the -NH₃⁺ and -CH₃ groups of the BZA are strongly competitive with each other in forming hydrogen bonded interactions with the X cage in BZA₂SnX₄.

New 1D perovskite

The XRD patterns of the solid solutions of Figure 6.17 showed clear evidence of another phase especially in the $\sim 0.40 < x < \sim 0.55$ compositional range. In particular, this occurred for all the replica of the 50% I/Br samples, while attempts to obtain the new phase pure in Br or I, either via ball milling or by solution, failed. This suggests that the coexistence of mixed halides is crucial for its formations. In order to unveil the nature of the phase formed, we applied solution synthesis to grow single crystals of the



BZA₂Sn(Br_xI_{1-x})₄ solid solution with $x=0.50$. A pool of crystals with different colour shades was obtained, suggesting the presence of crystal with various halide ratios. The structural analysis of several fragments indicated that they possess a monoclinic symmetry with similar lattice parameters. The crystal structure

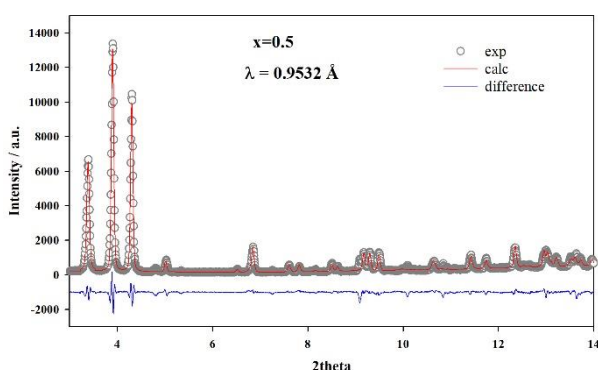


Figure 6.17: a) Sketch of the crystal structure of $BZA_3Sn(Br_{0.5}I_{0.5})_5$ along the b -axis; b) Refinement of powder pattern of $BZA_3Sn(Br_{0.5}I_{0.5})_5$

analysis carried out on a selected fragment led to the discovery of a new 1D tin-based hybrid perovskite, namely $BZA_3Sn(Br_{0.3}I_{0.7})_5$. A sketch of the structure of this novel compound is reported in Figure 6.17a.

The 1D hybrid perovskite belongs to the monoclinic space group $P2_1c$ and has lattice parameters of $a=14.5383(4)$ Å, $b=8.46698(19)$ Å, $c=26.2932(6)$ Å, and $\beta=105.410(3)^\circ$. This new phase is characterized by Sn-

halide corner-sharing octahedra forming 1D nanowires in a zig-zag disposition, surrounded by benzylammonium cations. This arrangement is qualitatively similar to that of IPA_3SnI_5 (where IPA indicate isopropyl ammonium)³⁶, where the smaller organic cation allowed to preserve an orthorhombic unit cell. A similar connectivity was observed in dimethyl ethylenediamine lead bromide³⁷ and foreseen for Cs_3PbI_5 ³⁸, while many other 1D perovskites show unusual hexagonal symmetry for perovskites, with the octahedra sharing faces (e.g. $MAMnBr_3$ ³⁹) or alternating faces and corner connectivity (GA_3SnI_3 ³⁶, GA =guanidinium). The single crystal refinement indicates excess of iodine from nominal $x=0.50$ composition. In order to confirm the formation of 1D perovskite in the samples produced through ball-milling, a sample with nominal composition $x=0.5$ was investigated by synchrotron powder diffraction, using a rotating-capillary-stage which allowed to reduce significantly preferred orientations. The refinement (Figure 6.17b) performed using the structure solved by single crystal confirmed the goodness of the structural solution.

Table 6.2 reports the lattice parameters of the 1D perovskite whenever observed in the solid solution, together with the overall nominal composition x . In general, the lattice parameters of the 1D perovskites were observed to scale monotonically with the nominal Br/I concentration.

Table 6.2: Comparison of lattice parameters of $BZA_3Sn(Br_xI_{1-x})_5$ obtained with different nominal composition

x	X-ray data collection	a	b	c	β
0.30*	Single crystal	14.5383(4)	8.46698(19)	26.2932(6)	105.410(3)
0.30**	Powder - synchrotron	14.490(3)	8.4356(8)	26.295(4)	104.93(2)
0.375	Powder - lab	14.473(8)	8.444(6)	26.23(1)	105.0(1)
0.50	Powder - synchrotron	14.455(2)	8.3984(9)	26.214(3)	104.86(1)
0.625**	Powder - synchrotron	14.418(4)	8.423(6)	26.103(6)	104.54(4)

* value estimated by refinement of I/Br site occupation

** minority phase

Interestingly, the nominal composition $x=0.5$ showed significantly smaller lattice parameters compared to the single-crystal, suggesting Br-enrichment. The lattice contraction occurs nearly isotropically, suggesting it is driven by simple sterical effects related to halide substitution. This result further suggests that $BZA_3Sn(I_xBr_{1-x})_5$ can be potentially formed with different Br/I composition.

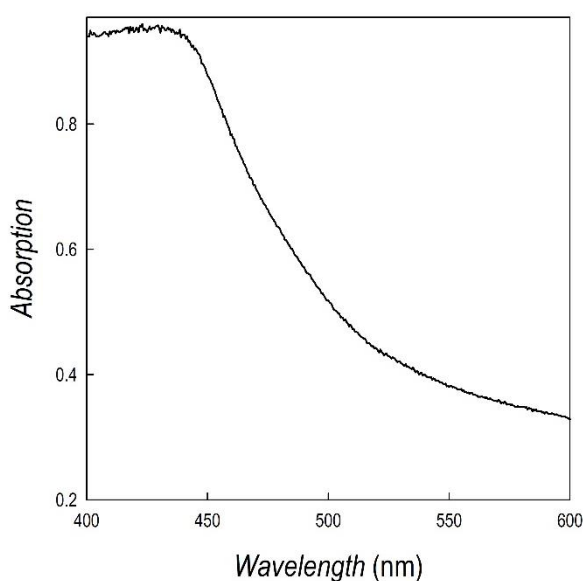


Figure 6.18: Absorption spectra of the $BZA_3Sn(Br_{0.5}I_{0.5})_5$ sample.

As a matter of fact, the tendency in forming 1D perovskites of various I/Br ratios has been observed in the present work when the samples were synthesized by solution chemistry, possibly as a consequence of a reduced reactivity of tin leading to a BZA/Sn stoichiometry more close to 3:1. The use of mechanochemical synthesis allowed a proper control of reagents amount thus providing the set of 2D perovskites presented above. Finally, its absorption spectrum is shown in Figure 6.18, corresponding to a bandgap of 2.05 eV which is intermediate between those of the pure I and Br 2D endmembers.

Experimental section

Materials preparation

Samples of general formula $BZA_2Sn(Br_xI_{1-x})_4$ (1 g) were prepared by a one-step fully dry mechanochemical approach via ball-milling. For the synthesis, a proper stoichiometric amount of the reactants, *e.g.* benzylammonium iodide and bromide (BZAI, BZABr) and tin iodide and bromide (SnI_2 , $SnBr_2$) powders, is transferred to a tungsten carbide (WC) milling bowl with 30.5 mm diameter WC balls. The bowl is tightly

closed and mounted into the planetary ball milling machine (Fritsch, Pulverisette 7, Premium Line), the speed was set to 400 rpm and the reaction time was 6 h. In the planetary ball miller, the jar performs two movements: a rotation around its own axis and a rotation around the centre of the main disk. After the milling, uniformly coloured powders were obtained. For a perfect conservation of the samples, the reaction was set up in a N₂ glove box (to prevent the oxidation of Sn(II) to Sn(IV)), sealed and removed from the glove box, placed in the planetary mill for the reaction and again collected in the glove box, without annealing or other further purifications.

The single crystals of BZASnI₄ and BZASnBr₄ were prepared according to a general and original procedure that our group developed previously¹⁷. In a typical synthesis a proper amount of Sn(II) acetate is dissolved in a large excess of the desired HX acid under continuous stirring and nitrogen atmosphere. Hypophosphoric acid is added to the solution and inert atmosphere is maintained in the reaction environment in order to prevent Sn oxidation. Then, the solution is heated to 100°C and the corresponding BZA solution is added in equimolar amount. The solution is then cooled down to ca. 50°C at 1°C/5 min, until the formation of a needle-shaped precipitate, which is immediately filtered and dried under vacuum overnight. For the synthesis of BZA₂SnCl₄, the procedure was slightly different because the slow cooling of the solution didn't lead to any precipitation. The white product was obtained quenching the 100°C solution in an iced-water bath and then treated as previously reported.

Absorption and photoluminescence

Absorbance was measured with a UV/Vis/NIR spectroscopy (PerkinElmer Lambda 950S) and steady-state PL emission was measured with a Fluorescence spectrometer (PerkinElmer LS 55) and an Edinburgh FLS920 spectrometer equipped with a Peltier-cooled Hamamatsu R928 photomultiplier tube (185-850 nm). An Edinburgh Xe900 450 W Xenon arc lamp was used as exciting light source. Corrected spectra were obtained via a calibration curve supplied with the instrument (lamp power in the steady state PL experiments 0.6 mW cm⁻², spot area 0.5 cm²).

X-ray Diffraction Measurements and refinements

XRD measurements on powdered samples were performed using a Bruker D8 Advance in Bragg–Brentano geometry under Cu K α radiation.

Single crystal data collections for BZA₂SnCl₄ and BZA₃Sn(I_{0.7}Br_{0.3})₅ were performed using a Rigaku Oxford Diffraction SuperNova diffractometer equipped with a Dectris PILATUS3 R 200K-A detector and a micro-focus sealed X-ray tube ($\lambda = 0.71073$ Å). X-ray diffraction intensity data were integrated and corrected for standard Lorentz polarization factors with the CrysAlisPro package, while ABSPACK in CrysAlis RED

was used for the absorption correction.⁴⁰ The structure was solved and refined using the program Shelx-2013.⁴¹

Synchrotron powder diffraction data ($\lambda = 0.9532 \text{ \AA}$) were collected on the high-resolution MCX beamline at the Elettra synchrotron light source (Trieste, Italy).⁴² Standard 0.3 mm diameter borosilicate capillaries were filled with powders under Argon atmosphere ($<0.5 \text{ ppm O}_2$ and H_2O), capped with vacuum grease, and finally sealed using a butane torch. Diffraction patterns were acquired in Debye geometry on the 4-circle Huber goniometer by spinning capillaries at 3000 rpm.

For $\text{BZA}_2\text{SnCl}_4$ isotropic full-matrix least-squares cycles were initially run assuming the atom sites as fully occupied, although unusually high values of the isotropic displacement factor for the Cl1 and Cl2 atoms strongly suggested disorder at those sites. For this reason, the positions of Cl1 and Cl2 was split into two positions (Cl1a/Cl1b and Cl2a/Cl2b) with the site-occupancy left free to be refined. The site scattering at the split positions was identically distributed between the 'a' and 'b' positions and thus fixed in the subsequent cycles of the refinement. The anisotropic model of the structure led to $R1 = 0.0952$. At this stage, considering the similarity in the b and c parameters ($\sim 7.75 \text{ \AA}$), we hypothesized the presence of a twinning simulating a four-fold symmetry axis (four-twinned components) according to the matrix $|-100/001/010|$. Twinning is quite common in perovskite-type materials when the distortion from the cubic aristotype is evident.^{43,44} The introduction of the twin law lowered the R1 index to 0.0638 for 2012 observed reflections [$F_o > 4\sigma(F_o)$] and 107 refined parameters. Further trials using a different refinement program by introducing an additional twin law (merohedral twinning) and higher tensors to describe the displacement parameters for Cl1 and Cl2 did not improve the overall quality of the refinement.⁴⁵

EDX Analysis

Elemental analyses of the powders were performed by Energy Dispersive X-ray Analysis (EDX) by a X-max 50 mm² probe (Oxford Instrument) connected to an EVO MA10 scanning electron microscope (SEM). The powders were dispersed on graphite bi-adhesive supports fixed on Al stubs inside a glove box under Ar atmosphere. The stubs were inserted in a home-made sample holder that was sealed in the glove box and in which the low vacuum was made by a rotary pump. In this way, the samples were transferred in the SEM chamber avoiding the exposition to air. Subsequently, the sample holder was open, and the measurements performed under ultra-high vacuum at a working distance of 8.5 mm and with an electron generation voltage of 20 kV.

Conclusions

We reported a detailed investigation of the lead-free 2D BZA₂SnX₄ (X=I, Br, and Cl) system as a function of the halide nature by preparing, by means of mechanochemistry, two novel compositions, *i.e.* BZA₂SnBr₄ and BZA₂SnCl₄, as well as the BZA₂Sn(Br_xI_{1-x})₄ solid solution. From a structural point of view, the progressive replacement of the halide from iodide to chloride leads to an expansion of the c-axis due to the change in the staggering of the two benzylammonium cations and to a contraction of the in-plane lattice parameters reflecting the different size of the halide. The optical properties show a linear trend in the band gap throughout the I/Br mixed compositions and, together with the BZA₂SnCl₄ sample, the samples cover an optical region extending from about 400 nm to about 700 nm, with PL data showing narrow emission in the whole range. During the study of the 2D BZA₂SnX₄ system we also identified a novel lead-free 1D perovskite showing a possible mixed I/Br composition as well, namely the BZA₂Sn(Br_xI_{1-x})₄ compound. A full computational investigation of the three stoichiometric samples, *i.e.* BZA₂SnX₄ (X=I, Br, and Cl), has been performed by means of DFT calculation providing a complete description of their electronic structure. In conclusion, the data reported extend the actual knowledge on lead-free two-dimensional perovskites, also highlighting the correlation between the staggering of the organic cation as a function of the halide, providing a novel system with emission extending in a wide visible region.

References

1. L. Mao, C. C. Stoumpos, G. Kanatzidis, *J. Am. Chem. Soc.* 2019, 141, 1171-1190.
2. T. D. Gangadhara, T. D. Ma, *Energy Env. Sci.* 2019, 12, 2860-2889.
3. P. Gao, A. R. B. Yusoff, M. K. Nazeeruddin, *Nature Comm.* 2018, 9, 5028.
4. G. Grancini, M. K. Nazeeruddin, *Nature Review Mater.* 2019, 4, 4-22.
5. J. Wang, J. Dong, F. Lu, C. Sun, Q. Zhang, N. Wang, *J. Mater. Chem. A*, 2019, 7, 23563-23576.
6. N. Wang, W. Liu, Q. Zhang, *Small Methods* 2018, 2, 1700380.
7. J. Calabrese, N. L. Jones, R. L. Harlow, N. Herron, D. L. Thorn, Y. Wang, *J. Am. Chem. Soc.* 1991, 113, 2328-2330.
8. C. Smith, E. T. Hoke, D. Solis-Ibarra, M. D. McGehee, H. I. A. Karunadasa, *Angew. Chem., Int. Ed.* 2014, 53, 11232-11235.
9. L. Mao, H. Tsai, W. Nie, L. Ma, J. Im, C. C. Stoumpos, C. D. Malliakas, F. Hao, M. R. Wasielewski, A. D. Mohite, M. G. Kanatzidis, *Chem. Mater.* 2016, 28, 7781-7792.
10. M. E. Kamminga, H.-H. Fang, M. R. Filip, F. Giustino, J. Baas, G. R. Blake, M. A. Loi, T. T. M. Palstra, *Chem. Mater.* 2016, 28, 4554-4562

11. X. N. Li, P. F. Li, W. Q. Liao, J. Z. Ge, D. H. Wu, H. Y. Ye, *Eur. J. Inorg. Chem.* 2017, 938–942.
12. E. R. Dohner, A. Jaffe, L. R. Bradshaw, H. I. Karunadasa, *J. Am. Chem. Soc.* 2014, 136, 13154–13157.
13. S. Yang, Z. Lin, J. Wang, Y. Chen, Z. Liu, E. Yang, J. Zhang, Q. Ling, *ACS Appl. Mater. Interfaces* 2018, 10, 15980–15987.
14. Z. Hong, D. Tan, R. A. John, Y. K. E. Tay, Y. K. T. Ho, X. Zhao, T. C. Sum, N. Mathews, F. Garcia, H. S. Soo, *iScience* 2019, 16, 312–325.
15. A. Karmakar, M. S. Dodd, X. Zhang, M. S. Oakley, M. Klobukowski, V. K. Michaelis, *Chem. Commun.*, 2019, 55, 5079–5082.
16. H. Wang, H. Bian, Z. Jin, H. Zhang, L. Liang, J. Wen, Q. Wang, L. Ding, S. F. Liu, *Chem. Mater.* 2019, 31, 6231–6238.
17. X. Tang, M. van den Berg, E. Gu, A. Horneber, G. J. Matt, A. Osvet, A. J. Meixner, D. Zhang, C. J. Brabec, *Nano Lett.* 2018, 18, 3, 2172–2178.
18. Q. A. Akkerman, S. Park, E. Radicchi, F. Nunzi, E. Mosconi, F. De Angelis, R. Brescia, P. Rastogi, M. Prato, L. Manna, *Nano Lett.* 2017, 17, 3, 1924–1930.
19. Y. Cho, A. M. Soufiani, J. S. Yun, J. Kim, D. S. Lee, J. Seidel, X. Deng, M. A. Green, S. Huang, A. W. Y. Ho-Baillie, *Adv. Energy Mater.* 2018, 8, 1703392.
20. P. Cheng, T. Wu, J. Liu, W.-Q. Deng, K. Han, *J. Phys. Chem. Lett.* 2018, 9, 2518–2522.
21. D. A. Egger, L. Kronik, *J. Phys. Chem. Lett.* 2017, 8, 6154–6159.
22. J. H. Lee, J.-H. Lee, E.-H. Kong, H. M. Jang, *Scientific Reports* 2016, 6, 21687.
23. F. El-Mellouhi, A. Marzouk, E. T. Bentría, S.N. Rashkeev, S. Kais, F. H. Alharbi,
24. K. L. Svane, A. C. Forse, C. P. Grey, G. Kieslich, A. K. Cheetham, A. Walsh, K. T. Butler, *J. Phys. Chem. Lett.* 2017, 8, 6154–6159.
25. L. Z. Tan, F. Zheng, A. M. Rappe, *ACS Energy Lett.* 2017, 2, 937–942.
26. M. W. Lufaso, P. M. Woodward, *Acta Cryst.* 2004, B60, 10–20.
27. K. L. Svane, A. C. Forse, C. P. Grey, G. Kieslich, A. K. Cheetham, A. Walsh, K. T. Butler, *J. Phys. Chem. Lett.* 2017, 8, 6154–6159.
28. M.-H. Jung, *Inorg. Chem.* 2019, 58, 6748–6757.
29. J. M. Frost, K. T. Butler, F. Brivio, C. H. Hendon, M. van Schilfgaarde, A. Walsh, *Nano Lett.* 2014, 14, 2584–2590.
30. A. Mancini, P. Quadrelli, C. Milanese, M. Patrini, G. Guizzetti, L. Malavasi, *Inorg. Chem.* 2015, 54, 8893–8895.
31. M. Patrini, P. Quadrelli, C. Milanese, L. Malavasi, *Inorg. Chem.* 2016, 55, 12752–12757.
32. E. Mosconi, P. Umari, F. De Angelis, *J. Mater. Chem. A* 2015, 3, 9208–9215.
33. G.R. Desiraju, T. Steiner, *The weak hydrogen bond in structural chemistry and biology*, Oxford University Press, Oxford, UK, 1999.
34. G.R. Desiraju, P. Shing Ho, L. Kloo, A.C. Legon, R. Marquardt, P. Metrangolo, P. Politzer, G. Resnati, K. Rissanen, *Pure Appl. Chem.* 2013, 85, 1711–1713.
35. P. Munshi, T.N. Guru Row, *J. Phys. Chem. A* 2005, 109, 659–672.
36. C. C. Stoumpos, L. Mao C. D. Malliakas, M. G. Kanatzidis, *Inorg. Chem.* 2017, 56, 1, 56–73.

37. Z. Yuan, C. Zhou, Y. Tian, Y. Shu, J. Messier, J. C. Wang, L. J. van de Burgt, K. Kountouriotis, Y. Xin, E. Holt, K. Schanze, R. Clark, T. Siegrist, B. Ma, *Nature Communications* 2017, 8, 14051.
38. Z. Xiao, Y. Zhou, H. Hosono, T. Kamiya, N. P. Padture, *Chem. Eur. J.* 2018, 24, 2305–2316.
39. M. Daub, I. Ketterer, H. Hillebrecht, *Z. Anorg. Allg. Chem.* 2018, 644, 280–287.
40. Oxford Diffraction Ltd. CrysAlis RED; Oxford Diffraction Ltd.: Abingdon, UK, 2006.
41. G. M. Sheldrick, *Acta Crystallographica Section C: Structural Chemistry* 2015, 71, 3-8.
42. L. Rebuffi, J. R. Plaisier, M. Abdellatif, A. Lausi, A. P. Scardi, *Zeitschrift fur Anorg. und Allg. Chemie* 2014, 640, 3100–3106.
43. Y. Wang, F. Guyot, A. Yeganeh-Haeri, R. C. Liebermann, *Science* 1990, 248, 468-471.
44. M. U. Rothmann, W. Li, Y. Zhu, U. Bach, L. Spiccia, J. Etheridge, Y. B. Cheng, *Nature Comm.* 2017, 8, 14547.
45. V. Petříček, M. Dušek, L. Palatinus, *Zeitschrift für Kristallographie-Crystalline Materials* 2014, 229, 345-352.

CHAPTER 7.

CONCLUSIONS AND

OUTLOOKS

Today's global population and economic growth is accompanied with a large increase in energy consumption. Satisfying this energy demand by generating energy using traditional sources is inconceivable, so the need of a viable technology to tackle the global energy issue is urgent. Solar photovoltaics represents one of the most efficient response to answer the increasing demand for energy and very recently, metal halide perovskites have emerged as a promising new PV technology, characterized by an incredible increase in efficiency in only a few years after discovery. Besides this high efficiency and the ability to produce thin, lightweight and potentially flexible solar cells, the material's solution processability makes low-cost large-scale production an interesting possibility. The material's tolerance towards compositional changes allows tuning of the material properties towards specific applications.

In this view, the six articles that make up the backbone of this Ph.D. thesis have addressed the modification of the physical-chemical properties through substitution of the main components in some highly interesting hybrid perovskite systems, in order to face the two big problems that still affect these materials: stability and toxicity issues. In the following paragraphs are reported the key points of the entire work.

7.1 Quantitative determination of mixed-ion composition

To have a deep insight into this kind of materials, is fundamental to determine the effective ratio of the mixed-ion composition.

We were the very first group to use the solid state ^1H NMR in order to determine the actual amines ratio. The precise control over the real stoichiometries allowed for the determination of a reliable correlation between the amount of protonated amine and the physiochemical properties.

Regarding the real halide composition, in our last work on the $BZA_2Sn(Br_xI_{1-x})_4$ system (Chapter 6), we estimated the real Br/I and X/Sn ratio of some selected samples of the series using the Energy Dispersive X-Ray Spectroscopy (EDS) finding a very good agreement with the nominal stoichiometric values.

Nominal Value of x	Br/I stoich.	Br/I eff	X/Sn eff
0	-	-	3.85
0.25	3	3.05	4.10
0.625	1.67	1.75	4.24
0.75	0.33	0.38	4.09
1	-	-	3.96

Table 7.1: Br/I and X/Sn ratio of some selected samples calculated using EDS VS the nominal stoichiometric values

7.2 The relevance of electronic dimensionality

In the third chapter we demonstrated that the average cubic structure of $FASnBr_3$ is instantaneously distorted, which means that on the time scale of structural characterizations, the structure is overall cubic, while in the time scale of electronic transitions, the structure is distorted and the average band gap is larger than the band gap of the average structure. That happens because this material is structurally 3D but exhibit quasi-0D electronic structure.

Conventionally, structural dimensionality has been used as the only benchmark to be considered for photovoltaic properties and performances, but this concept fails for some absorber as in the case of $FASnBr_3$. The concept of electronic dimensionality helps to understand why only some 3D halide perovskites do not exhibit the ideal photovoltaic performance as others do. Electronic dimensionality is the connectivity of lower conduction band and upper valence band atomic orbitals. High electronic dimensionality is needed for perovskites to exhibit good photovoltaic performance.

So, $FASnBr_3$ likely represents a limit compound in the compositional space of 3D perovskites, the different electronic structure of $FASnBr_3$ allows the system to “solve” the instability issue related to the large FA cation size but it is a worse absorber. The same happened for $DMASnBr_3$. This sample is very stable against aging, which is an unexpected and exciting result for a Sn-based hybrid perovskite. The improved stability

is very probably related to the lower electronic (and in this case also structural) dimensionality. Other studies are in need to clarify these aspects, but DMASnBr_3 seems to be a quasi-2D material with DMA cations closer to each other promoting the formation of hydrogen bond which stabilize the non-perovskite structure.

7.3 Simpler conditions of reactions: 3D, 2D and NCs perovskites

The synthetic method employed for most of the samples discussed in this thesis differs from the common procedures used in the current literature where hybrid materials are prepared from protonated amine halide and lead halide salts mixed together in an appropriate solvent. Our versatile and optimized approach, starting from the amine solution in water, lead soluble salt and the desired acid, assures a more rigorous control over sample stoichiometries and crystallization path and it can be used for any material for which a protonated amine halide is not available or difficult to synthesize.

It was the same approach used to synthesize the single crystals of the end members of the 2D system analyzed in the sixth chapter leading to the discovery of three new lead-based 2D (and 1D) hybrid perovskites. By slowing the cooling rate, it was possible to obtain needle-shaped single crystals of which we were able to determine the structure. Different was the procedure chosen for the intermediate compositions of the same 2D solid solution, which were mechanochemically synthesized. This kind of approach, besides being green and scalable, allowed us to prevent the Sn-based sample from any contact with air.

The last innovative approach I would like to highlight is the one employed for the anion-exchange reaction in perovskite nanocrystals. This simple and fast approach, in contrast with the most common procedures found in literature, which require difficult to synthesize precursor, hot temperatures and inert atmosphere just employs lead halide precursors at room temperature, without the need for N_2 atmosphere.

7.4 Outlooks

Despite the very fast improvement in power conversion efficiencies, demonstrating the great potential of organolead halide perovskites solar cells, this emerging technology still stands way behind commercialization because of some big challenges: poor stability against moisture and temperature, the development of large-scale manufacturing processes along with the presence of the harmful element lead.

7.4.1 Addressing the stability issue

There are four main factors leading to perovskite instability: environmental factor (moisture and oxygen), hygroscopicity, thermal instability, and ion migration. Moisture and oxygen, as well as the hygroscopicity, can be solved by encapsulation. The thermal instability can be addressed by composition tuning to increase the decomposition energy or barrier, *e.g.*, with FA cations. The issue of ion migration is almost unavoidable. It is currently treated by A-site doping, multiple dimensional perovskites engineering and organic molecular additives, but could be prevented by passivating the grain boundary or increasing the ion migration barrier by engineering the packing density via ion substitution. While the research interest on the stability studies is growing rapidly, the published stability tests have been conducted in a wide range of non-standard conditions, making it impossible to compare the lifetime tests between different laboratories. It is important to point out that the real solar panels are always encapsulated, so the air stability should not be a primary concern. The current goals are firstly to build the relationship between the accelerated aging lifetime and the real lifetime for PSCs and secondly to achieve 1000 h lifetime retaining the 80% of the initial efficiency, under 85 °C and 85% relative humidity. (102)

7.4.2 Reducing the toxicity

The unique electronic configuration of Pb^{2+} provides 3D perovskites with excellent optoelectronic properties. MAPbI_3 , the archetypal hybrid halide perovskite, possesses many ideal properties as a solar absorber: a direct bandgap (E_g) of 1.53 eV, small exciton binding energies (37 or 45 meV), long charge carrier diffusion lengths over 3.5 μm and excellent charge carrier mobilities. These 3D lead halide perovskites possess 25% efficiency record, which make them the fastest growing photovoltaic technology in history, rivalling commercial crystalline silicon solar cells. However, the toxicity issue of the lead urged some researchers to seek alternatives to lead-based perovskites.

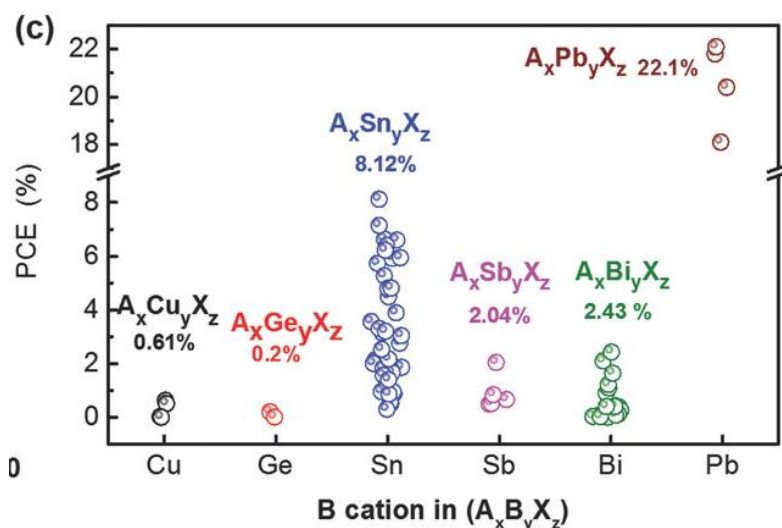


Figure 7.1: Comparison of performance of the device between different lead-free absorbers (103)

Developing nontoxic or low-toxicity and air-stable halide perovskite-based solar cells has attracted extensive attention and has focused on compounds containing Sn^{2+} , Ge^{2+} , Bi^{3+} and Sb^{3+} , which exhibit ns^2 lone pairs as Pb. But the search for alternative materials to replace lead, only leads to stable but very low-performance materials. So, there's come the question: it's possible to have both things at once?

Sn-based absorbers achieved the promising efficiency of $\approx 8\%$, but it is still far from the best Pb-based perovskites. One of the major problems of tin-based PSCs is the well-known self-doping effect. This poor stability, originating from the easy formation of Sn-vacancies associated with oxidation, lead to poor reproducibility and fast deterioration of the device. To suppress this effect, sacrificial additives like Sn(II) halide

salt and some reductive reagents are added. (104) Among the tin-based perovskites, different cations showed different advantages. Sn-based perovskites with FA cation showed higher efficiency and stability than MA counterparts. It has been speculated that FA cation can endow the perovskite with higher formation energies of Sn vacancies (105) and more resistance against oxidation (106) On the other hand, FA-based hybrid perovskites have better solubility than all-inorganic perovskites. As amply demonstrated in this thesis, but also in the current literature, mixing organic cations at A position seems an effective method to improve devices performance. FA–MA mixed tin perovskite showed an impressive band gap tuning, while MA–DMA mixed Sn perovskite yielded a quasi 2D structure with improved air and water stability.

Self-doping effect will still be a challenge to all the researchers working on Sn-based perovskite. A deep insight into the mechanisms of self-doping effect is crucial for achieving efficiency up to 15% or higher, which are theoretical possible. A more suitable procedure only employs “intermediate agent” that could be removed in the final stage or even without using any sacrificial additives. Successful compositional engineering could help to give efficient and stable compounds similar to Pb-based perovskites. Additionally, high-performance and dopant-free HTMs could also assist in achieving more efficient and stable Sn-PSCs. So, the answer to the question above need to be found in the future developments. (103)

It has to be said that there are some studies that swim against the tide about the big topic of lead toxicity: the results reported by Alberola-Borràs et al. (107), Billen et al. (108) and Zhang et al. (109) deserve particular attention. They have demonstrated that the content of Pb in the perovskite contributes to the human toxicity cancer impact category 1-2 orders of magnitude less than the rest of the module components (Glass/ITO (FTO), ETM, HTM and back contact). Substitution of lead with less toxic materials is one of the main challenging purpose for different reasons: (i) the elimination of a cause of concern due to the toxic metal; (ii) the facilitation of the market entry of this new technology also due to the consumer skepticism towards devices containing lead; (iii) the removal of administrative barriers built by the European Union (EU) regarding hazardous materials. In this way, tin has been suggested as a solution. Nevertheless, for the authors, it does not seem to be a promising solution. It exhibits ecotoxicity and global warming potential factors higher than lead and it is a metal with a low substitution potential. Additionally, it has a low distribution in the world (Peru, Indonesia, China), that could lead to supply disruption. Tin is also more expensive than lead, so it could result in a less sustainable PV technology from an economic point of view. (110)

Current literature seems to be very cleaved about this topic and I think that this division does not come from a difference in thoughts and intents, but in the approach to problem solving. What's certain is that the future lies in the hands of the Research. R&D should invest in improve stability, energy efficiency in manufacturing and waste management strategies.

PUBLICATIONS

Reproduced

Reprinted with permission from **A. Pisanu**, C. Ferrara, P. Quadrelli, G. Guizzetti, M. Patrini, C. Milanese, C. Tealdi, L. Malavasi, *The FA_{1-x}MA_xPbI₃ System: Correlation between Stoichiometry Control, Crystal Structure, Optical Properties and Phase Stability*, Journal of Physical Chemistry (2017), 121, 8746. Copyright © 2017 American Chemical Society

C. Ferrara, M. Patrini, C. Tealdi, **A. Pisanu**, C. Milanese, P. Quadrelli e L. Malavasi, *Wide Band-gap Tuning in Sn-based Hybrid Perovskites through Cation Replacement: the FA_{1-x}MA_xSnBr₃ Mixed System*, Journal of Material Chemistry A (2017), 5, 9391 - Reproduced by permission of The Royal Society of Chemistry

Reprinted with permission from **A. Pisanu**, A. Mahata, E. Mosconi, M. Patrini, P. Quadrelli, C. Milanese, F. De Angelis, L. Malavasi, *Exploring the boundary of 3D perovskites domain: The case of FAPb_{1-x}Sn_xBr₃ perovskites*, ACS Energy Letters (2018) 3, 1353. Copyright © 2018 American Chemical Society.

A. Pisanu, P. Quadrelli, L. Malavasi, *Facile Anion-Exchange Reaction in Mixed-Cation Lead Bromide Perovskite Nanocrystals*, RSC Advances (2019) 9, 13263 - Reproduced by permission of The Royal Society of Chemistry

A. Pisanu, P. Quadrelli, G. Drera, L. Sangaletti, A. Speltini, L. Malavasi, *Enhanced Air-Stability of Sn-based Hybrid Perovskites Induced by Dimethylammonium (DMA): Synthesis, Characterization, Aging and Hydrogen Photogeneration of the MA_{1-x}DMA_xSnBr₃ System*, J. Mater. Chem. C (2019), 7, 7020 - Reproduced by permission of The Royal Society of Chemistry

A. Pisanu, M. Coduri, M. Morana, Y. O. Ciftic, A. Rizzo, A. Listorti, M. Gaboardi, L. Bindi, V. I. E. Queloz, C. Milanese, G. Grancini, L. Malavasi, *Exploring the Role of Halide Mixing in Lead-Free BZA₂SnX₄ Two-Dimensional Hybrid Perovskites*, J. Mater. Chem. A (2020), Accepted Manuscript

Other Publications

F. Capitani, C. Marini, S. Caramazza, P. Postorino, G. Garbarino, M. Hanfland, **A. Pisanu**, P. Quadrelli e L. Malavasi, *High-pressure behavior of methylammonium lead iodide (MAPbI₃) hybrid perovskite*, Journal of Applied Physics (2016), 119, 185901

F. Capitani, C. Carlo, S. Caramazza, P. Dore, **A. Pisanu**, L. Malavasi, L. Nataf, F. Baudelet, J.-B. Brubach, P. Roy, P. Postorino, *Locking of Methylammonium by pressure-enhanced H-bonding in MAPbBr₃ hybrid perovskite*, J. Phys. Chem. C (2017), 50, 28125

A. Speltini, A. Scalabrini, F. Maraschi, M. Sturini, **A. Pisanu**, L. Malavasi, A. Profumo, *Improved photocatalytic H₂ production from aqueous glucose biomass by oxidized g-C₃N₄*, Int. J. Hydrogen Energy (2018) 43, 14925

A. Pisanu, A. Speltini, B. Vigani, F. Ferrari, M. Mannini, N. Calisi, B. Cortigiani, A. Caneschi, P. Quadrelli, A. Profumo, L. Malavasi, *Enhanced Hydrogen Photogeneration by Bulk g-C₃N₄ Through a Simple and Efficient Oxidation Route*, Dalton Trans. (2018) 47, 6772-6778

F. Mazzali, M. Orzech, A. Adomkevicius, **A. Pisanu**, L. Malavasi, D. Deganello, and S. Margadonna, *Designing a high-power sodium-ion battery by in situ metal plating*, ACS Appl. Energy Mater. (2019) 2, 344

RINGRAZIAMENTI

Ed ora che sono giunta al termine, mi sento di poter paragonare questi tre anni ad un viaggio: gli esperimenti, i risultati, i lavori conclusi e quelli abbandonati, le buone idee e quelle sbagliate. Tutto questo rappresenta il bagaglio di esperienze che mi caratterizza e che in qualche modo mi ha reso il ricercatore e la persona che sono.

La cosa più importante sono però le persone che mi hanno accompagnata in questo tortuoso viaggio. Perché la ricerca si basa sulle idee, e le idee vengono dalle persone.

Questo lavoro è dedicato alla mia famiglia. Al Babbo, a Mamma, a mia sorella Giada e a quella palla di pelo di Matisse. Vi devo tutto. Senza la necessità di troppe spiegazioni, a voi è dedicato il più grande Grazie: per il supporto, i consigli, la pazienza e l'amore sconfinato che non mi avete mai fatto mancare.

Il tutor è la figura più importante del dottorato e in questo non posso che ritenermi fortunata. Tutto quello che ho imparato in questi anni, che sono molti più dei tre di dottorato, lo devo principalmente a Lorenzo. Grazie per essere stato un punto di riferimento sempre presente e paziente. Il suo entusiasmo per la ricerca e la costante richiesta di qualità mi hanno portato a risultati, scientifici e non, molto più grandi di quanto credessi possibile. Il miglior esempio che potessi chiedere. Il suo supporto costante e l'incoraggiamento sono stati indispensabili per arrivare dove sono ora.

Un Grazie sincero è dedicato al prof. Paolo Quadrelli, per avermi aiutata e sostenuta fin dagli anni della magistrale e per avermi dato la possibilità di lavorare al suo fianco in uno dei migliori laboratori dell'UniPV.

E poi ci sono tutti i ragazzi dell'Auletta. Perché non si vive di sola scienza. Grazie a tutti quelli che mi hanno aiutata, chi con una birra, chi con un esperimento e chi con entrambi. Avete reso questi anni memorabili, pieni di sorrisi, briscole e grafici improbabili. Un grazie particolare va a Sara e Mauro, per tutto il tempo speso assieme, le turbe condivise e la "zampa" data in ogni occasione la richiedesse. Ma soprattutto grazie per la vostra amicizia.

Grazie anche a tutti i membri di ST.E.P., che chi più, chi meno, volenti o nolenti, ormai da 5 anni, rappresentano la mia seconda famiglia. Grazie per essere il mio porto

sicuro. Siete il miglior diversivo ai pensieri molesti e alle numerose giornate monotone che la nostra amata Pavia riesce sempre ad offrirci.

L'ultimo ringraziamento lo voglio dedicare a due amici che mi hanno permesso di mantenere salde le mie prospettive al di fuori della ricerca: Francesca e Primo. Siete state le colonne di questi anni.

Pavia, 5 Ottobre 2019

A handwritten signature in black ink, appearing to read "Roberto Pisu". The signature is written in a cursive, somewhat stylized script.

BIBLIOGRAPHY

1. J. H. Heo, D. H. Sng, B. R. Patil, S. H. Im, Recent progress of innovative perovskite hybrid solar cells, *Israel J. Chem.* 2015, 55, 966.
2. P. R. Ehrlich and A. H. Ehrlich, The Population Explosion, *Prometheus* 1991, 9, 320.
3. F. Karagulian, C. A. Belis, C. G. Dora, A. M. Prüss-Ustün, S. Bonjour, H. Adair-Rohani et al., Contributions to cities' ambient particulate matter (PM): A systematic review of local source contributions at global level, *Atmospheric Environment* 2015, 120, 475-483.
4. <https://www.bp.com/en/global/corporate/energy-economics/statistical-review-of-world-energy/primary-energy.html>.
5. P. Liese, J. Guteland, N. Torvalds, B. Eickhout, L. Boylan, E. Evi, Risoluzione ENVI.
http://www.europarl.europa.eu/meetdocs/2014_2019/plmrep/COMMITTEES/ENVI/RE/2019/02-20/1173148IT.pdf.
6. S. Sgouridis, M. Carbajales-Dale, D. Csala, M. Chiesa, U. Bardi, Comparative net energy analysis of renewable electricity and carbon capture and storage, *Nature Energy* 2019.
7. S. B. Darling, F. You. The case for organic photovoltaics, *RSC Advanced* 2013, 3, 17633-17648.
8. NREL, Transforming Energy. Best Research-Cell Efficiency Chart 2019, <https://www.nrel.gov/pv/cell-efficiency.html>.
9. *Energy efficiency: fundamental physical limits*, J. Nelson, Cambridge : Winton Inaugural Symposium, 2012.
10. Y. Zhao and K. Zhu, Organic-inorganic hybrid lead halide perovskites for optoelectronic and electronic applications, *Chem. Soc. Rev.* 2016, 45, 655-689.
11. C. Becker, T. Sontheimer, S. Steffens, S. Scherf and B. Rech, Polycrystalline silicon thin films by high-rate electronbeam evaporation for photovoltaic applications - influence of substrate texture and temperature, *Energy Procedia* 2011, 10, 61-65.
12. Y. Ichikawa, T. Yoshida, T. Hama, H. Sakai and K. Harashima, Production technology for amorphous silicon-based flexible solar cells, *Solar Energy Materials and Solar Cells* 2001, 66, 107-115.

13. D. L. Wronski, C. R. Staebler, Reversible conductivity changes in discharge produced amorphous Si, *Applied Physics Letters*, 1977, 31, 292-294.
14. V. Plotnikov, X. Liu, N. Paudel, D. Kwon, K.A. Wieland, and A.D. Compaan, Thin-film cdte cells: Reducing the cdte, *Thin Solid Films* 2011, 519, 7134-7137.
15. M. A. Green, K. Emery, Y. Hishikawa, W. Warta and E. D. Dunlop, Solar cell efficiency tables (version 45), *Progress in Photovoltaics: Research and Applications* 2015, 23, 1-9.
16. V. M. Fthenakis, H. Chul Kim and E. Alsema, Emissions from photovoltaic life cycles, *Environmental Science & Technology* 2008, 42, 2168-2174.
17. M. Grätzel, Dye-sensitized Solar Cells, *Journal of Photochemistry and Photobiology C* 2003, 4, 145-153.
18. L. Dou, J. You, Z. Hong, Z. Xu, G. Li, R. A. Street and Y. Yang, 25th anniversary article: a decade of organic/polymeric photovoltaic research, *Adv. Mater.* 2013, 25, 6642-6671.
19. A. Polman, M. Knight, E. C. Garnett, B. Ehrler, W. C. Sinke, Photovoltaic materials: Present efficiencies and future challenges, *Science* 2016, 352, 307.
20. *Geochemische Verterlungsgesetze der Elemente*. M. Goldschmidt, Oslo : Norske Videnskap, 1927.
21. D. B. Mitzi, Synthesis, Crystal Structure and Optical and Thermal Properties of $(C_4H_9NH_3)_2MI_4$ (M=Ge, Sn, Pb), *Chemistry of Material* 1996, 8, 791.
22. Y. Lee, D. Mitzi, P. Barnes and T. Vogt, Pressure-induced phase transitions and templating effect in three-dimensional organic-inorganic hybrid perovskites, *Physical Review B* 2003, 68, 020103.
23. T. Baikie, Y. Fang, J. M. Kadro, M. Schreyer, F. Wei, S. G. Mhaisalkar, M. Graetzel and T. J. White, Synthesis and crystal chemistry of the hybrid perovskite $(CH_3NH_3)PbI_3$ for solid-state sensitised solar cell applications, *Journal of Materials Chemistry A* 2013, 1, 5628.
24. G. Xing, N. Mathews, S. Sun, S. S. Lim, Y. M. Lam, M. Graetzel, S. Mhaisalkar, T. C. Sum and M. Grätzel, Long-range balanced electron- and hole-transport lengths in organic-inorganic $CH_3NH_3PbI_3$, *Science* 2013, 342, 344.
25. S. D. Stranks, G. E. Eperon, G. Grancini, C. Menelaou, M. J. P. Alcocer, T. Leijtens, L. M. Herz, A. Petrozza and H. J. Snaith, Electron-hole diffusion lengths exceeding 1 micrometer in an organometal trihalide perovskite absorber, *Science* 2013, 342, 341.
26. C. S. Ponseca, T. J. Savenije, M. Abdellah, K. Zheng, A. Yartsev, T. Pascher, T. Harlang, P. Chabera, T. Pullerits, A. Stepanov, J.-P. Wolf and V. Sundström. Organometal Halide Perovskite Solar Cell Materials Rationalized: Ultrafast Charge

Generation, High and Microsecond-Long Balanced Mobilities, and Slow Recombination, *Journal of the American Chemical Society* 2014, 136, 5189.

27. C. C. Stoumpos, C. D. Malliakas and M. G. Kanatzidis, Semiconducting tin and lead iodide perovskites with organic cations: phase transitions, high mobilities, and nearinfrared photoluminescent properties, *Inorganic chemistry* 2013, 52, 9019.

28. A. Kojima et. al., Organometal Halide Perovskites as Visible-Light Sensitizers for Photovoltaic Cells, *J. Am. Chem. Soc.* 2009, 131, 6050-6051.

29. I. Chung, B. Lee, J. He, R. P. H. Chang and M. G. Kanatzidis, All-solid-state dye-sensitized solar cells with high efficiency, *Nature*. 2012, 485.

30. H. S. Kim, C. R. Lee, J. H. Im, K. B. Lee, T. Moehl, A. Marchioro, S. J. Moon, R. Humphry-Baker, J. H. Yum, J. E. Moser, M. Grätzel and N. G. Park, Lead iodide perovskite sensitized all-solid-state submicron thin film mesoscopic solar cell with efficiency exceeding 9%, *Scientific Reports* 2012, 2, 591.

31. M. M. Lee, J. Teuscher, T. Miyasaka, T. N. Murakami and H. J. Snaith, Efficient hybrid solar cells based on meso-superstructured organometal halide perovskites, *Science* 2012, 338, 643-647.

32. J. Burschka, N. Pellet, S. J. Moon, R. Humphry-Baker, P. Gao, M. K. Nazeeruddin and M. Grätzel, Sequential deposition as a route to high-performance perovskite-sensitized solar cells, *Nature* 2013, 499, 316.

33. S. Chavhan, O. Miguel, H. J. Grande, V. Gonzalez-Pedro, R. S. Sánchez, E. M. Barea, I. Mora-Seró and R. Tena-Zaera, Organo-metal halide perovskite-based solar cells with CuSCN as the inorganic hole selective contact, *Journal of Materials Chemistry A* 2014, 2, 12754.

34. S. Ye, W. Sun, Y. Li, W. Yan, H. Peng, Z. Bian, Z. Liu and C. Huang, CuSCN-Based Inverted Planar Perovskite Solar Cell with an Average PCE of 15.6%, *Nano Letters* 2015, 15, 3723.

35. J. H. Heo, S. H. Im, J. H. Noh, T. N. Mandal, C. S. Lim, J. A. Chang, Y. H. Lee, H. J. Kim, A. Sarkar, M. K. Nazeeruddin, M. Grätzel and S. I. Seok, Efficient inorganic-organic hybrid heterojunction solar cells containing perovskite compound and polymeric hole conductors, *Nature Photonics* 2014, 7, 2614.

36. N. J. Jeon, J. H. Noh, Y. C. Kim, W. S. Yang, S. Ryu and S. I. Seok, Solvent engineering for high-performance inorganic-organic hybrid perovskite solar cells, *Nature materials* 2014.

37. A. Yella, L. P. Heiniger, P. Gao, M. K. Nazeeruddin and M. Grätzel, Nanocrystalline rutile electron extraction layer enables low-temperature solution

processed perovskite photovoltaics with 13.7% efficiency, *Nano Letters* 2014, 14, 2591-2596.

38. M. Liu, M. B. Johnston and H. J. Snaith, Efficient planar heterojunction perovskite solar cells by vapour deposition, *Nature* 2013, 501, 395-398.

39. Q. Chen, H. Zhou, Z. Hong, S. Luo, H. S. Duan, H. H. Wang, Y. Liu, G. Li, and Y. Yang, Planar Heterojunction Perovskite Solar Cells via Vapor-Assisted Solution Process, *Journal of the American Chemical Society* 2014, 136, 622-625.

40. E. H. Anaraki, A. Kermanpur, L. Steier, K. Domanski, T. Matsui, W. Tress, M. Saliba, A. Abate, M. Grätzel, A. Hagfeldt and J. P. Correa-Baena, Highly efficient and stable planar perovskite solar cells by solution-processed tin oxide, *Energy Environ. Sci.* 2016, 10, 3128-3134.

41. Z. Xiao, et al., Solvent annealing of perovskite-induced crystal growth for photovoltaic-device efficiency enhancement, *Adv. Mater.* 2014, 26, 6503-6509.

42. M. A. Green, A. Ho-Baillie and H. J. Snaith, The emergence of perovskite solar cells, *Nat. Photonics.* 2014, 8, 506-514.

43. G. Grancini et al., Role of microstructure in the electron-hole interaction of hybrid lead halide perovskites, *Nat. Photonics* 2015, 9, 695-701.

44. L. Dou et al., Atomically thin two-dimensional organic-inorganic hybrid perovskites, *Science* 2015, 349, 1518-1521.

45. C. C. Stoumpos et al., Ruddlesden-Popper hybrid lead iodide perovskite 2D homologous semiconductors, *Chem. Mater.* 2016, 28, 2852-2867.

46. X. Wu, M. T. Trinh and X. Y. Zhu, Excitonic many-body interactions in two-dimensional lead iodide perovskite quantum wells, *J. Phys. Chem. C* 2015, 119, 14714-14721.

47. J. Huang, Y. Yuan, Y. Shao and Y. Yan, Understanding the physical properties of hybrid perovskites for photovoltaic applications, *Nature reviews* 2017, 2, 1-19.

48. A. Zunger, A. Walsh, Instilling defect tolerance in new compounds, *Nature Materials* 2017, 16, 964-967.

49. W. J. Yin, T. Shi and Y. Yan, Unique properties of halide perovskites as possible origins of the superior solar cell performance, *Adv. Mater* 2014, 26, 4653-4658.

50. L. M. Pazos-Outón et al., Photon recycling in lead iodide perovskite solar cells, *Science* 2016, 351, 1430-1433.

51. Z. Xiao, W. Meng, J. Wang, D. B. Mitzi and Y. Yan, Searching for promising new perovskite-based photovoltaic absorbers: the importance of electronic dimensionality, *Mater. Horiz.* 2017, 4, 206-216.

52. Y. Deng, Z. Xiao and J. Huang, Light induced self-poling effect in organometal trihalide perovskite solar cells for increased device efficiency and stability, *Adv- Energy Mater.* 2015, 5, 1500721.
53. J. M. Frost, K. T. Butler, F. Brivio, C. H. Hendon, M. van Schilfgarde and A. Walsh, Atomistic Origins of High-Performance in Hybrid Halide Perovskite Solar Cells, *Nano Letters* 2014, 14, 2584.
54. J. Xu, A. Buin, A. H. Ip, W. Li, O. Voznyy, R. Comin, M. Yuan, S. Jeon, Z. Ning, J. J. McDowell, P. Kanjanaboos, J. P. Sun, X. Lan, L. N. Quan, D. H. Kim, I. G. Hill, P. Maksymovych and E. H. Sargent, Perovskite–fullerene hybrid materials suppress hysteresis in planar diodes, *Nature Communications* 2015, 6, 7081.
55. D. Wei, F. Ma, R. Wang, S. Dou, P. Cui, H. Huang, J. Ji, E. Jia, X. Jia, S. Sajid, A. M. Elseman, L. Chu, Y. Li, B. Jiang, J. Qiao, Y. Yuan and M. Li, Ion-Migration Inhibition by the Cation– π Interaction in Perovskite Materials for Efficient and Stable Perovskite Solar Cells, *Advanced Materials* 2018, 30, 1701583.
56. M. Bag, L. A. Renna, R. Y. Adhikari, S. Karak, F. Liu, P. M. Lahti, T. P. Russell, M. T. Tuominen, D. Venkataraman, Kinetics of Ion Transport in Perovskite Active Layers and Its Implications for Active Layer Stability, *J. Am. Chem. Soc.* 2015, 40, 13130.
57. J. Xing, Q. Wang, Q. Dong, Y. Yuan, Y. Fanga and J. Huang, Ultrafast ion migration in hybrid perovskite polycrystalline thin films under light and suppression in single crystals, *Physical Chemistry Chemical Physics* 2016, 18, 30484.
58. Y. C. Zhao, W. K. Zhou, X. Zhou, K. H. Liu, D. P. Yu and Q. Zhao, Quantification of light-enhanced ionic transport in lead iodide perovskite thin films and its solar cell applications, *Light: Science & Applications* volume 2017, 6, e16243.
59. Q. Chen, N. De Marco, Y. Yang, T. Song, C. Chen, H. Zhao, Z. Hong, H. Zhou, Y. Yang, Under the spotlight: The organic–inorganic hybrid halide perovskite for optoelectronic applications, *Nano Today* 2015, 10, 355.
60. C. C. Stoumpos, C. D. Malliakas, M. G. Kanatzidis, Semiconducting tin and lead iodide perovskites with organic cations: phase transitions, high mobilities, and near-infrared photoluminescent properties, *Inorg. Chem* 2013, 52, 9019.
61. J. M. Kadro et al., The End-of-Life of Perovskite PV, *Joule* 2017, 1, 29.
62. Q. Zhang, F. Hao, J. Li, Y. Zhou, Y. Wei and H. Lin, Perovskite solar cells: must lead be replaced – and can it be done?, *Science and Technology of Advanced Materials* 2018, 19, 425.
63. O. Stroyuk, Lead-free hybrid perovskites for photovoltaics, *Beilstein J. Nanotechnol.* 2018, 9, 2209.

64. A. Mancini, P. Quadrelli, C. Milanese, M. Patrini, G. Guizzetti, L. Malavasi, CH₃NH₃Sn_xPb_{1-x}Br₃ Hybrid Perovskite Solid Solution: Synthesis, Structure, and Optical Properties, *Inorg. Chem.* 2015, 54, 8893.
65. M. Patrini, P. Quadrelli, C. Milanese and L. Malavasi, FA_{0.8}MA_{0.2}Sn_xPb_{1-x}I₃ Hybrid Perovskite Solid Solution: Toward Environmentally Friendly, Stable, and Near-IR Absorbing Materials, *Inorg. Chem.* 2016, 55, 12752.
66. F. Wang, J. Ma, F. Xie, L. Li, J. Chen, J. Fan, N. Zhao, Organic Cation-Dependent Degradation Mechanism of Organotin Halide Perovskites. *Advanced Functional Materials* 2016, 26, 20.
67. A. Bernasconi, A. Rizzo, A. Listorti, A. Mahata, E. Mosconi, F. De Angelis, L. Malavasi, Synthesis, Properties, and Modeling of Cs_{1-x}Rb_xSnBr₃ Solid Solution: A New Mixed-Cation Lead-Free All-Inorganic Perovskite System, *Chem. Mater.* 2019, 31, 3527.
68. C. Anelli, M. R. Chierotti, S. Bordignon, P. Quadrelli, D. Marongiu, G. Bongiovanni, L. Malavasi, Investigation of Dimethylammonium (DMA) Solubility in MAPbBr₃ Hybrid Perovskite: Synthesis, Crystal Structure and Optical Properties, *Inorg. Chem.* 2019, 59, 944.
69. Q.A. Akkerman, G. Rainò, M. V. Kovalenko, L. Manna, Genesis, Challenges and Opportunities for Colloidal Lead Halide Perovskite Nanocrystals, *Nat. Mater.* 2018, 17, 394.
70. L. Protesescu, S. Yakunin, M. I. Bodnarchuk, F. Krieg, R. Caputo, C. H. Hendon, R. X. Yang, A. Walsh, M. V. Kovalenko, Nanocrystals of Cesium Lead Halide Perovskites (CsPbX₃, X = Cl, Br, and I): Novel Optoelectronic Materials Showing Bright Emission with Wide Color Gamut, *Nano Lett.* 2015, 15, 3692.
71. L. C. Schmidt, A. Pertegas, S. Gonzalez-Carrero, O. Malinkiewicz, S. Agouram, G. Minguez Espallargas, H. J. Bolink, R. E. Galian and J. Perez-Prieto, Nontemplate Synthesis of CH₃NH₃PbBr₃ Perovskite Nanoparticles, *J. Am. Chem. Soc.* 2014, 136, 850.
72. J. A. Sichert, Y. Tong, N. Mutz, M. Vollmer, S. Fischer, K. Z. Milowska, R. García Cortadella, B. Nickel, C. Cardenas-Daw, J. K. Stolarczyk, A. S. Urban, J. Feldmann, Quantum Size Effect in Organometal Halide Perovskite Nanoplatelets, *Nano Lett.* 2015, 15, 6521.
73. Y. Bekenstein, B. A. Koscher, S. W. Eaton, P. Yang, A. P. Alivisatos, Highly Luminescent Colloidal Nanoplates of Perovskite Cesium Lead Halide and Their Oriented Assemblies, *J. Am. Chem. Soc.* 2015, 137, 16008.
74. Q. A. Akkerman, S. Genaro Motti, A. R. S. Kandada, E. Mosconi, V. D'Innocenzo, G. Bertoni, S. Marras, B. A. Kamino, L. Miranda, F. De Angelis, A. Petrozza, M. Prato, L. Manna, Solution Synthesis Approach to Colloidal Cesium Lead Halide Perovskite

- Nanoplatelets with Monolayer-Level Thickness Control, *J. Am. Chem. Soc.* 2016, 138, 1010.
75. M. C. Weidman, A. J. Goodman, W. A. Tisdale, Colloidal Halide Perovskite Nanoplatelets: An Exciting New Class of Semiconductor Nanomaterials. *Chem. Mater.* 2017, Vol. 29, 5019.
76. Y. Tong, E. Bladt, M. F. Aygüler, A. Manzi, K. Z. Milowska, V. A. Hintermayr, P. Docampo, S. Bals, A. S. Urban, L. Polavarapu, J. Feldmann, Highly Luminescent Cesium Lead Halide Perovskite Nanocrystals with Tunable Composition and Thickness by Ultrasonication, *Angew. Chem. Int. Edit.* 2016, 55, 13887.
77. Z. Y. Zhu, Q. Q. Yang, L. F. Gao, L. Zhang, A. Y. Shi, C. L. Sun, Q. Wang, H. L. Zhang, Solvent-Free Mechanochemical Synthesis of Composition-Tunable Cesium Lead Halide Perovskite Quantum Dots, *J. Phys. Chem. Lett.* 2017, 8, 1610.
78. Q. Pan, H. Hu, Y. Zou, M. Chen, L. Wu, D. Yang, X. Yuan, J. Fan, B. Sun and Q. Zhang, Microwave-Assisted Synthesis of High-Quality All-Inorganic CsPbX₃ (X = Cl, Br, I) Perovskite Nanocrystals and the Application in Light Emitting Diode. *J. Mater. Chem. C.* 2017, 5, 10947.
79. J. De Roo, M. Ibáñez, P. Geiregat, G. Nedelcu, W. Walravens, J. Maes, J. C. Martins, I. Van Driessche, M. V. Kovalenko, Z. Hens, Highly Dynamic Ligand Binding and Light Absorption Coefficient of Cesium Lead Bromide Perovskite Nanocrystals, *ACS Nano.* 2016, 10, 2071.
80. B. Ai, C. Liu, J. Wang, J. Xie, J. Han, X. Zhao, Precipitation and Optical Properties of CsPbBr₃ Quantum Dots in Phosphate Glasses, *J. Am. Ceram. Soc.* 2016, 99, 2875.
81. S. Liu et al., Novel CsPbI₃ QDs Glass with Chemical Stability and Optical Properties, *J. Eur. Ceram. Soc.* 2018, 38, 1998.
82. X. Di, Z. Hu, J. Jiang, M. He, L. Zhou, W. Xiang and X. Liang, Use of Long-Term Stable CsPbBr₃ Perovskite Quantum Dots in Phospho-Silicate Glass for Highly Efficient White Leds, *Chem. Commun.* 2017, 53, 11068.
83. C. C. Stoumpos, C. D. Malliakas, M. G. Kanatzidis, Semiconducting Tin and Lead Iodide Perovskites with Organic Cations: Phase Transitions, High Mobilities, and near-Infrared Photoluminescent Properties, *Inorg. Chem.* 2013, 52, 9019.
84. L. Protesescu, S. Yakunin, S. Kumar, J. Bär, F. Bertolotti, N. Masciocchi, A. Guagliardi, M. Grotevent, I. Shorubalko, M. I. Bodnarchuk, C.-J. Shih, M. V. Kovalenko, Dismantling the “Red Wall” of Colloidal Perovskites: Highly Luminescent Formamidinium and Formamidinium–Cesium Lead Iodide Nanocrystals, *ACS Nano.* 2017, 11, 3119.

85. R. E. Beal, D. J. Slotcavage, T. Leijtens, A. R. Bowring, R. A. Belisle, W. H. Nguyen, G. F. Burkhard, E. T. Hoke, M. D. McGehee, Cesium Lead Halide Perovskites with Improved Stability for Tandem Solar Cells, *J. Phys. Chem. Lett.* 2016, 7, 746.
86. G. Nedelcu, L. Protesescu, S. Yakunin, M. I. Bodnarchuk, M. J. Grotevent, M. V. Kovalenko, Fast Anion-Exchange in Highly Luminescent Nanocrystals of Cesium Lead Halide Perovskites (CsPbX_3 , $X = \text{Cl, Br, I}$), *Nano Lett.* 2015, 15, 5635.
87. Q. A. Akkerman, V. D'Innocenzo, S. Accornero, A. Scarpellini, A. Petrozza, M. Prato, L. Manna, Tuning the Optical Properties of Cesium Lead Halide Perovskite Nanocrystals by Anion Exchange Reactions, *J. Am. Chem. Soc.* 2015, 137, 10276.
88. L. Protesescu, S. Yakunin, M. I. Bodnarchuk, F. Bertolotti, N. Masciocchi, A. Guagliardi and M. V. Kovalenko, Monodisperse Formamidinium Lead Bromide Nanocrystals with Bright and Stable Green Photoluminescence, *J. Am. Chem. Soc.* 2016, 138, 14202.
89. G. Grancini, C. Roldán-Carmona, I. Zimmermann, E. Mosconi, X. Lee, D. Martineau, S. Narbey, F. Oswald, F. De Angelis, M. Graetzel and M. Khaja Nazeeruddin, One-year stable perovskite solar cells by 2D/3D interface engineering, *Nat. Commun.* 2017, 8, 15684.
90. A. H. Slavney, R. W. Smaha, I. C. Smith, A. Jaffe, D. Umeyama and H. I. Karunadasa, Chemical approaches to addressing the instability and toxicity of lead-halide perovskite absorbers, *Inorg. Chem.* 2017, 56, 46.
91. T. A. Berhe, W.-N. Su, C.-H. Chen, C.-J. Pan, J.-H. Cheng, H.-M. Chen, M.-C. Tsai, L.-Y. Chen, A. A. Dubaleb and B.-J. Hwang, Organometal halide perovskite solar cells: degradation and stability, *Energy Environ. Sci.* 2016, 9, 323.
92. E. Bi, H. Chen, F. Xie, Y. Wu, W. Chen, Y. Su, A. Islam, M. Gratzel, X. Yang and L. Han, Diffusion engineering of ions and charge carriers for stable efficient perovskite solar cells, *Nat. Commun.* 2017, 8, 15330.
93. M. Grätzel, The rise of highly efficient and stable perovskite solar cells, *Acc. Chem. Res.* 2017, 50, 487.
94. J. You et al., Improved air stability of perovskite solar cells via solution-processed metal oxide transport layers, *Nat. Nanotechnol.* 2016, 11, 75.
95. F. Bella, G. Griffini, J.-P. Correa-Baena, G. Saracco, M. Grätzel, A. Hagfeldt, S. Turri, C. Gerbaldi, Improving efficiency and stability of perovskite solar cells with photocurable fluoropolymers, *Science* 2016, 354, 203.
96. X. Li, M. I. Dar, C. Yi, J. Luo, M. Tschumi, S. M. Zakeeruddin, M. Khaja Nazeeruddin, H. Han and M. Grätzel, Improved performance and stability of perovskite solar cells by

crystal crosslinking with alkylphosphonic acid ω -ammonium chlorides, *Nat. Chem.* 2015, 7, 703.

97. D. H. Cao, C. C. Stoumpos, O. K. Farha, J. T. Hupp, M. G. Kanatzidis, 2D homologous perovskites as light-absorbing materials for solar cell applications, *J. Am. Chem. Soc.* 2015, 137, 7843.

98. D. B. Mitzi, Templating and structural engineering in organic-inorganic perovskites, *J. Chem. Soc., Dalton Trans.* 2001, 1.

99. Y. Lekina, Z. X. Shen, Excitonic states and structural stability in two-dimensional hybrid organic-inorganic perovskites, *Journal of Science: Advanced Materials and Devices* 2019, 4, 189.

100. K. Matsuishi, T. Suzuki, S. Onari, E. Gregoryanz, R. J. Hemley, Excitonic states of alkylammonium lead-iodide layered perovskite semiconductors under hydrostatic pressure to 25 gpa, *Phys. Status Solidi Basic Res.* 2001, 223, 177.

101. G. Grancini, C. Roldán-Carmona, I. Zimmermann, E. Mosconi, X. Lee, D. Martineau, S. Narbey, F. Oswald, F. De Angelis, M. Graetzel & Mohammad Khaja Nazeeruddin, One-Year stable perovskite solar cells by 2D/3D interface engineering, *Nature Communications* 2017, 8, 15684.

102. L. Meng, J. You and Y. Yang, Addressing the stability issue of perovskite solar cells for commercial applications, *Nature Communications* 2018, 9, 5265.

103. L. Liang, P. Gao, Lead-Free Hybrid Perovskite Absorbers for Viable Application: Can We Eat the Cake and Have It too?, *Advanced Science* 2017, 5, 1700331.

104. I. Chung, B. Lee, J. He, R. P. H. Chang, M. G. Kanatzidis, All-solid-state dye-sensitized solar cells with high efficiency, *Nature* 2012, 485, 486.

105. T. Shi, H. Zhang, W. Meng, Q. Teng, M. Liu, X. Yang, Y. Yan, H.-L. Yip, Y. Zhao, Effects of organic cations on the defect physics of tin halide perovskites, *J. Mater. Chem. A* 2017, 5, 15124.

106. F. Wang, J. Ma, F. Xie, L. Li, J. Chen, J. Fan, N. Zhao, Organic Cation-Dependent Degradation Mechanism of Organotin Halide Perovskites, *Adv. Funct. Mater.* 2016, 26, 3417.

107. J. A. Alberola-Borràs, R. Vidal, E. J. Juárez-Pérez, Relative impacts of methylammonium lead triiodide perovskite solar cells based on life cycle assesment, *Sol Energy Mater Sol Cells* 2018, 179, 169.

108. P. Billen, E. Leccisi, S. Dastidar, Comparative evaluation of lead emissions and toxicity potential in the life cycle of lead halide perovskite photovoltaics, *Energy* 2019, 166, 1089.

109. J. Zhang, X. Gao, Y. Deng, B. Li, C. Yuan, Life Cycle Assessment of Titania Perovskite Solar Cell Technology for Sustainable Design and Manufacturing, *ChemSusChem* 2015, 8, 3882.
110. N. Mariotti, M. Bonomo, C. Barolo, Emerging photovoltaic technologies and eco-design - Criticisms and potential improvements, *Environmental Impacts of Solar Panels*, Dr. Abdülkerim Gok (Ed.), 2019.
111. G. Grancini and M. K. Nazeeruddin, Dimensional tailoring of hybrid perovskites for photovoltaics, *Nature Reviews Materials* 2019, 4, 4.